

Search for GUT Magnetic Monopoles
and Other Supermassive Particles
with the MACRO Detector

Thesis by
Jiangtao Hong

In Partial Fulfillment of the Requirements
for the Degree of
Doctor of Philosophy

California Institute of Technology
Pasadena, California

1993

(Submitted on February 22, 1993)

-ii-

To my parents.



Monopole , **A**strophysics , and **C**osmic **R**ay **O**bservatory

*We must pity the student in his deep dark hole
Whose thesis depends on that one monopole.
— Sheldon L. Glashow (1986)*

Acknowledgements

I wish to express my deepest gratitude to my thesis adviser Professor Barry C. Barish and to my *de facto* co-adviser Professor Charles W. Peck for their excellent guidance and generous support. Both of them are first class scientists, yet they have very different styles; I am glad to have learned many different things from their combined guidance.

I thank Dr. Gang Liu for many stimulating discussions and hands-on help. His effort in developing the slow monopole trigger circuits is greatly appreciated. I thank Dr. Douglas Michael for many useful discussions and constructive advice on various subjects.

I want to take this opportunity to thank all my fellow graduate students in the Caltech MACRO group: S. Coutu, E. Katsavounidis, S. Kyriazopoulou, R. Liu, B. Nolty, N. Pignatano, K. Scholberg, J. Steele, and C. Walter. It has been a great pleasure to work with them. In particular, I thank KS for reading through this manuscript and providing data for Fig. 2.11, and RL for Fig. 3.17.

I wish to thank all members of the MACRO collaboration, whose names are gratefully acknowledged in Appendix A. Their collective effort makes the MACRO experiment and this thesis work possible. In particular, I thank Professor Adalberto Sciubba for a critical reading of this work and Dr. Ed Kearns for useful discussions regarding this data analysis.

I thank the technical support staff in the Caltech high energy physics group for their productive work in manufacturing the slow monopole trigger circuits.

Abstract

Magnetic monopoles naturally arise in grand unified gauge theories and are believed to carry a mass of $\sim 10^{17} \text{ GeV}/c^2$. Strange quark matter (nuclearites) may be the true QCD ground state and its mass could vary from $\sim 100 \text{ GeV}/c^2$ to the neutron star mass. Both of them could travel at any velocities from $3.7 \times 10^{-5}c$ to $\sim 10^{-2}c$. Experimental discovery of either one would have profound implications. This thesis presents a search with the MACRO detector for both of them and any other supermassive particles that are scintillating, slow-moving and highly-penetrating.

The MACRO detector is a large underground detector located at Gran Sasso, Italy, with the primary goal of searching for magnetic monopoles at a flux level beyond the astrophysical Parker bound. It employs liquid scintillator counters, streamer tubes and track-etch detectors. When completed, it will have an acceptance of $10,000 \text{ m}^2\text{sr}$.

This search is conducted with the large liquid scintillator detector in the first supermodule of the MACRO detector, which has an acceptance of $870 \text{ m}^2\text{sr}$. A specialized slow monopole trigger is based on the time of passage of slow particles through each scintillator counter and enables the detection of supermassive particles with velocities as low as $\sim 10^{-4}c$. A second trigger is based on the time of flight between different scintillator layers and covers relatively fast velocity range up to $2 \times 10^{-2}c$. The scintillator waveforms are recorded for both triggers. Both triggers collected data over a period of two years from October 1989 to November 1991. The data were analyzed to search for slow particles. The absence of candidates establishes an upper limit on the flux of supermassive particles at

$8.7 \times 10^{-15} \text{cm}^{-2} \text{sr}^{-1} \text{sec}^{-1}$ for $3 \times 10^{-3} < \beta < 2 \times 10^{-2}$ and at $5.6 \times 10^{-15} \text{cm}^{-2} \text{sr}^{-1} \text{sec}^{-1}$ for $\beta_0 < \beta < 3 \times 10^{-3}$. The low velocity cutoff β_0 depends on the type of supermassive particles. For magnetic monopoles, the cutoff based on the Ficenech *et al.* slow proton scintillation measurement is $\beta_0 = 1.8 \times 10^{-4}$, and the pessimistic cutoff based on the most conservative Ahlen-Tarlé light yield model is $\beta_0 = 7 \times 10^{-4}$. For dyons or monopole-proton composites, the model independent cutoff is $\beta_0 = 9 \times 10^{-5}$. Bracci *et al.* have argued that most likely bare monopoles have bound protons in the early universe, making this dyon search more significant. The application of this flux limit to other supermassive particles including nuclearites is described in Chapter 5.

Table of Contents

1	Introduction	1
1.1	Magnetic Monopoles	2
1.1.1	Monopoles before GUTs	2
1.1.2	Monopoles and GUTs	3
1.1.3	Monopoles and Cosmology	5
1.1.4	Monopole and Astrophysics	8
	Monopole Velocities	8
	Parker Bound	9
1.1.5	Previous Monopole Searches	10
	Induction Technique	11
	Scintillation Counters	12
	Gaseous Detectors	13
	Track-etch Detectors	14
	Catalysis of Nucleon Decay	15
1.1.6	Summary	15
1.2	Other Supermassive Particles	16
1.2.1	Nuclearites	16
1.2.2	Fractionally Charged Superstring Particles	18
2	The MACRO Detector	19
2.1	The Gran Sasso Laboratory	19
2.2	General Description of the MACRO Detector	20
2.2.1	Mechanical Structure	21
2.2.2	Streamer Tubes	23

2.2.3	Track-etch Detectors	26
2.2.4	Online Data Acquisition System	26
2.3	Liquid Scintillator Counters	27
2.3.1	Counter Geometries and Optics	28
	Horizontal Counters	31
	Vertical Counters	35
2.3.2	Liquid Scintillator	35
2.3.3	Photomultiplier Tubes	37
2.4	Conclusions	40
3	Monopole Trigger Schemes and Their Sensitivities	41
3.1	Light Yield of Slow-moving Particles	43
3.1.1	Scintillation of Slow-moving Charged Particles	43
3.1.2	Black Body Radiation of Nuclearites	46
3.2	Slow Monopole Trigger	49
3.2.1	Motivations	49
3.2.2	Circuits	52
3.2.3	Trigger Efficiency Studies	58
3.2.4	Implementation in the First Supermodule	62
3.3	Fast Monopole Trigger	64
3.4	Configurations in the First Supermodule	67
3.5	Measurement of Slow Monopole Trigger Sensitivity	76
3.6	Conclusions	87
4	Data Analysis	88
4.1	Run Selections	88
4.2	Slow Monopole Analysis	95
4.2.1	Selection of Candidates	96
4.2.2	Visual Scanning of Candidates	105
4.3	Fast Monopole Analysis	119
4.3.1	Waveform Baseline Fitting	119
4.3.2	Fast Monopole Analysis	121
4.4	Acceptance and Flux Limits	137

5	Conclusions	144
A	Members of the MACRO Collaboration	147
B	Photoelectron Statistics	149
C	Simulations of Pulse Trains	152
D	Numbers of Stopping Muons in FMT Candidates	159
	Bibliography	162

List of Figures

1.1	Evolution of the inverse of the three coupling constants	6
2.1	Geographical Map of Central Italy	20
2.2	Structure of the full MACRO detector	22
2.3	Cross-sectional end view of the first supermodule	24
2.4	Geometry of the horizontal counter	30
2.5	Geometry of the vertical counter	30
2.6	Design of the light collection mirror for the horizontal counter	32
2.7	Photocathode response as a function of the incident angle	32
2.8	Response function of the scintillator counter	34
2.9	Counter response as a function of scintillant concentration	36
2.10	Geometry and base of the Hamamatsu R1408 phototube	38
2.11	Single photoelectron charge spectrum	39
2.12	Phototube saturations	40
3.1	Sensitive β ranges of monopole triggers	42
3.2	Predicted light yield for supermassive charged particles	47
3.3	Passage of a $\beta = 10^{-3}$ particle through the MACRO detector	51
3.4	Monte Carlo simulated pulse trains	53
3.5	TOHM circuits	54
3.6	Leaky Integrator	55
3.7	LED simulation of the slow monopole trigger efficiency	60
3.8	Monte Carlo simulation of the slow monopole trigger efficiency	61
3.9	Slow monopole trigger	63
3.10	Fast monopole trigger	65
3.11	WFD configurations	71

3.12	LED generated SPE pulse trains	72
3.13	Ground loop noise reduction	74
3.14	An ADC distribution for the sensitivity measurement	78
3.15	σ^2 vs. μ	79
3.16	SMT sensitivity curve at 90% efficiency	80
3.17	PMT gain variations	83
3.18	Sensitivities of the monopole trigger circuits (I)	85
3.19	Sensitivities of the monopole trigger circuits (II)	86
4.1	Effect of calculating livetime using scintillator muons	90
4.2	Livetime distribution for all data runs	92
4.3	Distribution of scintillator muon rates	94
4.4	Sample waveforms of single face slow monopole trigger events	97
4.5	Distribution of the two face slow monopole events	98
4.6	A randomly selected two face slow monopole event from run 2911	100
4.7	A randomly selected two face slow monopole event from runs 3245-3255	101
4.8	Distribution of times relative to the last scintillator muon event	102
4.9	Distribution of run numbers and relative times of the finally selected slow monopole candidates	104
4.10	Distribution of relative times of the finally selected slow monopole candidates	106
4.11	An event with bipolar oscillations	107
4.12	An event with simultaneous presence of long negative pulse trains in all channels	108
4.13	An event with featureless waveforms	109
4.14	A slow monopole candidate faked by a di-muon	111
4.15	Accidental coincidence between a muon and a radioactivity pileup	112
4.16	Accidental coincidence of radioactivity pileups (I)	113
4.17	Accidental coincidence of radioactivity pileups (II)	114
4.18	Accidental coincidence of radioactivity pileups (III)	115
4.19	Waveform of the best slow particle candidate	116
4.20	Postions of radioactivities	118
4.21	Waveform baseline subtraction	122

4.22	Maximum TOF of the fast monopole events	125
4.23	An FMT event: accidental coincidence of radioactivities	125
4.24	Muon waveform area distribution	126
4.25	Categorization of 194 FMT events which failed baseline-fitting	128
4.26	Double face charge cut	130
4.27	29 FMT events which passed the single face charge and width cut	131
4.28	Time of flight for the 58 fast monopole candidates	132
4.29	A muon accompanied by an accidental radioactivity	133
4.30	Charges of the eight final fast monopole candidates	134
4.31	An FMT candidate which is a stopping muon	135
4.32	An FMT candidate in which a muon crossed two supermodules	136
4.33	Acceptance of the first supermodule	139
4.34	Product of acceptance and livetime	140
4.35	Upper limits on GUT monopole flux	142
4.36	Upper limits on nuclearite flux	143
C.1	SMT trigger efficiency as a function of light level in MC	155
C.2	SMT sensitivity curves from Monte Carlo	156
C.3	SMT sensitivity curves from Monte Carlo and from LED measurement	157

List of Tables

3.1	Multiplexing scintillator counters into supercounters	68
3.2	Two sets of waveform digitizers	70
3.3	PMT gains	81
4.1	Run selections	95
4.2	Summary of cuts for slow monopole analysis	103
4.3	First cuts for the fast monopole analysis	123

Chapter 1

Introduction

... in this stone you should thoroughly comprehend there are two points of which one is called the North, the remaining one the South.

— *Petrus Peregrinus (1269 AD)*

During King Charles of Anjou's siege of the Saracen town of Lucera, Italy, in 1269AD, Petrus Peregrinus (Pierre de Maricourt) observed that all lines of force around a lodestone are concentrated at two points which he named the north and south poles [2]. Subsequent generations of scientists have confirmed that all magnets have these two inseparable poles, *i.e.*, all magnets are *dipoles*. Seven hundred years later, still in Italy, a much larger effort is being made to counter this observation; searches for *magnetic monopoles*, stable particles carrying single magnetic poles (or called magnetic charges), are being performed using the MACRO (**M**onopole, **A**strophysics and **C**osmic **R**ay **O**bservatory) detector at the Gran Sasso Laboratory, Italy, with renewed motivations and guidances from the modern particle theories. The topic of this thesis is a search for Grand Unified Theories (GUT) magnetic monopoles and other supermassive particles using the large scintillator detector of the first supermodule of the MACRO detector. In this chapter I shall summarize the theoretical aspects of and the previous experimental searches for GUT monopoles. I shall also describe concepts of other supermassive particles such as nuclearites and fractionally

charged superstring particles.

1.1 Magnetic Monopoles

Magnetic monopoles are a rich subject in the literature, vitally connected to particle theories, cosmology and astrophysics. Serious efforts have been made to search for them for decades. Preskill [3] has presented a thorough review on various aspects of monopole-related physics, especially the theoretical aspects. Groom [4] has given a detailed review on various bounds on monopole abundance obtained from astrophysical observations and direct terrestrial searches. In addition, this topic is covered in great breadth and depth in the conference proceedings [5, 6].

1.1.1 Monopoles before GUTs

For centuries, generations of thinkers have toyed with the idea that magnets may have isolated poles for many good reasons, among which is the elimination of the asymmetry between the electricity and the magnetism — positive and negative electric charge can easily be separated while all magnets are observed to be dipoles. However, the first good argument for the existence of magnetic monopoles was put forward by Dirac in 1931 [7]. He demonstrated that the existence of magnetic monopoles naturally leads to electric charge quantization. Electric charges have always been observed to be integer multiples of an elementary unit charge (the electron charge) ever since Millikan's oil drop experiments around the year of 1910 [8]. No other explanation was known for this fundamental and striking phenomenon of nature. Dirac showed that the magnetic charge g and the electron charge e must satisfy the Dirac quantization condition [7]

$$eg = \frac{n}{2}, \quad (1.1)$$

where n is an integer. Here we use the Gaussian unit system with the additional requirement of $\hbar = c = 1$ and thus the fine structure constant is $\alpha = e^2$ in this system. The minimum

allowed magnetic charge is the Dirac magnetic charge

$$g_{\text{D}} = \frac{1}{2e} = \frac{1}{2\alpha} e . \quad (1.2)$$

All magnetic charges are required to be integer multiples of this Dirac charge. Similarly, we can turn this argument around: suppose that there exists a magnetic monopole with charge g_{D} , then all electric charges are quantized to be integer multiples of the electron charge¹.

1.1.2 Monopoles and GUTs

Many particle physicists hold dearly the belief that all observed fundamental interactions between particles may be governed by a single unified law of nature. In particular, the strong and electroweak gauge interactions, which possess three apparently independent coupling constants, have been conjectured [10] to become unified at exceedingly short distances as a single gauge interaction with a single coupling constant (Fig. 1.1). Among the successful predictions of such “grand unified” theories (GUTs) is that the predicted value [11] of the Weinberg angle (the weak mixing angle) is verified by experiments. It has been demonstrated that magnetic monopoles must exist in any GUTs. In 1974 ‘t Hooft [12] and Polyakov [13] independently showed that magnetic monopoles, as one type of topologically stable configurations of gauge and Higgs fields, are a necessary consequence of any unified gauge theory in which the electromagnetic $U(1)_{\text{em}}$ group is embedded in a non-Abelian simple or semisimple² group. It is interesting to point out that electric charge is automatically quantized in any such unified gauge theory [10].

¹This does not contradict our belief that quarks exist. Since quarks are confined in quantum chromodynamics (QCD), the apparent contradiction between the minimum magnetic charge g_{D} and the fractional charges of quarks can be resolved if the magnetic monopole carrying charge g_{D} also carries color-magnetic charge [9, 3]. However, if there exist *free* fractionally charged particles (section 1.2.2), the minimum magnetic charge can no longer be g_{D} , unless there is some other (as yet unknown) long range interaction between the magnetic monopole and the fractionally charged particle.

²A Lie algebra is simple if it does not have any non-trivial invariant subalgebra; it is semisimple if it does not have a non-trivial Abelian invariant subalgebra. Hence the standard electroweak theory $SU(2) \otimes U(1)$ does not satisfy this criterion, and thus does not introduce ‘t Hooft-Polyakov magnetic monopoles.

All GUT models are based on a large group G (the simplest one is $SU(5)$) of exact gauge symmetries, which mix the strong and electroweak interactions. These symmetries undergo a spontaneous symmetry breaking,

$$G \xrightarrow{M_X} SU(3) \otimes SU(2) \otimes U(1) , \quad (1.3)$$

at an extremely short distance scale M_X^{-1} , or an extremely large mass scale M_X . This unification scale M_X is the mass scale of X vector bosons mediating the unified force. The prediction that magnetic monopoles must exist does not depend on the detailed mechanism of the symmetry breakdown.

While Dirac [7] showed the consistency of magnetic monopoles with quantum electrodynamics, 't Hooft [12] and Polyakov [13] demonstrated the necessity of magnetic monopoles in grand unification. Dirac derived that the magnetic charge must be an integer multiple of the Dirac charge g_D , but he did not predict any other properties of the magnetic monopole, such as its mass. For comparison, properties of the 't Hooft-Polyakov monopole can be predicted in a given GUT model. The typical magnetic charge of the GUT monopole is the Dirac charge g_D , which is concentrated in a core of size $R \approx M_X^{-1}$. The mass of the GUT monopole is comparable to the magnetostatic potential energy stored in the core, which is calculated to be $m \approx M_X/\alpha_X$, where α_X is the *running* coupling constant at the unification scale. A monopole's Compton wavelength m^{-1} is much smaller than its core size, and thus it is essentially a "classical" object.

The unification scale M_X varies in different GUT models, but it is calculable under the *desert hypothesis* — a very strong assumption that no new interactions or particles should appear between the present day energies (~ 100 GeV) and the unification scale, *i.e.*, no new physics beyond the standard model (SM) but the GUTs. Previous calculations based on this hypothesis showed that $M_X \approx 10^{14}$ GeV and $\alpha_X \approx 1/40$ [11,3], correspondingly, the monopole core size is $R \approx 10^{-28}$ cm and the monopole mass is $m \approx 10^{16}$ GeV. However, the minimal $SU(5)$ GUT model with the desert hypothesis predicts too short a proton lifetime, contradicting with the recent results from the proton decay experiments [14].

Furthermore, the LEP precision measurements of the three coupling constants at the energy scale of the Z-boson mass indicate that the three coupling constants cannot be unified into a single coupling constant in the minimal standard model (*i.e.*, under the desert hypothesis); that is, they do not meet at a single point when extrapolated to the unification scale (Fig. 1.1A). On the contrary, the minimal supersymmetric extension to the standard model (MSSM) [16] gives unification — the three couplings evolve and meet at a single point (Fig. 1.1B) and it is calculated that [15]

$$M_X = 10^{15.8 \pm 0.4} \text{ GeV} \quad \text{and} \quad \alpha_X^{-1} = 26.3 \pm 2.9 . \quad (1.4)$$

The SU(5) unification with the MSSM predicts the proton lifetime to be $10^{34.5 \pm 1.2}$ years [15], not yet reached by the experimental limits. Some other GUT models also give similar M_X and α_X (thus similar proton lifetime) as in the MSSM [15]. This implies that the GUT monopole has a mass larger than as previously calculated under the desert hypothesis. We summarize the properties of GUT monopoles as following:

$$\begin{aligned} \text{Magnetic Charge:} \quad & g = g_D = \frac{1}{2\alpha} e , \\ \text{Core Size:} \quad & R \approx M_X^{-1} \approx 10^{-30} \text{ cm}, \\ \text{Mass:} \quad & m \approx M_X / \alpha_X \approx 10^{17} \text{ GeV} \approx 10^{-7} \text{ g} \approx 10^7 \text{ J} . \end{aligned} \quad (1.5)$$

It is worthwhile to point out that the sensitivity of the monopole search in this thesis, which will be discussed in more detail later, does *not* depend on the exact values of monopole mass or core size.

A variety of superstring models also predict the existence of supermassive magnetic monopoles, but the minimum magnetic charge may be an integer multiple of the Dirac charge g_D (see, for example, [17, 18]), making their detection easier.

1.1.3 Monopoles and Cosmology

If the monopole mass is indeed as large as 10^{17} GeV, it is not surprising that monopoles have not been observed in accelerator experiments and we do not expect to produce monopoles

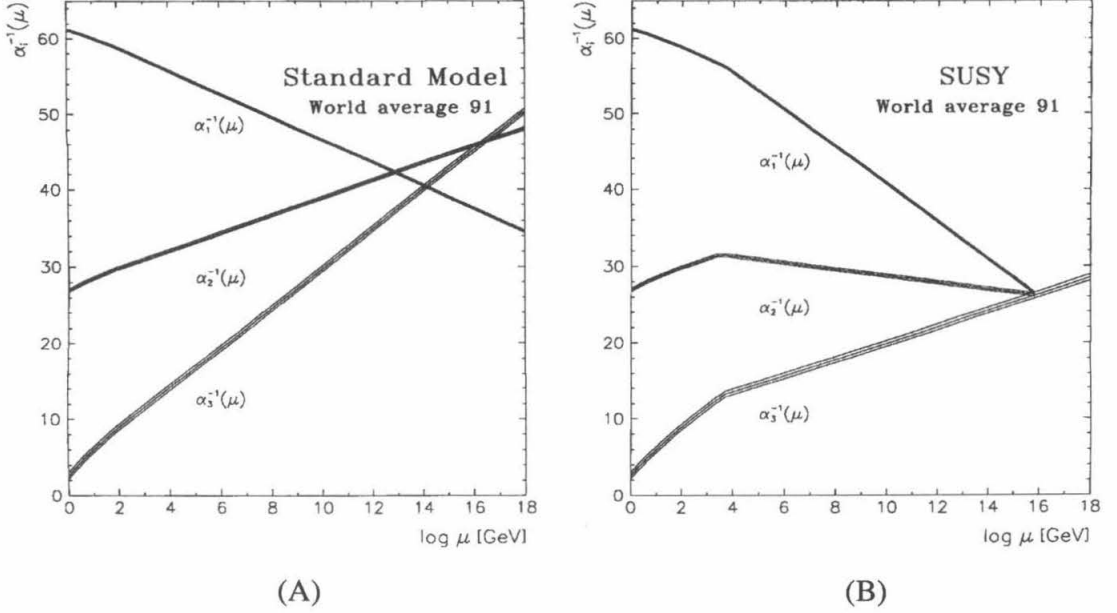


Figure 1.1: Evolution of the inverse of the three running coupling constants, (A) in the minimal standard model, (B) in the minimal supersymmetric (SUSY) extension to the standard model. The evolution is calculated using the renormalization group equations. The 1991 world average (mainly determined by the LEP data) of the coupling constants at the low energies were used in the calculations. The three coupling constants are defined as [15]

$$\begin{aligned} \alpha_1 &= (5/3)g'^2/(4\pi) = 5\alpha/(3\cos^2\theta_W), \\ \alpha_2 &= g^2/(4\pi) = \alpha/\sin^2\theta_W, \\ \alpha_3 &= g_s^2/(4\pi), \end{aligned}$$

where g' , g and g_s are respectively the couplings of the groups U(1), SU(2) and SU(3) in the standard model, α is the fine structure constant and θ_W is the Weinberg angle. The factor 5/3 in the definition of α_1 is included for the proper normalization at the unification scale [11]. Reprinted from reference [15].

with accelerators in the foreseeable future. The only place to find a monopole seems to be in cosmic rays. But since no known process in the present universe is energetic enough to produce monopoles, any monopoles around today must be relics of the very early universe. Immediately after the big bang, the universe was so hot that processes occurred which were sufficiently energetic to produce monopoles. For a review on early universe cosmology, see reference [19].

As the universe cooled down, it underwent a phase transition at a critical temperature T_C of the order of the unification scale M_X , accompanied by the spontaneous symmetry breaking of the GUT gauge symmetry, which was fully restored when the temperature was above T_C . In the phase transition, monopoles as “topological defects” were frozen in, and roughly one monopole was created per horizon volume [20]. The horizon is the fraction of the universe which is in causal contact. After monopoles were produced, their density per comoving volume can be reduced only by monopole-antimonopole annihilation, because monopoles are stable. Preskill [21] showed that the annihilation is negligible and the density of monopoles is roughly the same as the density of baryons in the standard cosmology. This is the so-called “monopole problem:” the monopole is about 10^{17} times heavier than the baryon, and thus the resulting cosmic mass density is absurdly large compared with the limit of the present mass density of the universe.

Among many solutions to this problem, the inflationary universe scenario [22, 23, 3] seems most attractive. In this scenario, there was an epoch in the early history of the universe in which the universe was “inflating” exponentially as a function of time. During the inflation epoch, monopoles were “inflated away.” This scenario significantly suppresses the monopole density, but predictions for the monopole abundance vary greatly in different models.

The monopole problem has influenced the development of cosmology. However, cosmology offers essentially no guidance to us, the monopole hunters; it gives no definite prediction for the monopole abundance.

1.1.4 Monopole and Astrophysics

Because the relic monopoles have been roaming around in the universe since their production in the very early universe, they inevitably interact with various astrophysical objects via gravitational or magnetic forces. That is why monopoles are connected with astrophysics. This connection gives estimates on monopole velocities and upper bounds on the monopole flux.

Monopole Velocities

As the relic of the big bang, an isolated monopole gas would by now have cooled to 10^{-8} Kelvin and its present thermal velocities would be [19]

$$\langle v^2 \rangle^{1/2} \approx \sqrt{T/m} \approx m_{17}^{-1/2} 10^{-19} c, \quad (1.6)$$

where $m = m_{17} 10^{17}$ GeV is the monopole mass and c is the speed of light. Obviously, these monopoles should have been accelerated by gravitational and magnetic forces. The maximum velocity that can be acquired through gravitational force is the galactic escape velocity $\sim 10^{-2} c$. It has been measured that the galactic magnetic field has a strength B of $\sim 3 \mu\text{G}$ [24]. The field is chaotic over large scales but coherent over a scale L of ~ 300 pc ($\sim 10^{21}$ cm). In traversing one coherent region, a monopole acquires a velocity of

$$v_{\text{mag}} = (2g_D B L / m)^{1/2} \approx m_{17}^{-1/2} 10^{-3} c. \quad (1.7)$$

Thus, the supermassive monopoles have to be slow-moving. They could exist in one of the following states [4]:

1. Monopoles are not gravitationally bound to our galaxy or supercluster. When an extragalactic monopole falls through our galaxy and reaches the earth, it acquires a velocity of the order of $\sim 10^{-2} c$, the galactic escape velocities.
2. Monopoles are bound to the galaxy or the local supercluster, and thus they travel at the galactic circular velocities $\sim 10^{-3} c$ ($3 \times 10^{-3} c$ for the supercluster).

3. Monopoles are bound to the solar system [25, 26]. Their typical velocities are $\sim 10^{-4}c$, the velocity of the earth orbiting around the sun. The minimum velocity expected of a monopole in cosmic rays is the earth escape velocity $3.7 \times 10^{-5}c$.

Overall, monopoles could pass through a terrestrial detector with any velocities in the range $3.7 \times 10^{-5} < \beta < 10^{-2}$, but galactic velocities $\sim 10^{-3}c$ seem to be more likely because it is more probable for monopoles to be clustered in our galaxy.

Parker Bound

In traversing the galaxy, monopoles are accelerated by the galactic magnetic field, and thus extract energy from the field. The rate of this energy reduction must not exceed the rate at which the field regenerates itself, otherwise the field would have been destroyed. Thus, the survival of the galactic magnetic field allows us to establish an upper limit on the flux of magnetic monopoles, which is called the Parker bound because Parker [27] originally explored this problem. Taking into account the chaotic nature of the galactic magnetic field, Turner, Parker and Bogdan [24] reexamined this subject and obtained

$$F \lesssim \begin{cases} m_{17} v_3^2 10^{-15} \text{cm}^{-2} \text{sr}^{-1} \text{sec}^{-1}, & \text{if } v \gtrsim v_{\text{mag}} \\ 10^{-15} \text{cm}^{-2} \text{sr}^{-1} \text{sec}^{-1}, & \text{if } v \lesssim v_{\text{mag}} \end{cases} \quad (1.8)$$

where $v = v_3 10^{-3}c$ is the monopole velocity and v_{mag} is given in Eq. 1.7. The same arguments are applied to the intracluster magnetic field and a flux limit at least three orders of magnitude more stringent than the Parker bound is obtained [28], but this limit is less reliable because our knowledge of the existence and the persistence of the intracluster magnetic fields is less secure.

With the consideration of monopole dynamics in the superconducting core of a neutron star pulsar, the field survival in the pulsar gives an upper limit of supermassive monopole flux in the pulsar neighborhood [29]. Depending strongly on the age τ of the pulsar magnetic field ($F_{\text{max}} \propto \tau^{-2}$), this limit is hardly stringent for most pulsars ($\tau \lesssim 10^6$ yr).

But the millisecond pulsar PSR 1937+214, thought to be more than 10^9 yr old, leads to the most stringent flux limit $5 \times 10^{-22} v_3^2 \text{ cm}^{-2} \text{ sr}^{-1} \text{ sec}^{-1}$ [4]. However, it is less reliable than the Parker bound because of the uncertainty in the evolution history and the age τ of the pulsar magnetic field.

If monopoles are uniformly distributed in the universe, the present mass density of the universe provides an upper bound to the average number density of monopoles, or a flux limit [19]

$$F \lesssim m_{17}^{-1} v_3 10^{-15} \text{ cm}^{-2} \text{ sr}^{-1} \text{ sec}^{-1} . \quad (1.9)$$

If monopoles are clustered in our galaxy, the local mass density of the galactic “halo” as indicated by the rotation curve offers a significantly greater upper limit on the monopole flux [19]

$$F \lesssim m_{17}^{-1} v_3 10^{-11} \text{ cm}^{-2} \text{ sr}^{-1} \text{ sec}^{-1} . \quad (1.10)$$

This limit has been exceeded by experimental searches for much of the plausible monopole mass and velocity ranges; the present combined upper limit on monopole flux from all induction experiments (the most definitive monopole search technique) is $2.2 \times 10^{-13} \text{ cm}^{-2} \text{ sr}^{-1} \text{ sec}^{-1}$ [30], demonstrating that it is unlikely for magnetic monopoles to be the major constituent of the local galactic halo, unless monopoles are heavier than the Planck mass. The limit in Eq. 1.9 does not apply if monopoles are clustered in our galaxy. So the most reliable astrophysical flux limit is the Parker bound, which is plotted in Fig. 4.35 on page 142. To search for monopoles at the flux level of the Parker bound , a detector of football field size is needed.

1.1.5 Previous Monopole Searches

GUT monopoles are so supermassive that the attempts to search for them in accelerator experiments [31] are irrelevant. They can only be produced in the hot early universe, so the relic monopoles are searched for in cosmic rays. Although slowly moving, the

supermassive monopoles are very penetrating due to their large kinetic energy. The energy loss in rock of a magnetic monopole with $\beta = v/c \lesssim 0.01$ surely does not much exceed [32]

$$\frac{dE}{dx} \sim 100\beta \text{ GeV/cm} . \quad (1.11)$$

Thus, the range in rock of a $\beta \sim 10^{-3}$ monopole with mass $\sim 10^{17}$ GeV is larger than 10^{12} cm; the monopole passes through the earth without slowing down. This fact has two implications: it is unlikely for the penetrating monopoles to be trapped in the earth or the moon, making the searches for them in terrestrial material [33] or in lunar rock [34] hardly relevant. On the other hand, searches for penetrating monopoles in cosmic rays may be conducted using underground detectors, which reduces background from cosmic rays. This is a tremendous advantage for any detector except induction detectors for which cosmic rays do not constitute a background.

In this section, I shall briefly review the various experimental techniques for searches for magnetic monopoles in cosmic rays and summarize the flux limits from previous searches. For the sake of brevity, I shall cite only those experiments that have established more significant flux limits. These limits are plotted in Fig. 4.35 on page 142. All limits are quoted at 90% confidence level.

Induction Technique

If a magnetic monopole passes through a superconducting loop, it induces a measurable quantized current. Compared to other approaches, the induction technique is unambiguous and definitive. It uses the unique property of a magnetic monopole, its magnetic charge, and does not depend on any other characteristics, such as the monopole velocity, mass, or electric charge. As will be described below, ionization and excitation detectors are not sensitive to monopoles moving too slowly; both the mica technique and the Drell mechanism are insensitive to monopoles that carry positive electric charge (dyons³). However, it is

³Dyons, particles that carry both magnetic and electric charge, arise automatically as quantum mechanical excitations of magnetic monopoles [3, 35]. In addition, by dyons we also mean monopole-proton bound states.

technically difficult and economically expensive to build a large superconducting induction detector, making other options attractive. Using a fully coincident superconducting induction detector with an acceptance $A\Omega = 4\pi\text{m}^2\text{sr}$, Bermon *et al.* established an upper limit of monopole flux of $3.8 \times 10^{-13}\text{cm}^{-2}\text{sr}^{-1}\text{sec}^{-1}$ [30]; with an eight-loop superconducting detector of sensing area 1.1m^2 , Huber *et al.* set a limit of $7.2 \times 10^{-13}\text{cm}^{-2}\text{sr}^{-1}\text{sec}^{-1}$ [36]. The present global-combined induction limit is $2.2 \times 10^{-13}\text{cm}^{-2}\text{sr}^{-1}\text{sec}^{-1}$ [30].

Scintillation Counters

In traversing scintillator, electrically or magnetically charged particles lose energy by ionizing electrons or exciting electrons to higher energy levels. The energy loss is subsequently converted to light, measurable using phototubes. Progress has been made in understanding the scintillation light yield of slow monopoles, but some uncertainties still persist; a little more is to be said in section 3.1.1 about this subject. Usually scintillator detectors are only sensitive to $\beta \gtrsim 10^{-3}$ monopoles, unless special efforts are made in designing the detectors; the specialized trigger scheme in the MACRO detector is able to select monopoles of lower velocities (Chapter 3). Compared to cryogenic induction technique, both scintillator counters and gaseous detectors described below are mature technologies and it is relatively easy and inexpensive to build a large detector out of them.

Among the many scintillator detectors [37–41,4] built to search for monopoles, the best flux limit to date was set by the Baksan detector [37] located 850hg cm^{-2} underground in the Caucasus Mountains. The detector consists of four horizontal layers of liquid scintillator counters and is enclosed by vertical layers on the sides. The total acceptance for isotropic trajectories is $A\Omega = 1850\text{m}^2\text{sr}$ and the accumulated livetime is 5.8 years. The absence of candidates yields a flux upper limit of $6.8 \times 10^{-16}\text{cm}^{-2}\text{sr}^{-1}\text{sec}^{-1}$ for monopoles in the velocity range $10^{-3} < \beta < 0.1$.

Gaseous Detectors

Gaseous detectors like streamer tubes and multiwire proportional chambers have long been used in particle physics to detect charged particles through the ionization of gas. Typically they have difficulties in detecting particles with velocities smaller than $\sim 10^{-3}c$. However, gaseous detectors that employ the Drell mechanism and the Penning effect can be sensitive to magnetic monopoles as slow as $\sim 10^{-4}c$. Drell *et al.* [42, 43] have presented an elegant treatment of monopole energy loss in atomic hydrogen and helium. When a monopole passes nearby an atom (say, helium), the atomic energy levels get mixed because of the Zeeman splitting and the ground state electrons evolve adiabatically into an excited state. The excited helium atom de-excites through collision with another gas component (for example, methane) and the collisional energy transfer is sufficient to ionize the second gas species if chosen properly (the Penning effect [44]). Attempts [45] have been made to apply this treatment to more complicated atoms such as argon (often used in gaseous detectors), but the success is limited. A caveat to the Drell mechanism deserves mentioning: for positively charged dyons, the Drell effect is reduced so severely due to electrostatic interaction that it is no longer interesting for practical detectors [43].

A group from University of California at San Diego (UCSD) [46] built an array of He-CH₄ proportional tube to search for monopoles via the Drell mechanism. The detector has an acceptance of 265m²sr and sets a flux limit of $1.8 \times 10^{-14}\text{cm}^{-2}\text{sr}^{-1}\text{sec}^{-1}$ for $\beta > 1.1 \times 10^{-4}$. The low β part ($\beta \lesssim 10^{-3}$) of this limit is obtained by invoking the Drell mechanism, and thus is valid only for bare monopoles and negatively charged dyons.

The Soudan 2 detector, an underground (2100 hg cm⁻²) tracking calorimeter using Ar-CO₂ gas, is being built for nucleon decay. Part of the detector has been employed to search for highly ionizing tracks left behind by traversing magnetic monopoles and a flux limit of $8.7 \times 10^{-15}\text{cm}^{-2}\text{sr}^{-1}\text{sec}^{-1}$ has been set for $\beta > 2 \times 10^{-3}$ monopoles [47].

Track-etch Detectors

In passing through matter, an ionizing particle leaves behind a trail of local radiation damages. In track-etch material, the damaged sites are more chemically reactive, and thus etch at a higher rate than the surrounding undamaged bulk if strong chemical reagents (*e.g.*, NaOH solutions) are applied to the material. Thus, the particle track manifests itself as a hole through the track-etch sheet for a strong etching or a cone on each side of the sheet for a moderate etching. The angle of the cone depends on the type of track-etch material and the electronic and nuclear stopping power of the traversing particle. The most frequently used materials are ancient mica and polycarbonate plastics CR-39 and Lexan. Incidentally, CR-39 is the material used for manufacturing eyeglasses. In current theories of monopole energy loss, Lexan is only sensitive to monopoles with velocities greater than $\sim 0.3c$, CR-39 is sensitive to slower monopoles, and mica is only sensitive to monopoles that have captured nuclei.

CR-39 The best limit on monopole flux to date achieved with CR-39 is reported by Orito *et al.* [48]. A 2000 m^2 array of CR-39 track-etch detectors was deployed underground at a depth of 10^2 hg cm^{-2} . With 2.1 years of operations, the nonobservation of penetrating tracks placed a velocity-dependent flux limit which is shown in Fig. 4.35 on page 142. However, the vast majority of CR-39 calibrations are performed with $\beta > 10^{-2}$ fast ions. The only measurements so far for the low β response of CR-39 comes from Snowden-Ifft and Price [49], showing a higher threshold for detection of slow ions compared to that of fast ones, and thus invalidating the previous limits set by Price [50] on monopoles with velocities between $\beta = 3 \times (10^{-5} - 10^{-2})$ until further work is done. Although this result is obtained with a specific type of CR-39, it raises a general question about the sensitivity of CR-39 in the low β region and certainly suggests that at least a test of the CR-39 used by Orito *et al.* with low β ions is needed in order to establish a firm flux limit over the quoted β range.

Ancient Mica Taking advantage of the long exposure time ($> 10^8$ yr) of naturally occurring underground mica, Ghosh *et al.* [51] and Price *et al.* [52,53] have set very stringent flux limits for $\beta \approx 10^{-3}$ monopoles at the order of $10^{-18} \text{cm}^{-2} \text{sr}^{-1} \text{sec}^{-1}$. These limits are not shown in Fig. 4.35 because of the many loopholes in mica searches which have been pointed out originally by Price *et al.* [53] and then summarized by Groom [4]. Here we only make two points: (1) Monopole track might anneal at a different rate than the recoil and fission fragment tracks used to confirm the age-dating. (2) Mica is sensitive to monopoles that have captured $Z \geq 8$ nuclei [52] (*e.g.*, ^{27}Al) through magnetic dipole-magnetic monopole interaction as they traverse the earth. Coulomb barriers prevent positively charged dyons from picking up high- Z nuclei. Thus, the mica searches are invalid for positively charged dyons. Even for bare monopoles, Bracci *et al.* [54] have argued that monopoles would most likely have captured protons in the early universe and formed monopole-proton bound states. If true, the mica searches are also invalid even for bare monopoles.

Catalysis of Nucleon Decay

Because the core of the GUT monopole contains the baryon number violating grand unified gauge and Higgs fields, Rubakov [55] and Callan [56] have conjectured that magnetic monopoles may catalyze nucleon decay. Based on this assertion, many limits on monopole flux have been obtained, using astrophysical observations or terrestrial detectors. These limits depends strongly on the catalysis cross section, which is a very controversial theoretical subject: no theorists agree with each other. For a review, see references [3,4].

1.1.6 Summary

Most likely the strong and the electroweak interactions are unified at extremely short distances. Any such grand unified theories necessarily contain magnetic monopoles. Typical GUT monopoles carry the Dirac charge and are predicted to be supermassive ($\sim 10^{17}$ GeV), as shown in Eq. 1.5. Monopoles may bind protons or other nuclei, or they

may carry intrinsic electric charge. Such supermassive monopoles can only be produced in the hot early universe, so the relic monopoles are searched for in cosmic rays. Detection of monopoles is not only a strong confirmation that the idea of the grand unification is correct, but also a direct evidence that the universe was once very hot. The supermassive monopoles must be slow-moving and very penetrating. The survival of the galactic magnetic field suggests that the monopole flux cannot exceed the Parker bound and no previous terrestrial searches have achieved this low flux level over all possible velocity range. Hence we have been building the MACRO detector.

1.2 Other Supermassive Particles

The main physics goal of this thesis is to search for GUT monopoles. But this search applies to any other types of penetrating, slow-moving and scintillating particles. To be penetrating, any non-relativistic particles must be supermassive. This section offers a brief review on two other types of supermassive particles — nuclearites from QCD and supermassive fractionally (electrically) charged particles from superstring theory.

1.2.1 Nuclearites

It has been proposed [57–59] that *strange quark matter* (SQM), a color-singlet lump of up, down and strange quarks in approximately equal proportions, may be the true QCD ground state. A review on this subject is given by [60]. Various aspects of SQM are dealt with extensively in the conference proceeding [61].

Ordinary nuclei are made of protons and neutrons and thus have an energy density of ~ 938 MeV per nucleon. We could imagine that the constituents of nucleons (up and down quarks and gluons) exist in a different state — quark matter. In quark matter, the quarks are not locally confined to form nucleons and they freely move around inside the nucleus; in a sense the quark matter behaves like a Fermi gas of quarks. The two-flavored quark

matter apparently has a higher energy density than ordinary nuclei, otherwise ordinary nuclei would decay into quark matter.

With the inclusion of strange quarks, the three-flavored strange quark matter differs energetically from the two-flavored ordinary quark matter in two ways: strange quarks are more massive than up and down quarks. On the other hand, the inclusion of the third species of quarks reduces the Fermi energy level, according to the Pauli exclusion principle. Witten [57] has conjectured that the second effect may be stronger than the first one and thus SQM may have lower energy density than ordinary nuclei. The detailed calculations by Farhi and Jaffe [58] using the MIT hadron bag model have shown that this conjecture is plausible within the uncertainty inherent in a QCD calculation. SQM obeys the saturation properties analogous to the corresponding saturation condition of nuclear forces: the energy per baryon (E/A) and the baryonic number density do not depend on the total number of quarks (at least to first order). The nuggets of SQM may be stable over a wide range of baryon numbers A (one third of the total quark numbers) from ~ 100 to $\sim 10^{57}$. The upper limit is determined by instability against gravitational collapse. There are speculations [60] that neutron stars may be strange stars, stars made of strange quark matter.

The existence of ordinary nuclei does not exclude the possibility that SQM may be more stable. If SQM is indeed more energetically favored, the decay of an ordinary nucleus (*e.g.*, iron) to SQM is energetically allowed, but roughly one third of its up and down quarks would have to become strange *simultaneously*. The conversion of a single quark of a proton or neutron to a strange quark produces an energetically-disfavored hyperon, and thus is prohibited. Therefore, the rate of decay of nuclei into SQM is greatly suppressed by many powers of G_F (the Fermi coupling for the weak interaction) and becomes practically vanishing even in the cosmological time scale. So SQM may be more stable than iron and we would not have noticed.

Strange quark matter may have been produced during the QCD phase transition from

a quark-gluon plasma to a gas of hadrons in the early universe, or may be produced during a neutron star collision [57]. It is an attractive dark matter candidate; if proved successful, the dark matter problem would be solved within the QCD frame and no exotic physics would need to be invoked.

De Rújula and Glashow [59] have suggested that strange quark matter may exist in cosmic rays and they refer to such cosmic ray SQM as *nuclearites* (nuclear meteorites). Because of their huge mass, nuclearites are expected to travel at galactic velocities ($\sim 10^{-3} c$). Due to the wide range of nuclearite masses, searching for them requires very different experimental techniques in different mass regions. These include techniques from mass-spectrometer searches in earth materials [59, 61] to searches for natural disasters caused by large nuclearites hitting the earth [59] to searches for very small SQM (strangelets) in heavy ion accelerator experiments [62, 61]. A number of cosmic ray searches have been performed at various altitudes with different techniques and some of the monopole searches can also be interpreted to provide limits on nuclearite flux. These include searches using scintillator detectors [63, 38, 64], ancient mica [65, 51–53], plastic track-etch detectors [48, 65, 66], balloon-borne detectors [67], and a gravitational wave detector [68].

1.2.2 Fractionally Charged Superstring Particles

Wen and Witten [17] have demonstrated the existence of un-confined and color singlet particles with fractional electric charge in superstring models in which a grand unified $O(10)$ or E_6 gauge group is broken. Conversely, the minimal magnetic charge of a superstring magnetic monopole is an integer multiple of the Dirac charge g_D . These fractionally charged particles are predicted to carry a mass of the order of Planck mass (10^{19} GeV). They could very well exist in cosmic rays and travel at galactic velocities $10^{-3} c$, similar as magnetic monopoles and nuclearites. These particles are also searched for in this thesis.

Chapter 2

The MACRO Detector

This chapter describes in detail the apparatus of the first supermodule of the MACRO detector from which the data in this thesis is obtained, concentrating on the aspects related to the GUT monopole searches. A more general description of the first supermodule can be found in reference [69]. In addition to its primary goal of searches for supermassive particles, the MACRO experiment has many other physics objectives, *e.g.*, studies on the primary cosmic ray composition [70], searches for neutrino bursts emitted in gravitational stellar collapses [71], studies on muon astronomy [72], etc. However, these topics are not the subject of this thesis.

2.1 The Gran Sasso Laboratory

The MACRO detector occupies one of the large underground experimental halls of the Gran Sasso National Laboratory of Italy. About 137 km east of Rome, the Gran Sasso Laboratory is located near the town of Assergi in the Abruzzo region in Central Italy (Fig. 2.1) and it is right under the Gran Sasso Mountain after which it is named. The underground experimental halls are built off the Rome-Teramo highway tunnels and can be accessed by automobiles. The geographical coordinates are $13^{\circ}34'28''\text{E}$ in longitude



Figure 2.1: Geographical Map of Central Italy.

(with respect to the Greenwich meridian) and $42^{\circ}27'09''N$ in latitude. The altitude is 963 m above sea level and the rock overburden has a minimum thickness of 3200 hg/cm^2 . This overburden absorbs almost all cosmic ray radiations and attenuates their flux by a factor of about 10^6 , thus significantly reducing the background for detection of rare phenomena such as GUT monopoles.

2.2 General Description of the MACRO Detector

The primary physics goal of the MACRO experiment is to search for GUT magnetic monopoles at a flux level below the Parker bound (page 9). This dictates the strategies in designing the MACRO detector: it must have a large acceptance in order to search for particles at such a low flux level; if a candidate is found, it must have sufficient

redundancy to convince people that the candidate is not of a spurious origin. As discussed in section 1.1.5, the induction technique is the most definitive method to search for magnetic monopoles, but it is technically difficult and prohibitively expensive to build a large acceptance detector consisting of superconducting devices. Therefore, MACRO uses three relatively inexpensive detectors to achieve the large acceptance and redundancy: liquid scintillator counters, limited streamer tubes and track-etch detectors; they can be deployed at a large scale for a modest cost and without any outstanding technical difficulties. These three complementary techniques allow multi-signatures for GUT monopoles and other rare events. When completed, the MACRO detector will have an acceptance of about $10,000 \text{ m}^2\text{sr}$ for penetrating particles with isotropic fluxes, allowing a sensitive search for GUT monopoles below the Parker bound. For comparison, the first supermodule, the part of the detector used in this thesis, has an acceptance of $870 \text{ m}^2\text{sr}$ for isotropic particles.

2.2.1 Mechanical Structure

The MACRO detector has a modular structure as shown in Fig. 2.2. It consists of six *supermodules* with overall dimensions of $78 \text{ m} \times 12 \text{ m} \times 9 \text{ m}$. The total length of 78 m includes gaps between supermodules, occupied by the supporting structure of the apparatus. Each supermodule has a horizontal cross section of $12 \text{ m} \times 12 \text{ m}$ and consists of two decks. The lower deck is 4.8 m in height and together with the upper deck the total height is 9 m. As of this writing (early 1993), the lower deck of all six supermodules has been turned on and the upper deck is being constructed. The *lower deck of the first supermodule* had its first engineering run from February to May 1989. After being improved in summer 1989, it had a continuous data-taking run from October 1989 to November 1991, from which data used in this thesis were obtained (*cf.* section 3.4). These runs serve two purposes: even with only about 1/12 of the full detector, they are capable of making significant contributions to some physics topics; the first supermodule also serves as a prototype of the larger detector.

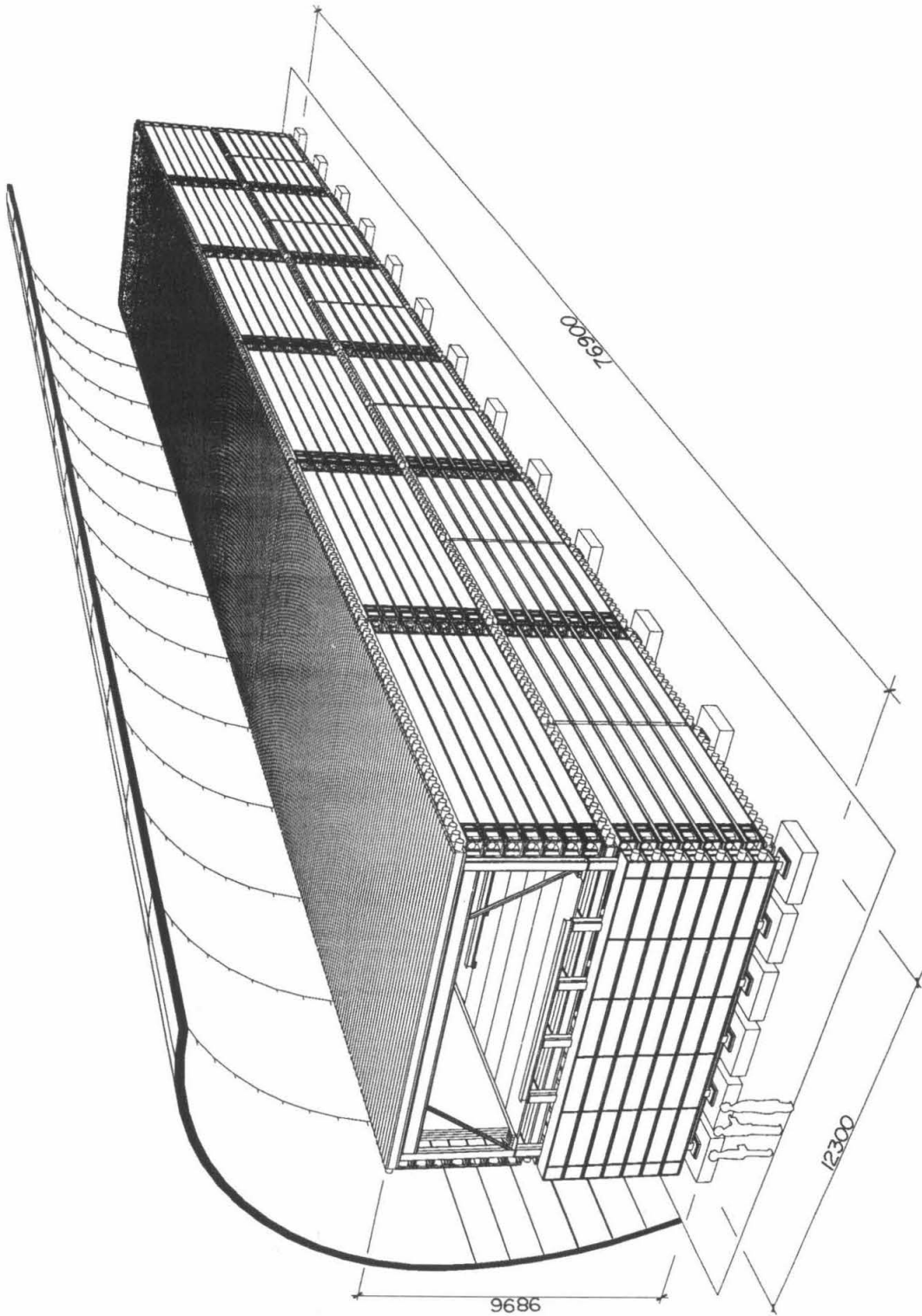


Figure 2.2: General structure of the full MACRO detector.

A cross-sectional end view of the first supermodule¹ is shown in Fig. 2.3. The body of the first supermodule is surrounded by large liquid scintillator counters except on the south side². Each horizontal scintillator layer is placed between two planes of limited streamer tubes. Three planes of streamer tubes are vertically placed on each side of every vertical scintillator layer. Inside the aforementioned detector elements lies a sandwich consisting of six more horizontal planes of streamer tubes, separated by seven layers of passive absorber. Thus, in the first supermodule there are ten $12\text{ m} \times 12\text{ m}$ horizontal planes and eighteen $4.8\text{ m} \times 12\text{ m}$ vertical planes of streamer tubes. The absorber is made of crushed rock (CaCO_3) and iron and each layer is about 60 g/cm^2 thick. It absorbs heavily-ionizing particles such as delta rays and showers. With a total thickness of $\sim 4.2\text{ hg/cm}^2$, the absorber sets an energy threshold of about 1 GeV for muons to cross the detector vertically. A horizontal layer of passive track-etch detectors is placed in the middle of the supermodule, providing additional redundancy for monopole searches. In the remaining part of this section, I shall describe the streamer tubes and the track-etch detectors. The scintillator counters, from which the data used in this thesis are obtained, will be described in more detail in next section.

2.2.2 Streamer Tubes

The MACRO streamer tubes [69] have two-fold goals: the good space resolution allows the reconstruction of tracks of traversing ionizing particles like cosmic ray muons; the helium-dominated gas mixture allows the exploitation of the Drell mechanism [42] for searches for GUT monopoles at very low velocities (possibly down to $\sim 10^{-4}c$). The first supermodule has been operated with different gas mixtures. The gas mixture finally chosen is helium (73%) and n-pentane (27%). The streamer tubes operate in the limited streamer mode [73] so that they have very high efficiency. Taking advantage of the

¹Hereafter, the term “*the first supermodule*” means its *lower deck*.

²The second supermodule is placed immediately south of the first supermodule, so the south face of the first supermodule is not instrumented with any active detector elements.

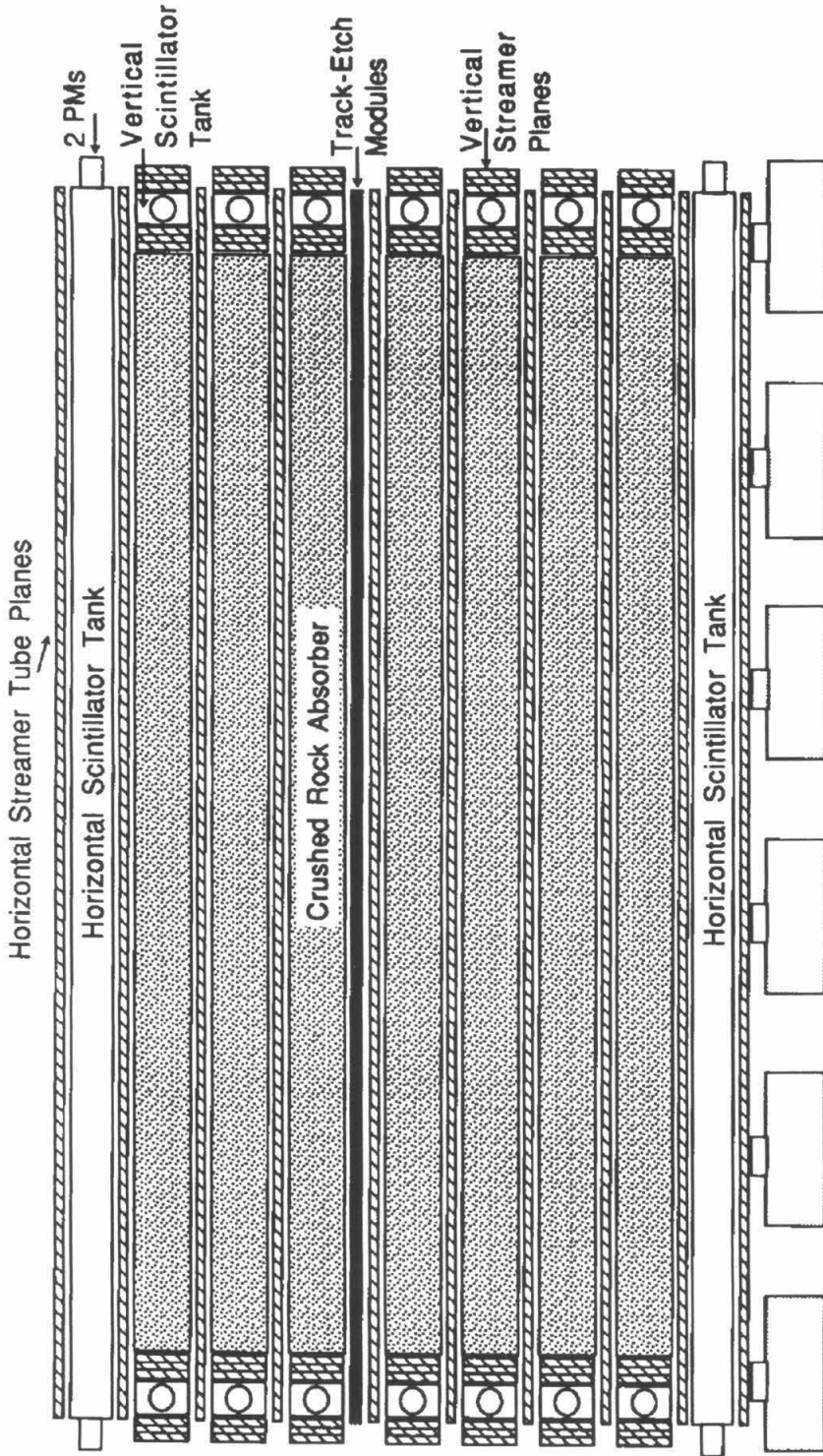


Figure 2.3: Cross-sectional end view (not to scale) of the lower deck of the first supermodule.

resistive cathode technique [74], the horizontal streamer tube planes are instrumented with the external pick-up strips. The strips make an angle of 26.5° with the streamer wires, allowing three-dimensional readout of the track hits. The space resolution for the tracking reconstruction is about 1 cm, resulting in an angular resolution of about 0.2° . However, for muon physics the pointing accuracy is mainly limited by the multiple Coulomb scattering due to the passage of muons in the rock overburden (its angular uncertainty is about 1°).

The streamer tubes are modularly organized: each horizontal plane is snugly covered by 48 chambers, while each vertical plane consists of 14 chambers. Enclosed in a 1.5 mm PVC envelope, each chamber is 12 m long and has a cross section of $3.2\text{ cm} \times 25\text{ cm}$. Such a chamber consists of eight individual cells in an open profile structure made of 1.5 mm thick PVC. Each cell has an active volume of $2.9\text{ cm} \times 2.7\text{ cm} \times 12\text{ m}$. The anode is a single wire made of silvered beryllium copper, having a diameter of $100\ \mu\text{m}$. It is stretched along the cell and supported by plastic inserts every meter. The cathode is the low-resistivity graphite coating ($\lesssim 1\text{ k}\Omega/\square$) on three sides of the cell. At one end of the chamber the graphite cathode is connected to a ground and the wires are connected to high voltages and readout electronics. Gas flows through both ends. The chamber is tightly sealed. In the first supermodule, there is a total of 732 streamer tube chambers, or equivalently 5856 anode wires. For horizontal streamer tube planes, the wires provide one planar coordinate of track hits and an additional planar coordinate is offered by the external pick-up strips, made of 3 cm wide and $40\ \mu\text{m}$ thick aluminum ribbons attached to a 1 mm thick PVC sheet. The strips are placed beneath the streamer chambers, making an angle of 26.5° with the wires. Both the wires and the strips are equipped with electronics for digital readout of track hits. The wires are also instrumented with electronics to process time and charge information. In addition to the conventional fast particle triggers, there is an independent trigger for slow monopoles based on the time of flight [75].

2.2.3 Track-etch Detectors

Track-etch detectors are employed to give an additional redundancy in the search for GUT monopoles besides the scintillator counters and the streamer tubes. Two types of plastic track-etch material, CR-39 and Lexan, are used in MACRO. In the first supermodule of the MACRO detector a layer of track-etch detectors is placed atop the sixth horizontal layer (counting from bottom) of streamer tubes (Fig. 2.3). This horizontal layer consists of 48 *trains* and each train is made of 47 *wagons*. Having a size of $25 \times 25 \text{ cm}^2$, each wagon is an aluminum bag filled with dry air containing three layers of CR-39 (1.4 mm thick), one layer of aluminum foil (1 mm thick) and three layers of Lexan (0.2 mm thick). Multiple layers of plastics are used to provide a spatial coincidence which eliminates background. The aluminum foil absorbs the low energy ions produced by spallations near the track-etch detector. Any wagon can be accessed by sliding the corresponding train on the rail. A vertical layer of the track-etch detectors is placed along the east and the north sides of the MACRO detector. The track-etch detector is mainly used for confirmation: Whenever an interesting candidate is found in the scintillator counters and/or the streamer tubes, a search is performed on those wagons around the expected position. Searches based on the track-etch alone are also planned: all plastic wagons will be periodically extracted and chemically processed to look for the tracks of monopoles.

2.2.4 Online Data Acquisition System

Data from the active system of the liquid scintillator counters and the streamer tubes are recorded by the online data acquisition system [69]. This system is based on a network of microcomputers (MicroVAXII running VAXELN) connected via Ethernet under DECNET protocol. A minicomputer (VAX8200³ running VAX/VMS) is used as the file server and the interface to the users. This modular system matches the modular structure of the MACRO detector and the network allows easy access from remote locations to each computer

³Now upgraded to a VAX4000/500.

to control the apparatus. Data are logged on the VAX8200 disks and then periodically copied to another computer (to reduce the load of the data acquisition computer) where the distribution tapes are made.

2.3 Liquid Scintillator Counters

The MACRO scintillator system has many features and is capable of making significant contributions to many physics topics [69]. Most relevantly, its large acceptance and specialized electronics allow a very sensitive search for supermassive particles such as GUT monopoles and nuclearites. Its general characteristics are described in this section, while the specialized monopole electronics are discussed in the next chapter.

The two horizontal faces (the *center* and *bottom* faces⁴) and three vertical faces (the *west*, *east* and *north* faces⁵) of the first supermodule are instrumented with large liquid scintillator counters. There are two types of counters, those for the horizontal faces and those for the vertical faces. Each horizontal face is covered by sixteen horizontal counters while each vertical face is made of seven vertical counters. Both types of counters are nominally 12 m long, limited by the space of the experimental hall of the Gran Sasso Laboratory and by the size of trans-Atlantic shipping containers. About 11 m of the counter is filled with a highly-transparent liquid scintillator. Two Hamamatsu R1408 8" hemispherical photomultiplier tubes (PMTs)⁶ are installed at each end of the horizontal counter, while the vertical counter has only one PMT at each end. Both the anodes and the dynodes of the PMTs are connected to give signals to the trigger and measuring electronics.

Each scintillator counter is assigned a name such as *IB01* to avoid possible confusions in referring to these counters. In this nomenclature, the first digit refers to the supermodule

⁴The term "*top face*" is reserved for the top face of the upper deck.

⁵The south face is not instrumented. See footnote 2 on page 23.

⁶The Hamamatsu PMTs in the first supermodule have been replaced with EMI D642 PMTs because of their better single photoelectron charge spectra. The EMI tubes are used for the remainder of the MACRO detector as well.

number. The first supermodule, the subject of this thesis, is located at the north end of the experimental hall. The letter stands for a scintillator layer, such as *B* for the bottom face, *E* for the east face, etc. The last two digits together indicate the counter number in each layer. The horizontal counters are numbered in an ascending order along the direction from north to south. The vertical counters are numbered from bottom to top. For example, 1C01 means the first counter from the north side in the center layer in the first supermodule, while 1N07 refers to the top counter in the north face in the lower deck of the first supermodule. If the end of a counter needs to be specified, a token of either 0 or 1 is attached to the above nomenclature: end 0 is the west or north (depending on the counter orientation) end of a counter and end 1 is the opposite end. For example, 1B03-1 means the east end of the third counter in the bottom face.

2.3.1 Counter Geometries and Optics

Both the horizontal and the vertical counters are ~ 12 m long rectangular tanks constructed from 0.63 cm PVC sheet, with cylindrical PMT housings at both ends. The counter is divided into three chambers by transparent windows made of 0.32 cm clear PVC. The central chamber (~ 11 m long) is filled with the liquid scintillator. The two end chambers house both the PMTs and light collection mirrors. The mirrors reflect light from the central chamber onto the PMT photocathode surfaces. To optimize the optical coupling between the scintillator and the photocathode, the end chambers are filled with pure mineral oil of the same type as that used for the base of the MACRO scintillator mix and to the same depth as the scintillator in the central chamber. This geometric arrangement avoids any contact between the chemically-active scintillator and the end chamber objects like the mirrors, the PMTs and their bases, thus eliminating the possibility for any potentially damaging chemical interaction to occur between them. Compared to a hypothetical situation that PMTs are directly surrounded by scintillator, this configuration of surrounding PMTs by pure mineral oil in the end chamber significantly decreases sizes of the radioactivity

pulses occurring near the PMTs, making life easier for the electronics processing PMT signals. Furthermore, the end chamber provides reasonably easy access to the PMTs for maintenance. Fig. 2.4 shows the geometric detail of the horizontal counter and Fig. 2.5 shows that of the vertical counter.

Because of the extraordinary length of the counter, light produced in the active scintillator volume propagates to the end chambers by means of total internal reflection. This is achieved by surrounding the scintillator (having a refractive index $n = 1.475$) with a liner material having an index $n' < n$. The critical angle with the liner surface is given by

$$\Theta_c = \cos^{-1} \left(\frac{n'}{n} \right) . \quad (2.1)$$

Those rays making an angle $\Theta \leq \Theta_c$ with the liner surface are totally reflected. Other rays are only partially reflected and become negligible after being reflected several times from the liner surface. The air ($n' = 1.00029$) above the scintillator makes an excellent liner, providing total internal reflection with a critical angle of 47.3° . The bottom and two side walls of the MACRO scintillator counter are lined with a white vinyl-FEP material ($n' = 1.33$). This FEP liner provides total internal reflection with a critical angle of 25.6° . The smaller critical angle of the two is more relevant — light from a distant source can reach the end chamber after several reflections only if the angle $\Theta \leq 25.6^\circ$. Although the air-scintillator interface provides total internal reflection for rays with angles $25.6^\circ < \Theta \leq 47.3^\circ$, these rays are attenuated when partially reflected from the FEP-scintillator interface. A piece of this FEP material was put in contact with the scintillator several years ago and no evidence of chemical interactions has been observed since.

Two types of artificial light sources are provided to monitor and calibrate the scintillator response and to simulate the passage of particles like GUT monopoles. Light emitting diodes (LEDs) are installed near the PMTs in the end chambers. The LEDs are capable of producing pulses of various amplitudes and widths varying over a large range, allowing simulations of the passage of particles with various velocities. Ultraviolet light from a nitrogen laser is guided by quartz optical fibers to various positions in the scintillator

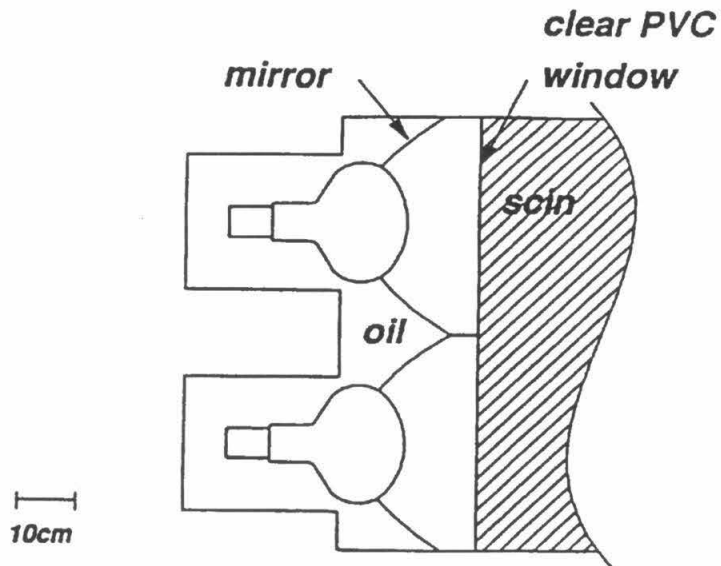


Figure 2.4: Geometry of the horizontal counter. The active liquid scintillator volume is 1120 cm long.

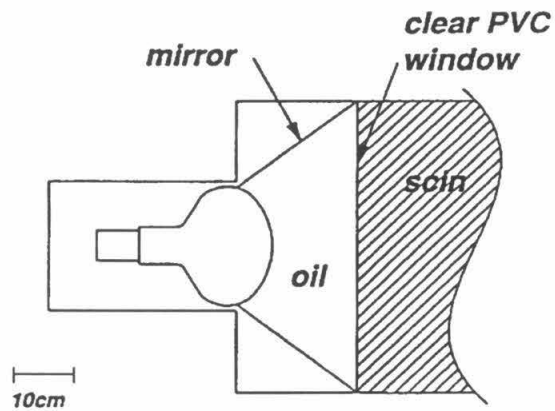


Figure 2.5: Geometry of the vertical counter. The active liquid scintillator volume is 1107 cm long.

chambers to excite the scintillator. The laser provides fast pulses of various amplitudes over a range of several orders of magnitude (controlled by optical attenuators).

Horizontal Counters

The active scintillator volume in the horizontal counter is 1120 cm long, 73.2 cm wide and nominally 19 cm deep. The depth varies by a few millimeters from counter to counter. It also differs by a few millimeters between two ends of a counter because the counter is not perfectly level. The end chamber contains two light collection mirrors, two PMTs and bases and cabling, and foam PMT mounts⁷. An LED is installed on each mirror.

Each 8" hemispherical Hamamatsu R1408 PMT has a photocathode of minimum diameter 19 cm (Fig. 2.10). The photocathodes of two such PMTs cover a minimum fraction of 41% of the transverse cross section of the active scintillator volume. Thus, they intercept less than half of the light propagated to the end chamber from the scintillator volume. A mirror is designed to increase the light collection efficiency. Made of plastic and coated with highly reflective aluminum, the mirror has a shape of a surface of revolution suitably truncated to fit into the end chamber. The shape of the revolved planar curve is calculated so that any "critical ray" coplanar with the revolution axis is reflected tangent to the hemispherical PMT envelope (the photocathode surface) (Fig. 2.6 and Fig. 2.4). A critical ray makes an angle of 23° (the critical angle⁸) with both the horizontal and vertical liner-scintillator interfaces. Therefore, this ray makes an angle of $\sin^{-1}(\sqrt{2} \sin 23^\circ) = 31^\circ$ with the mirror axis of revolution which is along the longitudinal direction of the counter. With this shape design, any rays from a distant source and coplanar with the mirror axis are guaranteed to reach the photocathode. Skew rays (non-coplanar rays) can be lost, but a ray-tracing Monte Carlo shows that the lost rays are less than 1% out of all rays including both the coplanar and the non-coplanar ones. Tests have been performed to measure the

⁷Iron magnetic shields are installed later to protect the phototubes from the ambient magnetic field.

⁸The mirror was designed for a scintillator with a refractive index 1.45, giving a critical angle of 23° rather than 25.6°.

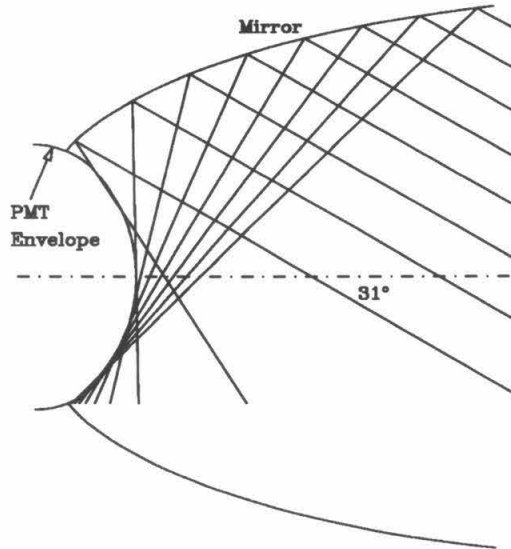


Figure 2.6: The design of the light collection mirror for the horizontal counter. All *critical rays* are reflected tangent to the PMT envelope.

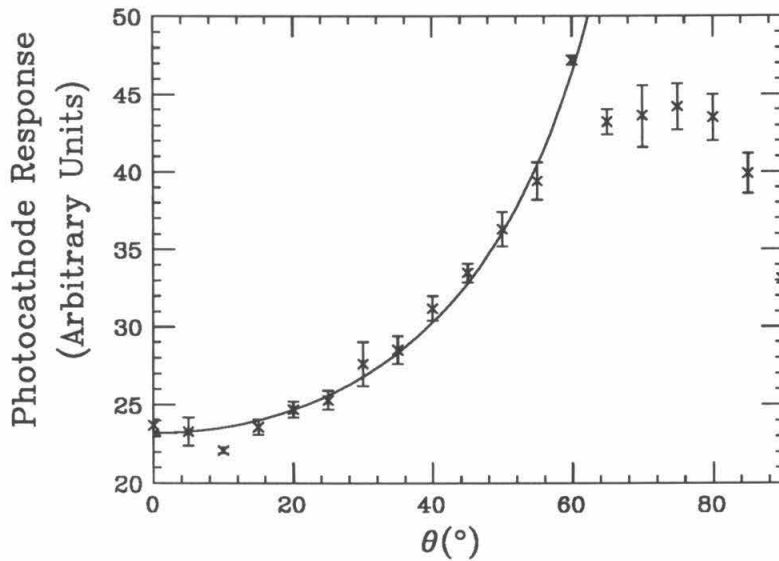


Figure 2.7: The response of the photocathode as a function of the incident angle θ with respect to the PMT envelope. The curve is a fit to the $\cos(\theta)$ function.

photocathode response as a function of the incident angle θ of the incoming light rays with respect to the surface normal. This response function follows $\sec(\theta)$ for θ up to 60° and shows a rough plateau for $\theta > 60^\circ$ (Fig. 2.7). The $\sec(\theta)$ response corresponds to the pathlength of the rays through the photocathode. Therefore, the mirror is optimized for the light produced at a distant source, since almost all of this light is reflected onto the photocathode and the photocathode has sensitivity for all incident angles.

A full-sized test counter was set up at Caltech to study the counter response under various conditions. Small plastic scintillator telescopes were placed both atop and beneath the counter at eight different locations along the counter, defining the longitudinal positions of cosmic ray muons crossing the counter with a resolution of 0.17 m (the width of the plastic scintillator). Two Hamamatsu R1408 PMTs were installed at each end of the counter as in the first supermodule of the MACRO detector at Gran Sasso. A charge-integrating ADC was used to measure the counter response in numbers of photoelectrons. The number of photoelectrons is given by

$$N = \left(\frac{\sqrt{2}\mu}{\sigma} \right)^2, \quad (2.2)$$

where μ and σ are the mean and standard deviation of the pedestal-subtracted ADC spectrum, and the factor $\sqrt{2}$ is due to the *dynode statistics* of the Hamamatsu R1408 PMTs (Appendix B). Fig. 2.8 shows the numbers of photoelectrons observed at one end of the counter as a function of positions of crossing muons for three different configurations: A) with no mineral oil and no reflecting mirrors in the end chamber; B) with mineral oil but no reflecting mirrors; C) with both mineral oil and reflecting mirrors. From these curves, one can see that the oil coupling improves the light collection by a factor of 1.78 almost uniformly along the counter except at positions close to the end chamber. One can also see that the mirrors increase the phototube response to the light from the far end of the counter by another factor of 1.65. The last factor is to be compared with what a perfect light collection would give which is a maximum increase of 2.44 (the inverse of the minimum PMT coverage of 41% in page 31); the mirrors have a minimum light collection efficiency

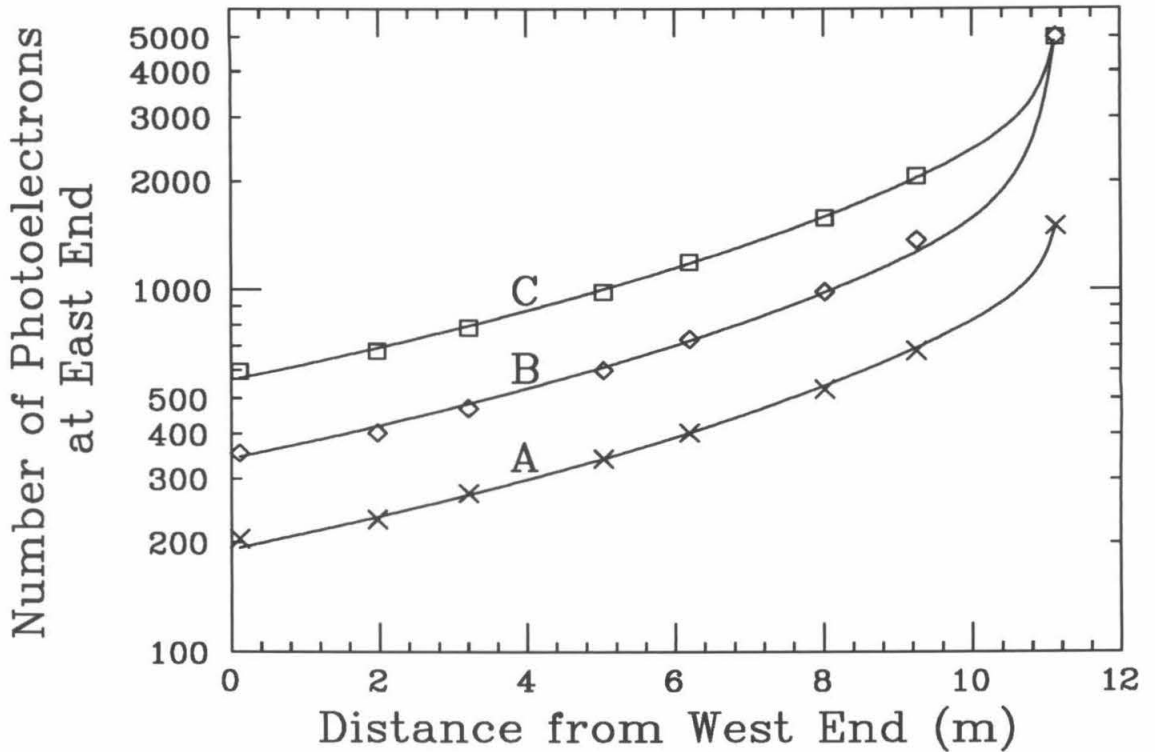


Figure 2.8: The response of the horizontal counter to muons crossing the counter at eight different positions along the counters under three different configurations: A) with no mineral oil and no reflecting mirrors in the end chamber; B) with mineral oil but no reflecting mirrors; C) with both mineral oil and reflecting mirrors. This measurement was performed using a prototype counter at Caltech, in which the liquid scintillator was known to have a worse attenuation length than the MACRO scintillator used at Gran Sasso, because the naive procedure of mixing scintillator at Caltech introduced dirt and bubbles into the scintillator.

of 68%. Meanwhile, the mirrors leave the response to the light produced near the end chambers almost unchanged, thus reducing the dynamic range of the counter response, to the benefit of the electronics.

Vertical Counters

The active scintillator volume in the vertical counters is 1107 cm long, 21.7 cm wide and 43 cm deep. As with the horizontal counters, the oil depth varies by a few millimeters from end to end and from counter to counter. A vertical counter has only one PMT and one light collection mirror in each of its two end chambers (Fig. 2.5). The PMT is of the same type with the horizontal counter. Made of highly reflective aluminum sheet, the mirror is a simple cone suitably truncated. No detailed study has been done on the performance of the vertical counters.

2.3.2 Liquid Scintillator

The unusual length of the counter (12 m) requires a highly transparent liquid scintillator, preferably having an attenuation length of 12 m or longer. To achieve this, the MACRO scintillator uses carefully-selected pure mineral oil as its base, mixed with an optimized amount of active scintillants. Measurements show that the pure mineral oil base has an attenuation length of at least 20 m at a wavelength of 425 nm. The scintillant concentrate is made of pure pseudocumene mixed with 40 grams/liter of PPO and 40 mg/liter of bis-MSB. The emission and absorption spectra of these aromatic materials can be found in reference [76]. The amounts of PPO and bis-MSB were set according to tests on a preliminary prototype counter of a size smaller than the ones actually used at Gran Sasso. The same tests also suggested that 6.2% of this concentrate should be mixed with the pure mineral oil to make the scintillator. Twenty-nine counters in the first supermodule were filled with this 6.2% scintillator.

Further investigations were performed using the same setup described on page 33 to

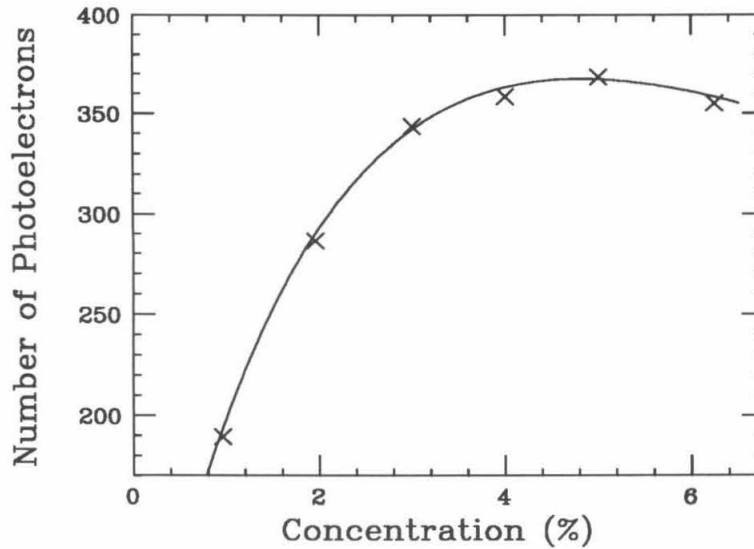


Figure 2.9: The counter response to muons crossing the counter at the far end as a function of scintillant concentration.

study the response to light from the far end of the counter as a function of the scintillant concentration. The scintillant concentration was gradually increased, and at each concentration the counter response to muons crossing the counter at the far end of the counter was measured. The results are shown in Fig. 2.9. They reveal that the response changes very little for concentrations varying from 3% to 6.2%. Thus, it was decided to use a conservative concentration 3.6%. The remaining counters in the first supermodule are filled with this 3.6% scintillator. It will be used to fill the remainder of the full MACRO detector. In summary, one liter of the final MACRO scintillator contains 0.964 liter of pure mineral oil, 0.036 liter of pseudocumene, 1.4 grams of PPO and 1.4 mg of bis-MSB. In addition, every liter of the mineral oil has 40 mg of an antioxidant added by the manufacturer. For every batch of scintillator mixed, the concentrations of the active components is checked using a spectrophotometer.

2.3.3 Photomultiplier Tubes

As mentioned before, 8" hemispherical Hamamatsu R1408 PMTs (Fig. 2.10) are used in the first supermodule of the MACRO detector. The R1408 has thirteen stages of bialkali dynodes in a venetian blind structure. In the MACRO detector both the anode and the eleventh-stage dynode are used to feed their signals to the fanouts which in turn send copies of the signals to various electronics. For the two PMTs at each end of the horizontal counter, each of the two anodes uses one 93Ω coaxial cable paralleled by a 92Ω resistor and the two such cables join into one 51Ω RG58 cable which goes to the fanout, and the two dynodes are connected in the same fashion. Thus, the PMT signals are almost properly back terminated. For the PMT in a vertical counter end, both the anode and the dynode drive back-terminated 51Ω cables. The PMTs in the first supermodule operate with a nominal gain of 5×10^6 . According to the manufacturer's specifications [77], the quantum efficiency at the wavelength of 390 nm is typically 25% and the absolute radiant sensitivity reaches its maximum at 420 nm. After folding the risetime of the phototube with the time spread of the light pulse in the MACRO scintillator counter and the stretching due to the MACRO fanout, the effective width⁹ of a single photoelectron pulse is (15 ± 2) ns. The corresponding width for a muon signal is found to be about 30 ns. The single photoelectron charge spectrum of the R1408 PMT has been measured using a LeCroy 3001 Multichannel Analyzer and it follows an exponential distribution (Fig. 2.11). From this exponential spectrum, one can derive the dynode statistics factor of $\sqrt{2}$ as described in Appendix B. Finally, Fig. 2.12 shows the PMT anode output charge as a function of the input light level in number of photoelectrons for the PMT gain of 5×10^6 . At very high light level, a pulse peak saturates but the pulse gets wider as the light level increases. Therefore, even for a light level as huge as 10^6 photoelectrons, there is still no "hard" saturation. The dynode saturation is similar but less severe.

Various electronics are employed to process the PMT signals. The specialized monopole

⁹The effective width of a pulse is defined as the integral area over the peak pulse height.

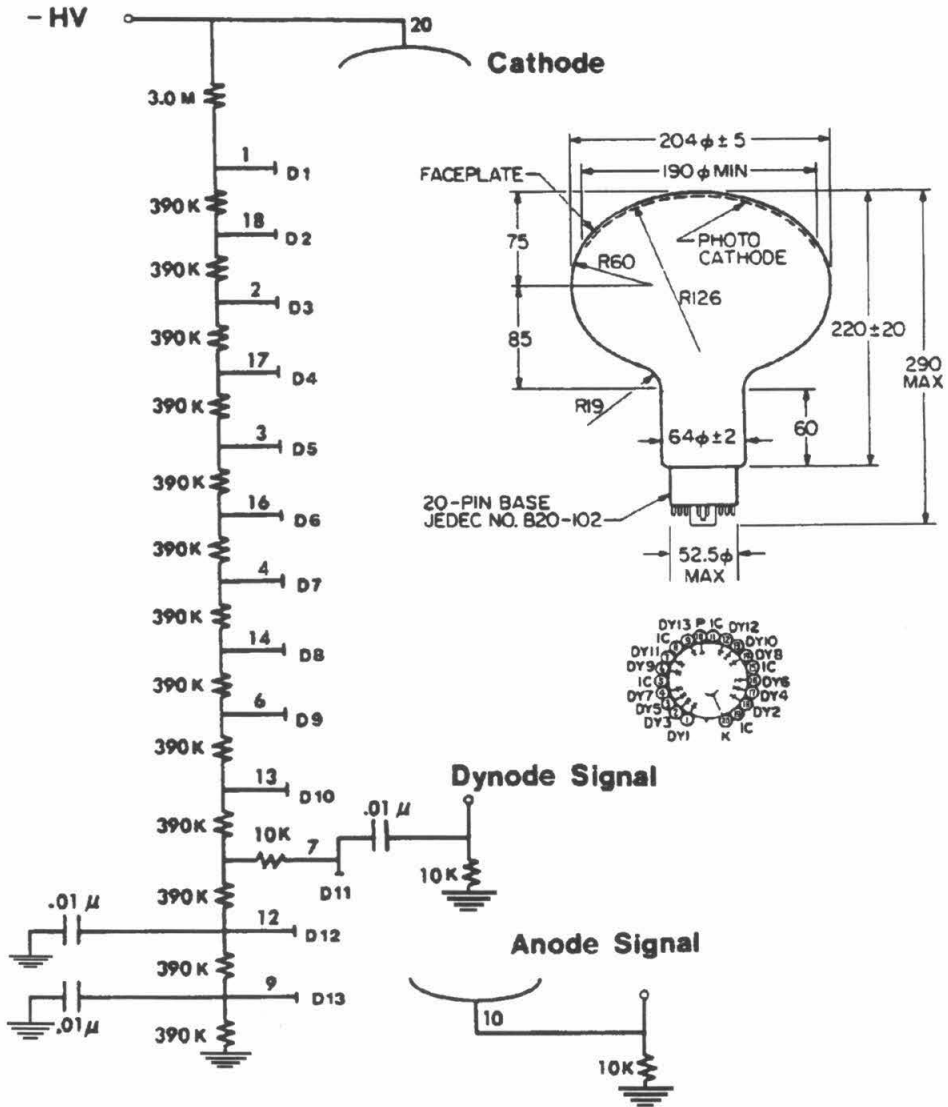


Figure 2.10: The geometry and the base of the Hamamatsu R1408 phototube.

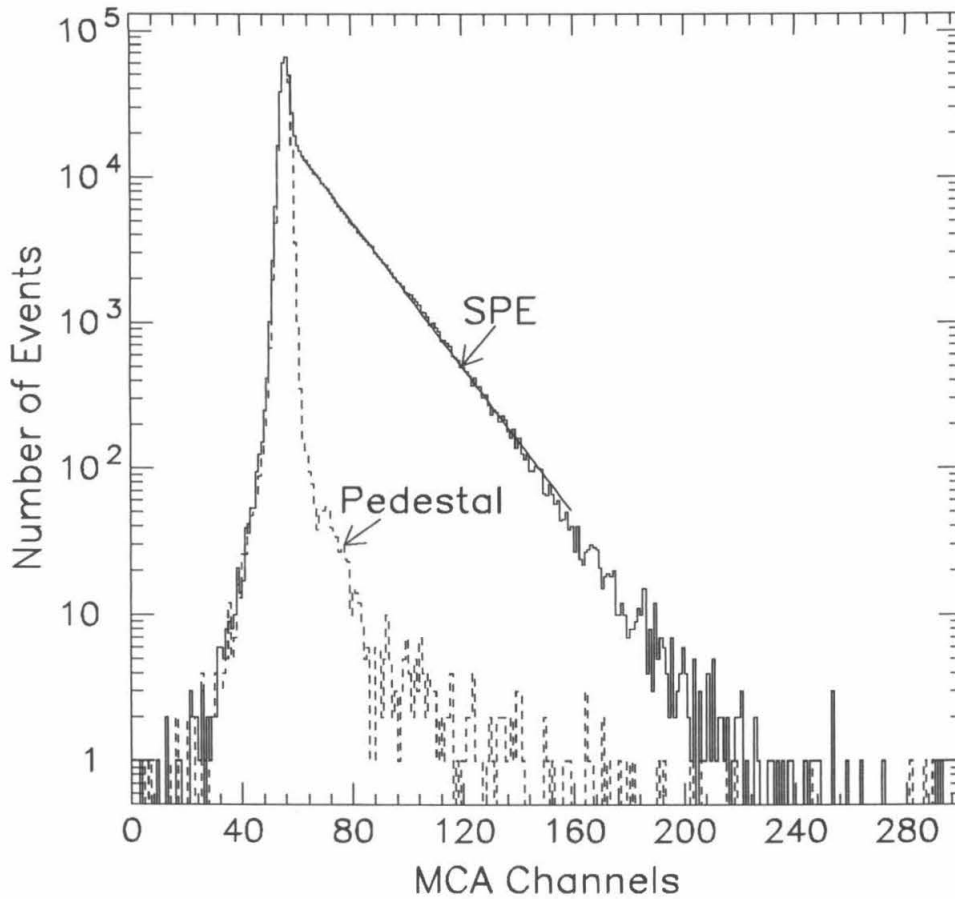


Figure 2.11: The single photoelectron (SPE) charge spectrum for Hamamatsu R1408 PMT as measured using a LeCroy 3001 Multichannel Analyzer (MCA). The solid-line histogram is the charge spectrum for single photoelectrons. An LED is used as the light source for the measurement. The solid straight line is an exponential fit to the histogram for channels from 63 to 160. The dashes are the histogram for the pedestal.

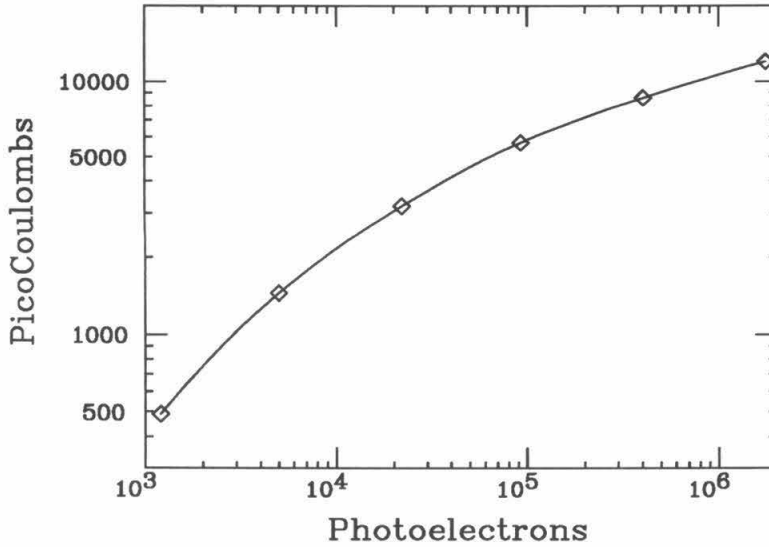


Figure 2.12: The PMT anode output charge as a function of the input light level in number of photoelectrons. The PMT gain was set at 5×10^6 . The curve is only a guide to the eye.

electronics are described in the next chapter. For the non-monopole-related electronics, see reference [69].

2.4 Conclusions

With all elements described in this chapter, the full MACRO detector will be capable of conducting a highly redundant search for GUT monopoles beyond the Parker bound. More relevant to the topic of this thesis, the liquid scintillator system in the first supermodule has many features, allowing a sensitive search for slow-moving light-yielding particles like GUT monopoles and nuclearites, if combined with the specialized monopole electronics described in next chapter.

Chapter 3

Monopole Trigger Schemes and Their Sensitivities

The primary detector elements used in this thesis for the search for GUT monopoles and other supermassive particles are the large liquid scintillator counters in the first supermodule of the MACRO detector described in section 2.3. Electronic pulses from the photomultiplier tubes (PMTs) occur from cosmic ray muons, decay products of radioactive isotopes in the environment, dark noise in the phototubes, etc. These pulses constitute backgrounds to the candidate signals from GUT monopoles. The candidate signals are selected by specialized electronic systems described below, which *trigger* the data acquisition system.

There are two types of monopole triggers¹ for the liquid scintillator detectors. The innovative main trigger, the *slow monopole trigger*, has been designed and built at the California Institute of Technology. It uses the time of passage information through each scintillator counter to identify *slow* particle candidates and is sensitive to GUT monopoles of velocities from $\sim 10^{-4}c$ to $3 \times 10^{-3}c$ (Fig. 3.1) and other supermassive particles in the

¹The terminology here is not strict: the “monopole triggers” are used as triggers for any slow-moving (thus supermassive), light-yielding particles, which include the primary goal of the MACRO experiments – GUT monopoles.

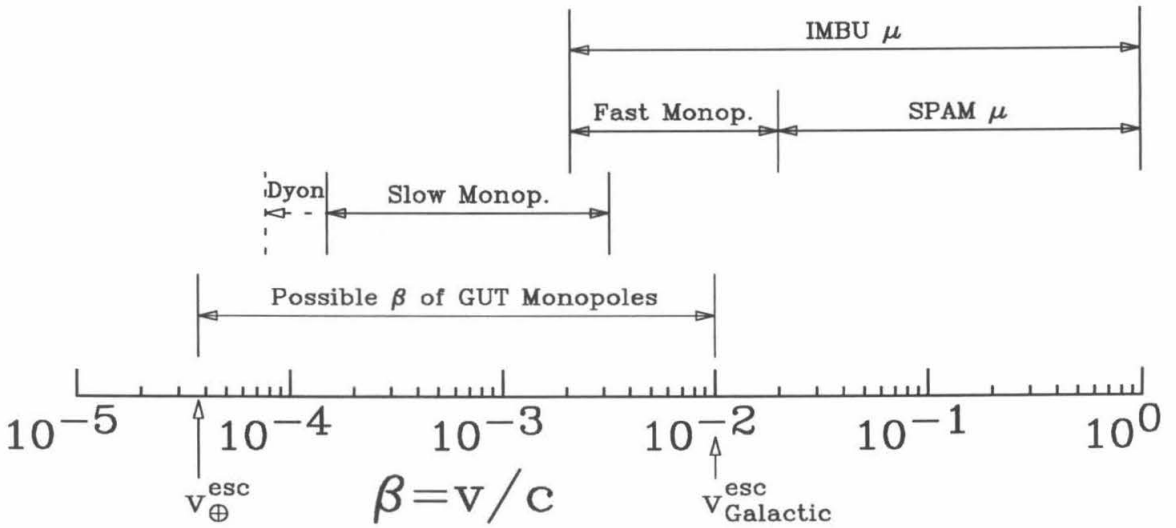


Figure 3.1: Sensitive β ranges of monopole triggers in the first supermodule of the MACRO detector. The slow monopole trigger is sensitive to GUT monopoles in the β range indicated by the solid line, and its sensitivity to dyons extends to lower velocities as indicated by the dashes. The fast monopole trigger has the same sensitive β range for both GUT monopoles and dyons. Also see Fig. 3.18 for the β ranges of these two triggers. The fast monopole trigger is in actuality the IMBU muon trigger vetoed by the SPAM muon trigger (section 3.3) so the β ranges of these two muon triggers are included for reference. Also shown is a possible β range of GUT monopoles, bounded by the earth escape velocity at the low end and by the galactic escape velocity at the high end (section 1.1.4).

similar velocity range. A more conventional second trigger, the *fast* (relatively speaking) *monopole trigger*, has been implemented to complement the first one. This second trigger is based on the time of flight information between different scintillator faces and extends the sensitive velocity range to $2 \times 10^{-2}c$. This is to be compared with the fact that the maximum possible velocity of supermassive GUT monopoles are around $10^{-2}c$, the galactic escape velocity (section 1.1.4). Other types of monopoles could have a lighter mass and thus be moving at higher velocities: Although these monopoles and other fast-moving heavily-ionizing exotic particles are searched for in MACRO by other techniques, they are not the subject of this dissertation. This chapter first introduces mechanisms for slow-moving particles to yield light in the liquid scintillator and then describes in detail the ideas and the circuitry of these two monopole triggers and their sensitivities, with emphasis on the slow monopole trigger.

3.1 Light Yield of Slow-moving Particles

In passing through scintillator, both monopoles and nuclearites lose energy and yield scintillation light, but via different mechanisms. In this section, I shall first discuss the conventional scintillation yield of slow-moving charged particles including slow monopoles, and then describe the light yield from the black body radiation of the shock waves associated with the traversing nuclearites.

3.1.1 Scintillation of Slow-moving Charged Particles

Electrically or magnetically charged particles lose energy by excitation and ionization of molecular electrons which are converted to light in scintillator. The energy loss rate, also called stopping power, of fast-moving ($\beta \gtrsim 0.1$) electrically charged particles in matter follows the well-known Bethe-Bloch formulae, which can be applied to fast monopoles with modifications [78]; a monopole carrying magnetic charge g at a velocity v loses

roughly the same amount of energy as a particle carrying an equivalent amount of electric charge gv/c moving at the same velocity, because these two particles induce electric fields of the same magnitude. No satisfactory theory to date covers the stopping power of protons for $0.01 < \beta < 0.05$ [32], though scintillation yield has been measured for protons in this β range [79].

For $10^{-3} < \beta < 10^{-2}$, Lindhard [80,81], and Fermi and Teller [82], have developed an accurate model of the electronic stopping power of electrically charged particles characterized by a linear dependence on the projectile velocity. Ahlen and Kinoshita [32] have extended these calculations to magnetic monopoles and found that the electronic stopping power of a monopole carrying the Dirac charge $g = g_D = 137e/2$ at any given velocity is roughly 1/4 of that of a proton at the same velocity. Figuratively speaking, this can be understood if we replace the aforementioned equivalent electric charge gv/c of a monopole by gv_F/c , where $v_F \approx c/137$ is the Fermi velocity. In the Lindhard and Fermi-Teller model, the medium is assumed to behave like a degenerate Fermi gas, in which the Fermi velocity is the only characteristic velocity.

Naively one may wish to extrapolate the linear velocity dependence in the Lindhard model to lower velocity region $\beta < 10^{-3}$. However, simple two-body kinematics suggests that the energy transfer from the ionizing particle to an atomic electron is forbidden if the minimum excitation energy of the system, E_g , exceeds the maximum possible energy transfer to the electron, given by $E_{\max} = 2m_e v(v + v_e)$, where $v = \beta c$ is the velocity of the heavy projectile, and m_e and v_e are the electron mass and velocity, respectively. This fact modifies the Lindhard linear dependence, but no satisfactory theory to date predicts this modification quantitatively.

Ahlen and Tarlé [83] have proposed a band-gap correction to the linear velocity dependence for the stopping power in organic scintillator, which uses results of Brandt and Reinheimer [84] dealing with the interactions of charged particles with semiconductor. These results are obtained using a semiconductor model with an effective Fermi energy

E_F , and consequently a maximum electron velocity v_F . Use of this model inevitably leads to a sharp kinematic cutoff in the electronic stopping power, and consequently a cutoff in scintillation yield as well. Simple kinematics gives this velocity cutoff as $v = E_g/(2m_e v_F)$. For NE-110 scintillator, it is estimated that $E_g = 5.0 \text{ eV}$ and $v_F = c/145$, and thus the cutoff is predicted as $v \sim 7 \times 10^{-4} c$ [83]. However, several years later, Ficenech *et al.*, including Ahlen and Tarlé, observed scintillation light from neutron-induced recoil protons with velocities as low as $2.5 \times 10^{-4} c$ [85, 40], contradicting the sharp cutoff prediction which has also been criticized by Groom *et al.* [86].

Surface effect in scintillator makes it difficult to measure scintillation response at very low energies through direct use of charged-particle beams. The low β scintillation measurements [85, 40, 87] use recoil protons produced within a scintillator by elastic collisions with neutrons. Ficenech *et al.* [85, 40] employed quasi-monoenergetic beams of 2- and 24-keV neutrons. NE-110 plastic scintillator was used. The proton recoil energy E_p is related to the scattering angle θ and the neutron energy E_n , according to $E_p = E_n \sin^2 \theta$. The scintillation light was measured using photomultipliers. The best fit to the measured data of the scintillation yield is obtained if Lindhard's linear stopping power is modified with an adiabatic correction factor of the form [85, 40]

$$F_{AC}(\beta) = 1 - \exp(-\beta^2/\beta_0^2), \quad \text{where } \beta_0 = 7 \times 10^{-4}. \quad (3.1)$$

This factor indicates the reduced efficiency for electronic excitations at low velocities. The absence of a sharp threshold in F_{AC} is most likely due to high velocity tails (unlike semiconductor) in the electron momentum distributions, which would allow an energy transfer above gap for lower velocity projectile; this also explains that F_{AC} starts to fall off around the kinematic cutoff $\beta \sim 7 \times 10^{-4}$. A less likely conjecture is that the perturbation of the atomic levels by the slow-moving projectiles may allow level mixing to occur, analogous to the Drell mechanism [42]; however, in this scenario, it seems unlikely that F_{AC} would exhibit an exponential decrease around the kinematic threshold, since the energy loss for helium due to the Drell mechanism is linear in the velocity region

$$\beta = (2.0-10.0) \times 10^{-4}.$$

This result of low β scintillation is used to predict the scintillation yield of supermassive charged particles, which is shown in Fig. 3.2 [85,40]. The upper bound on the scintillation yield for a bare monopole is taken to be the light yield from the linear electronic stopping power modified by F_{AC} . However, although the sharp cutoff in the scintillation response is not observed for protons, it is not ruled out for monopoles at this time. In the aforementioned less likely scenario that the absence of a cutoff in proton F_{AC} is due to level mixing, it is possible that the smaller interaction strength between a monopole and an electron (compared to that of a proton and an electron) prevents the level mixing effects. Thus, the Ahlen-Tarlé model is taken as an overconservative lower bound on the light yield of bare monopoles. The yield for a dyon, which has the same properties with respect to energy loss as a monopole-proton composite, is more certain since $\sim 4/5$ of the light yield is due to electric charge, and F_{AC} stopping is used. For supermassive $\frac{1}{3}e$ electrically charged superstring particles, the light yield has the same uncertainty as for bare monopoles because of the small charge. Thus, same as the case for bare monopoles, the upper bound on light yield uses F_{AC} stopping power and an overconservative lower bound adopts the Ahlen-Tarlé model.

3.1.2 Black Body Radiation of Nuclearites

Unlike the charged particles, nuclearites give scintillation light through a different mechanism. As described in section 1.2.1, nuclearites consist of roughly equal number of up, down and strange quarks. However, since the strange quarks are much heavier than others and so disfavored, the net electric charge is positive and is compensated by electrons [59]. Nuclearites behave like superheavy nuclear atoms, with A and Z well beyond any elements in the periodic table. As a nuclearite traverses a medium, the tightly-bound electron cloud displaces all matter in its path by elastic or quasi-elastic collisions with the ambient atoms,

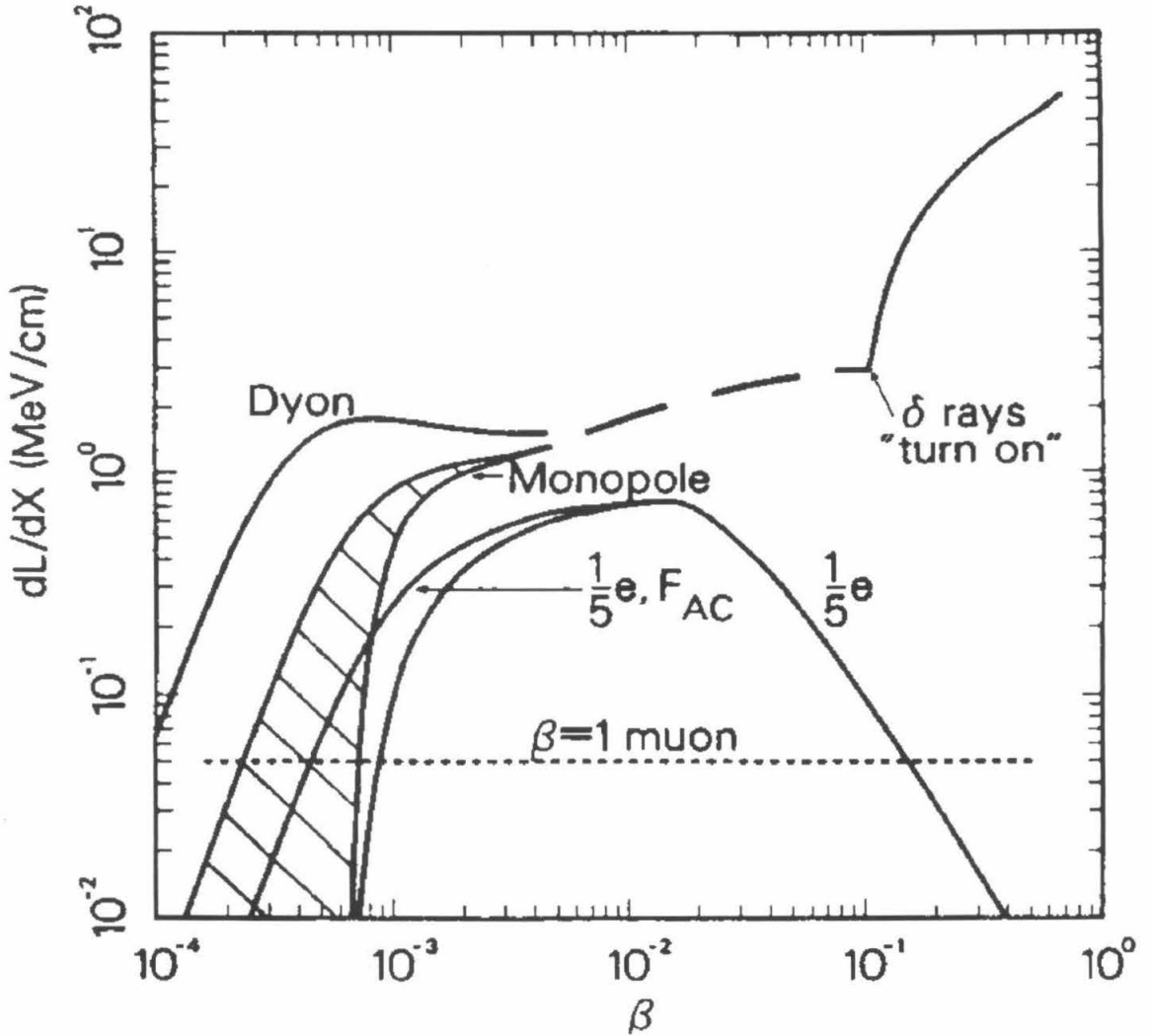


Figure 3.2: Predicted scintillation light yield for bare monopoles, dyons and $\frac{1}{5}e$ superstring particles. The shaded regions are allowed. The abrupt increase for monopoles with $\beta > 0.1$ is due to production of delta rays whose scintillation emission is not quenched. Reprinted from reference [85].

and thus loses its energy at a rate [59]

$$\frac{dE}{dx} = -A\rho v^2, \quad (3.2)$$

where ρ is the density of the medium, v is the nuclearite velocity, and A is its effective cross-sectional area which is taken to be [59]

$$A = \begin{cases} \pi(3M/4\pi\rho_N)^{2/3}, & \text{for } M \geq 1.5 \text{ ng} \\ \pi \times 10^{-16} \text{ cm}^2, & \text{for } M < 1.5 \text{ ng} \end{cases} \quad (3.3)$$

where $\rho_N = 3.6 \times 10^{14} \text{ g cm}^{-3}$ is the estimated nuclearite density and M is its mass. The lighter nuclearites are never smaller than $\sim 1 \text{ \AA}$. Eq. 3.2 breaks down for subsonic velocities. One can compute the range of a nuclearite as a function of its mass [59]

$$\int_0^L \rho dx = \begin{cases} 3 \times 10^7 (M/1 \text{ ng})^{1/3} \text{ g cm}^{-2}, & \text{for } M \geq 1.5 \text{ ng} \\ 2.3 \times 10^7 (M/1 \text{ ng})^{1/3} \text{ g cm}^{-2}, & \text{for } M < 1.5 \text{ ng} \end{cases} \quad (3.4)$$

Thus, nuclearites heavier than 10^{-10} g penetrate the rock overburden and reach the MACRO detector in any downward-going directions, and those heavier than 0.1 g pass freely through an earth diameter and reach MACRO with an isotropic flux.

As a nuclearite passes through a transparent medium, a fraction of its energy loss is converted into light. The lower bound on the light yield have been deduced from thermodynamic arguments in which light is emitted as black body radiation from an expanding cylindrical thermal shock wave by De Rújula and Glashow [59] (in natural units $\hbar = c = 1$)

$$\frac{dL}{dx} = \frac{1}{6\pi^2\sqrt{2}} A \omega_{\max}^{5/2} (m/n)^{3/2} v^2, \quad (3.5)$$

where m is the molecular mass of the medium, n is the relevant number of submolecular species in a molecule, and ω_{\max} is the maximum frequency for which the medium is transparent. This formulae assumes that only the black body radiation in the transparent region is collected.

In the scintillator, however, although it is not transparent in the ultraviolet region, the black body radiation emitted there is still collected through the wavelength shifts (which

absorb UV light and reemit it in the visible region). For this reason, $\omega_{\max}^{5/2}$ in Eq. 3.5 should be replaced by [63]

$$(\omega_{\max}^0)^{5/2} + \sum_{i=1}^N (\bar{\omega}^{eN} / \bar{\omega}^{ai}) Q_i Q_{i+1} \cdots Q_N [(\omega_{\max}^{ai})^{5/2} - (\omega_{\min}^{ai})^{5/2}], \quad (3.6)$$

where ω_{\max}^0 is the maximum frequency for which the scintillator is transparent, N is number of wave shifter components, ω_{\max}^{ai} and ω_{\min}^{ai} are respectively the maximum and the minimum absorption frequency of the i th shifter, Q_i is its quantum efficiency, $\bar{\omega}^{ai}$ is its average absorption frequency, and $\bar{\omega}^{eN}$ is the average emission frequency of the last waveshifter (which emits in the transparent region). For the MACRO scintillator (section 2.3.2), expression 3.6 gives $(4.35 \text{ eV})^{5/2}$, which is about twice as large as $(\pi \text{ eV})^{5/2}$, the typical value for a transparent material.

Using Eq. 3.5 and replacing $\omega_{\max}^{5/2}$ by expression 3.6, we have calculated the light yield per unit pathlength expected in the MACRO scintillator for nuclearites of different masses. The results are shown in Fig. 3.19.

3.2 Slow Monopole Trigger

3.2.1 Motivations

Although it is generally expected that GUT monopoles and other supermassive particles are most likely to travel at the galactic velocities $10^{-3}c$, they could very well traverse the earth with any velocities in the range from $10^{-2}c$ (for extra-galactic monopoles) down to the earth escape velocity $3.7 \times 10^{-5}c$ (Fig. 3.1) (section 1.1.4). Such a wide velocity range also means a wide ionization range, as discussed in section 3.1. Even at a given velocity, the amount of light produced by different types of supermassive particles differs greatly. Thus, developing triggering electronics for them presents a very special challenge. The usual particle detection often requires the fast coincidence to generate the trigger. This *coincidence technique* may be used to detect $\beta = 10^{-2}$ monopoles (section 3.3), but it

cannot be used to search for monopoles of velocities lower than $10^{-3}c$. While the time of flight for a relativistic particle to traverse the detector vertically is about 15 ns, this time is about $15 \mu\text{s}$ for a $\beta = 10^{-3}$ particle (Fig. 3.3), and $150 \mu\text{s}$ for a $\beta = 10^{-4}$ particle. If one attempts to setup a trigger scheme with such a wide coincidence gate and with a low pulse height discrimination level as demanded by the low light yield of slow monopoles, the trigger rate induced by the radioactivity backgrounds will be enormous, since the radioactivity-induced singles rate at one end of a typical MACRO scintillator counter is about 30 kHz.

However, the time of passage of a slow particle through the 19 cm thick scintillator body of each layer of the MACRO detector gives us a powerful handle. In crossing a scintillator layer, a particle with galactic velocity $10^{-3}c$ produces a signal of about $0.6 \mu\text{s}$ duration (Fig. 3.3). This signal can easily be distinguished from that of a relativistic particle, since a relativistic particle crosses in 0.6 ns, giving a short signal whose width is determined by the PMT inherent width of ~ 30 ns. Although this feature is very clear, the task of using it to generate triggers is not trivial, due to the extremely wide ranges of the possible velocities and ionization of various supermassive particles.

At the high β end, this trigger should cover velocities as high as $10^{-2}c$, velocities of monopoles of extra-galactic origin. Fortunately in the first supermodule, a conventional time of flight trigger (the fast monopole trigger in section 3.3) covers the β range from 2×10^{-3} to 1.5×10^{-2} (Fig. 3.1). To ensure that there is no gap in the velocity range of the MACRO monopole sensitivity, the slow monopole trigger should be sensitive to monopoles as fast as $\beta = 2 \times 10^{-3}$ or faster. Monopoles with such velocities produce large pulses having widths of ~ 300 ns. For the low velocity region, ideally this slow monopole trigger should be sensitive to monopoles having velocities as low as the earth escape velocity $3.7 \times 10^{-5}c$. The light yield in the scintillator from monopoles and other supermassive particles having such extremely low velocities are discussed in section 3.1. Because of their long transit time and low light yield, the signals from these slow-moving

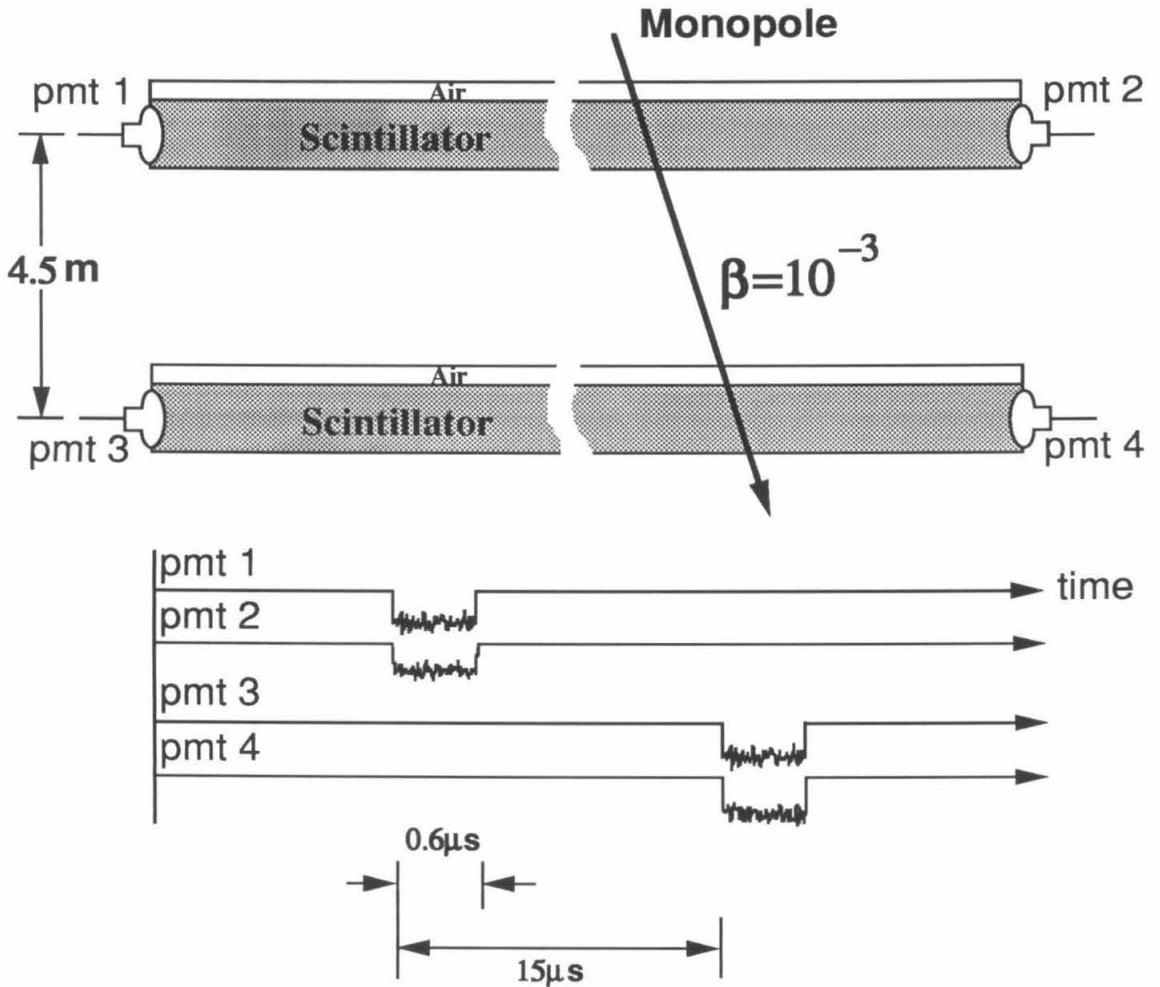


Figure 3.3: The passage of a $\beta = 10^{-3}$ particle through the center and the bottom scintillator layers of the MACRO detector (see section 2.3 for the detector geometry). The pulse trains in this picture are only artist's sketches.

particles are long trains of single photoelectron (SPE) pulses. For example, a $\beta = 10^{-4}$ GUT monopole crossing the center of a horizontal counter would produce a pulse train having a duration of $6.3 \mu\text{s}$ and containing ~ 100 separated photoelectrons. Shown in Fig. 3.4 are pulse trains generated by the Monte Carlo described in Appendix C for GUT monopoles passing through the center of the MACRO scintillator counter at four different velocities, using the expected ionization given in section 3.1. It is a very difficult problem for one trigger circuit to select all these qualitatively different pulse shapes.

3.2.2 Circuits

A specialized trigger circuit [88] has been developed to detect signals of slow particles passing through the MACRO liquid scintillator counters. It uses a strategy that triggers on both large wide pulses and long trains of separated single photoelectron pulses characteristic of light-yielding slow-moving particles, while rejecting most short pulses from muons and radioactivities. The circuit consists of two parts — the analog front-end Time Over Half Maximum discriminator (TOHM) and the digital Leaky Integrator. Thus, it makes up the *slow monopole trigger (SMT)*.

To select a slow-moving candidate from the backgrounds of large short pulses due to muons and radioactivities, the scheme uses the time of passage of a particle through the active scintillator volume, *i.e.*, it uses the width of a pulse or the sum of widths of all pulses in a train. The full width at half maximum (FWHM) of each input pulse is generated by the TOHM circuit and then sent to the Leaky Integrator to determine whether the triggering requirement is satisfied. Whenever its input from the PMT signal exceeds a pre-set minimum threshold, the TOHM discriminator dynamically raises its discrimination level to roughly half of the input pulse amplitude and produces a TTL logical output pulse whose width is approximately equal to the FWHM of the input pulse (Fig. 3.5). The pre-set minimum threshold decides whether the TOHM produces any output at all and the dynamic discrimination level determines the output width. In the case that the PMT signal

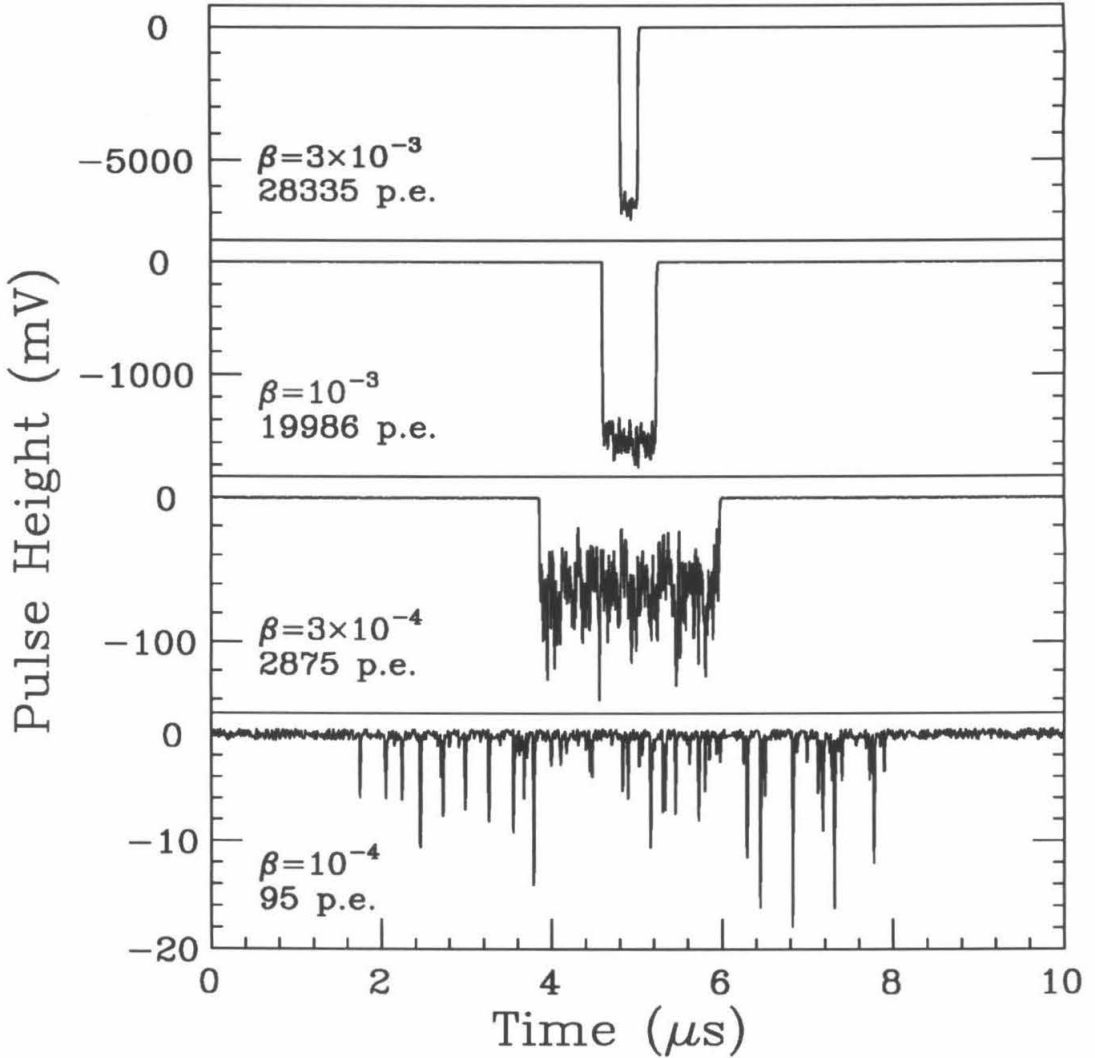


Figure 3.4: Monte Carlo simulated pulse trains using the techniques described in Appendix C. For GUT monopoles at different velocities, the light yield is assumed to follow the optimistic curve in Fig. 3.2. The charge of a single photoelectron (the integral of the SPE pulse shape over time) follows an exponential distribution with a mean of $50 \text{ mV} \cdot \text{ns}/\text{pe}$, corresponding to a PMT gain of 6.25×10^6 (see page 153). For the big pulse at the high β end, the PMT saturation is ignored. Fluctuations of 1 mV peak to peak amplitude are added to the baseline.

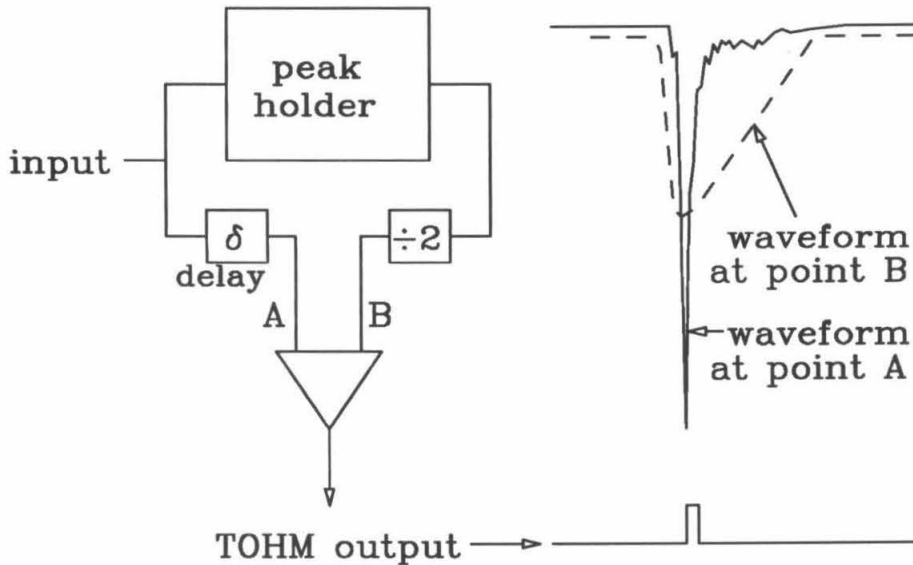


Figure 3.5: The TOHM circuits. Shaped by the peak holder, the waveform at point B decays linearly from the half maximum to the baseline, effectively eliminating the afterpulses following a large signal.

from a slow particle is a pulse train, it is shaped by the TOHM into a train of TTL pulses with variable widths. This dynamic discrimination level at the half maximum has the advantage that it can suppress the long afterpulses typically following the large fast signals from muons and radioactivities (Fig. 3.5). This is to be compared with a conventional fixed-level discriminator giving the output width as the time at which the input pulse height is over this fixed level; this level would have to be set below the SPE pulse height to select the SPE pulse train from a very slow monopole, so this discriminator would generate logical output pulses prolonged by those afterpulses; these prolonged logical pulses would most likely be mistreated by the subsequent Leaky Integrator as those from the wide pulses of slow monopoles. For all fast processes like muons and radioactivities, many photoelectrons are on top of each other since they are produced at about the same time, so the signals are large but short pulses. They are greatly suppressed by the TOHM circuit since its output disregards the pulse height and only counts for the time over half

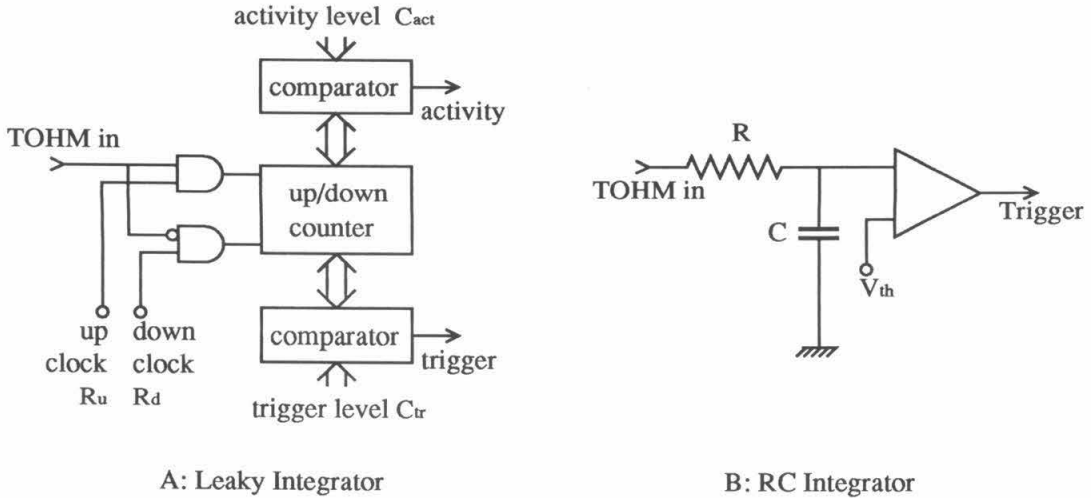


Figure 3.6: The Leaky Integrator and an ordinary RC integrator.

maximum. For slow particles like GUT monopoles, the photoelectrons are spread out over a relatively long period of time; thus the signals are either wide large pulses or long SPE pulse trains. Their TOHM outputs are either wide logical pulses or long trains of TTL pulses each having the width of a SPE pulse; they are effectively amplified by the TOHM circuit. For example, a muon pulse of 1200 photoelectrons produces a TOHM output of a width of ~ 30 ns, wider than a SPE pulse (about 15 ns wide) but not importantly so; a $\beta = 10^{-4}$ GUT monopole signal is a $6.3 \mu s$ long train containing 100 photoelectrons and its TOHM output is a train consisting of about 100 TTL pulses each having a width of about 15 ns if the TOHM pre-set minimum threshold is indeed set below the average SPE pulse height (so most SPEs give TOHM outputs). Depending on the Leaky Integrator parameters, the latter train may be selected while the former would be rejected.

The TTL output from the TOHM is then passed on to the Leaky Integrator (Fig. 3.6.A), which then decides if the width of a pulse or the sum of widths of all pulses in a pulse train indicates the passage of a slow particle. The Leaky Integrator uses an 8-bit up/down counter

which counts up at a rate R_u when the input is high and counts down at a programmable slower rate R_d when the input is low. The *up-counting clock rate* is chosen as 66.00 MHz; its period of 15.15 ns is about the same as the SPE pulse width. Although the SPE width is about 15 ns, if the exponentially distributed SPE pulse height happens to be only slightly over the TOHM threshold, the TOHM output width is then shorter than 15 ns. To count the SPEs as efficiently as possible, there is logic to ensure that any pulse with a width from 5 ns to 30 ns counts up exactly one count. The *down-counting clock rate* is carefully chosen to leak away the background counts while not missing the signals of very slow monopoles. The singles counting rate from one horizontal scintillator counter end is ~ 30 kHz; it is ~ 120 kHz for the 4:1 multiplexed counter ends in the first supermodule (*cf.* Table 3.1 on page 68). The down-counting rate should be significantly greater than this background radioactivity rate in order to leak away the counts due to these background radioactivities. On the other hand, to efficiently accumulate the counts from a long pulse train of separated SPEs characteristic of very slow monopole signals, the down-counting rate should be significantly less than the SPE rate in the signal train (number of SPEs divided by the train duration). In summary, a faster down-counting clock suppresses the backgrounds more effectively, while a slower down-counting clock selects slow monopole signals more efficiently. In actuality, this clock is carefully optimized and its value will be described on page 75. When the content of the counter is zero, the down-counting is inhibited. Thus, the up-counting due to a signal does not ever start from a negative count. A *trigger* occurs whenever the content of the counter, representing the input width, reaches the programmable threshold count C_{tr} (the trigger level). There is another similar but lower threshold, *i.e.*, the activity level C_{act} . When reached, it produces a low level trigger — the *activity*. Indicating the beginning of a long pulse train, the activity is used to determine when to freeze the waveform digitizer (*cf.* page 64). The up-counting and down-counting processes are quite similar to the charging and leaking processes of an ordinary RC integrator (Fig. 3.6.B), from which the name “Leaky Integrator” is derived.

The Leaky Integrator circuit uses standard TTL digital logic.

At the high β end, the PMT signal from a GUT monopole is a large wide pulse and the TOHM output is a relatively wide logical pulse. The Leaky Integrator trigger level acts like a “width discriminator” having the width threshold

$$W_{\text{th}} = \frac{C_{\text{tr}}}{R_{\text{u}}} \quad . \quad (3.7)$$

This width discrimination imposes a sharp cutoff at the high end of the β range in which the slow monopole trigger is sensitive,

$$\beta_{\text{max}} = \frac{L}{cW_{\text{th}}} = \frac{LR_{\text{u}}}{cC_{\text{tr}}} \quad , \quad (3.8)$$

where $L \approx 19$ cm is the monopole pathlength through the scintillator body and c is the speed of light. At the very low β region, a GUT monopole produces a train of SPEs which the TOHM shapes into a train of TTL pulses. For simplicity, we may ignore statistics and assume that every photoelectron pulse has the same width w , that there is no overlapping of photoelectrons, and that the counter rarely counts down to zero during the duration of the pulse train (the down-counting is inhibited when the counter has a vanishing count), then the Leaky Integrator trigger requirement is

$$NwR_{\text{u}} - (T - Nw)R_{\text{d}} \geq C_{\text{tr}} \quad , \quad (3.9)$$

where T is the duration of the pulse train and N is the number of photoelectrons in the train. If we define the effective width of the pulse train as

$$W^{\text{eff}} = Nw - (T - Nw)\frac{R_{\text{d}}}{R_{\text{u}}} \quad , \quad (3.10)$$

the Leaky Integrator is an “effective width discriminator” having the same threshold as in the high β case,

$$W_{\text{th}}^{\text{eff}} = \frac{C_{\text{tr}}}{R_{\text{u}}} \quad . \quad (3.11)$$

A slow down-counting clock increases the effective width of the pulse train, hence it reduces the light yield required to fire the slow monopole trigger at a given trigger level

and a given velocity (*i.e.*, a given pulse train duration). This apparent sharp threshold of the effective width is obtained under many assumptions; in actuality, it is not as sharp as suggested here because these assumptions are not exactly accurate, *e.g.*, the time interval between SPEs fluctuates. The above reasoning can be applied to the activity level in the same fashion.

3.2.3 Trigger Efficiency Studies

This subsection describes empirical tests and Monte Carlo simulations conducted in order to understand the slow monopole trigger efficiency as a function of its parameters and input light levels. Calibrations of the sensitivity of this trigger in the first supermodule are described in section 3.5.

In the empirical tests done at Caltech, an LED was used to generate light for the PMT with various light levels and various pulse durations, simulating the passage of ionizing particles through scintillator counters at various velocities. Both the LED and the PMT were in a light-tight dark box. The PMT signals were sent to a TOHM circuit. The TOHM minimum threshold was set at 10 mV, one fifth of the mean single photoelectron pulse height. Since the SPE pulse height of the Hamamatsu PMT follows the exponential distribution², the TOHM produced a TTL output pulse for $\sim 82\%$ of input SPE pulses. The light level of the input pulse or pulse train, expressed in number of photoelectrons in the pulse or pulse train, was measured by a charge-integrating ADC for a short pulse of high light level; and for a long pulse train of low light level, the number of photoelectrons in the train was approximately equal to the number of TOHM output pulses in the train, which was counted with a scaler. Thus, by varying the input light level and duration and adjusting the Leaky Integrator parameters, we obtained a mapping of the slow monopole trigger efficiency as a function of the trigger level C_{tr} , the down-counting period $D = 1/R_d$,

²To be precise, it is empirically found that the SPE charge follows an exponential distribution (Fig. 2.11). Since the SPE width fluctuation is negligible (the integral over peak is (15 ± 2) ns), the SPE pulse height also follows an exponential distribution.

the LED pulse train duration and the light level. Fig. 3.7 shows the trigger efficiency as a function of β at four different light levels, three different decay constants and a fixed trigger level $C_{tr} = 10$. The β was obtained from the pulse train duration assuming 19 cm pathlength. Besides the LED tests, Monte Carlo simulations were also performed on the circuit under the same conditions, following the procedures detailed in Appendix C. The resulting mapping of the trigger efficiency is shown in Fig. 3.8. It is similar to the one obtained from the empirical tests using the LED (Fig. 3.7). The Monte Carlo mapping also shows extra curves at a very high light level of 600 photoelectrons, which are absent in the empirical tests.

According to Eq. 3.8 on page 57, the trigger level $C_{tr} = 10$ imposes a high β cutoff of the trigger efficiency at $\beta_{max} = 4.2 \times 10^{-3}$. The cutoff, independent of light levels and down-counting periods, is very sharp at high light levels as shown by those curves having a light level of 600 photoelectrons in Fig. 3.8. This is because the SMT circuit is a sharp “width discriminator” only if the input is a large pulse (high light level) instead of a pulse train (low light level). Nevertheless, at low light levels, the β_{max} still gives the upper limit of the possible β range although the cutoff is not as sharp.

In the low β region, the trigger efficiency increases as the down counting clock decreases, as expected from Eq. 3.9. To demonstrate this characteristic using these curves, let us suppose, as an example, that a certain particle traverses the MACRO detector at a velocity of $5 \times 10^{-5}c$ and deposits 40 photoelectrons in a scintillator counter. As shown in both the empirical and the Monte Carlo curves, the slow monopole trigger would definitely miss the signal (0% efficiency) if the down counting clock period were set to be $D = 180$ ns, and would definitely pick up the particle with 100% efficiency if $D = 4$ μ s; and if $D = 600$ ns, the trigger efficiency would be between 70% and 95%.

In summary the empirical tests and the Monte Carlo simulations agree with each other. Both of them show that the trigger circuits indeed work as expected.

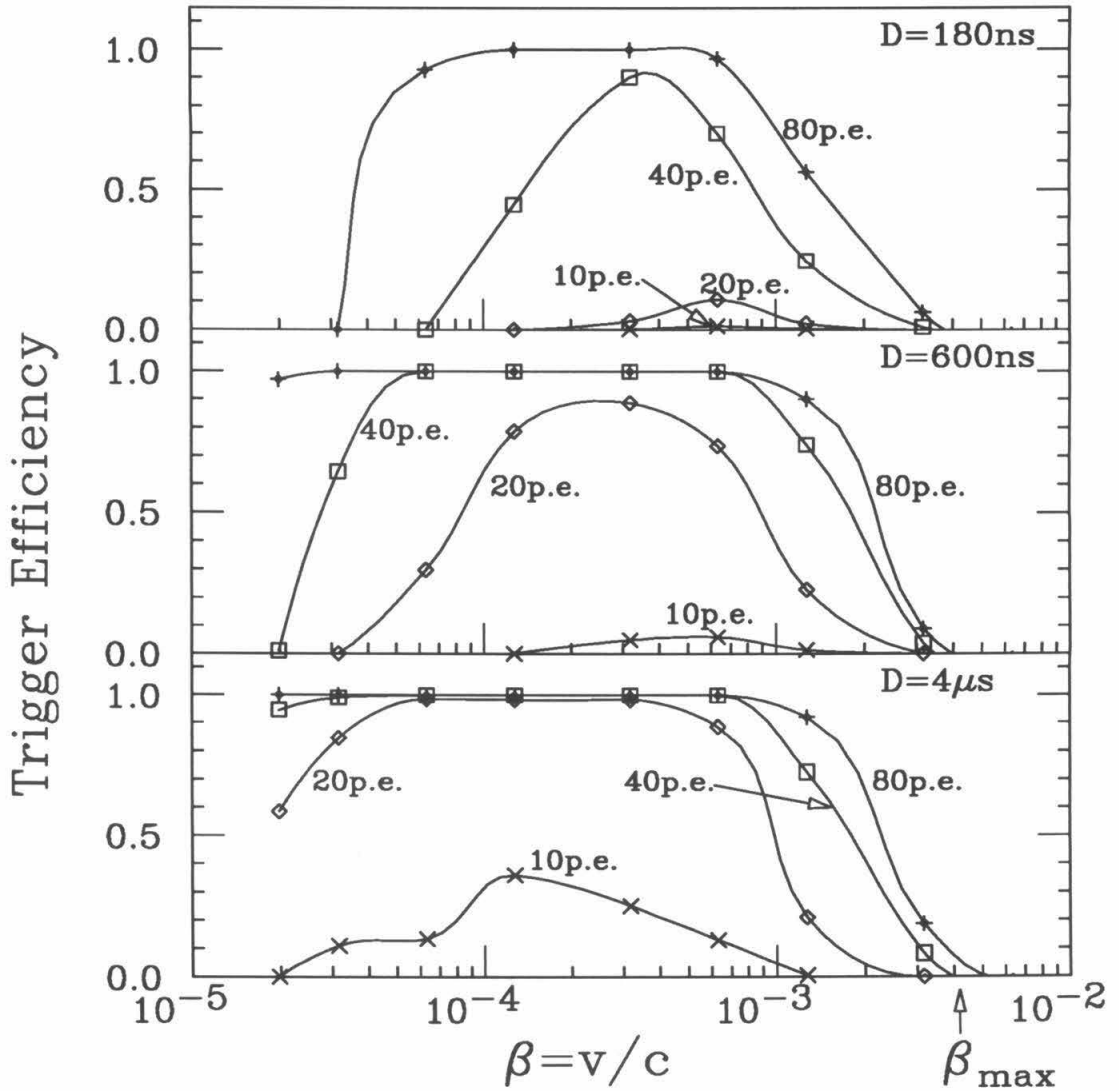


Figure 3.7: LED simulation of the slow monopole trigger efficiency. The trigger level is fixed at $C_{\text{tr}} = 10$, and thus the high β cutoff is $\beta_{\max} = 4.2 \times 10^{-3}$, according to Eq. 3.8. The curves are just guides to the eye.

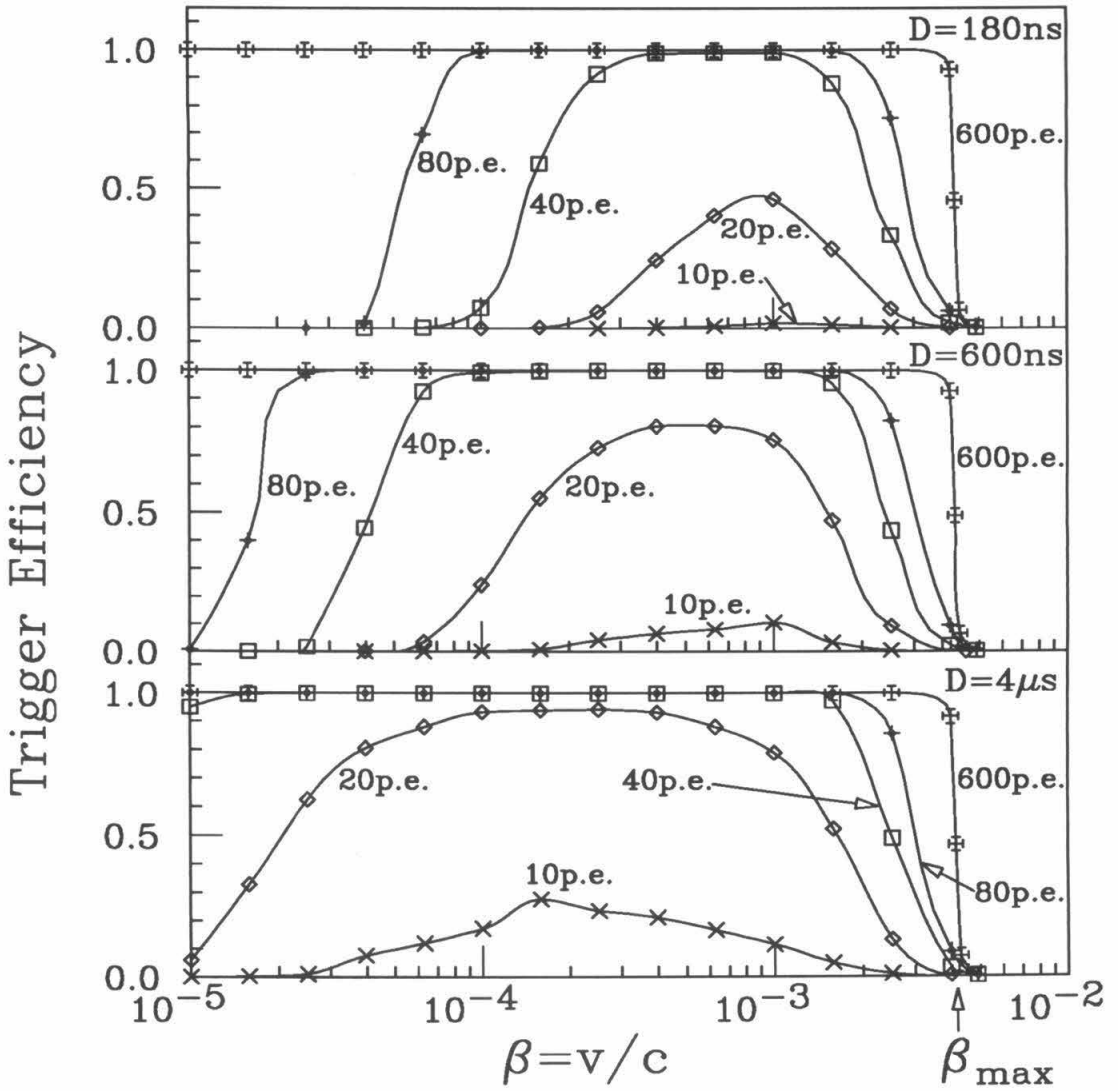


Figure 3.8: Monte Carlo simulation of the slow monopole trigger efficiency. Same as in Fig. 3.7, $\beta_{\max} = 4.2 \times 10^{-3}$ is determined by the pre-set trigger level $C_{tr} = 10$, according to Eq. 3.8. The curves are just guides to the eye.

3.2.4 Implementation in the First Supermodule

The TOHM discriminators used in the first supermodule are in a NIM module and take inputs from PMT signals of 4:1 multiplexed supercounters (Fig. 3.9). The multiplexing scheme is described in more detail in section 3.4. Each module has eight channels and takes care of four scintillator supercounters. The minimum threshold for each channel is adjustable from 8 mV to 100 mV using a trimpot on the front panel. The input of each channel of TOHM is a lemo connector terminated by 50Ω . Each channel has two outputs that drive 50Ω cables.

The Leaky Integrator circuits used in the first supermodule are in a double width CAMAC module. Each module has four input channels and takes care of two supercounters. Input channels zero and one are a pair assigned to both ends of a supercounter and channels two and three are another such pair. The down-counting clock rate R_d was programmable through a CAMAC interface and the setting of its value will be described on page 75. Both the activity and trigger pulses are accessible at lemo connectors on the front panel. A particle crossing one end of a scintillator counter with the earth escape velocity, $3.7 \times 10^{-5}c$, produces pulse trains of minimum durations $17 \mu s$ (since the minimum pathlength is 19 cm) at both ends of the counter. Since the number of photoelectrons received at the near end is roughly eight times greater than that at the far end, the near end signal may satisfy the slow monopole trigger requirement at the beginning of the pulse train, while the far end signal may not satisfy the requirement until the end of the train. Thus, a $20 \mu s$ window is used to generate the coincidence of the two trigger pulses from both ends, which is accessible via a lemo connector on the front panel and employed to freeze the waveform digitizers (WFDs) (Fig. 3.9). Due to the limited time windows of the two WFD systems used (the shorter one is $6.4 \mu s$, *cf.* Table 3.2 on page 70), the timing of the WFD freeze signal is carefully determined to maximize the coverage of the long pulse trains in the WFD time windows. The coincidence of the two activities (the low level triggers) of each pair within $5 \mu s$ is used to mark the beginning of event. The WFD freeze signal is timed to occur

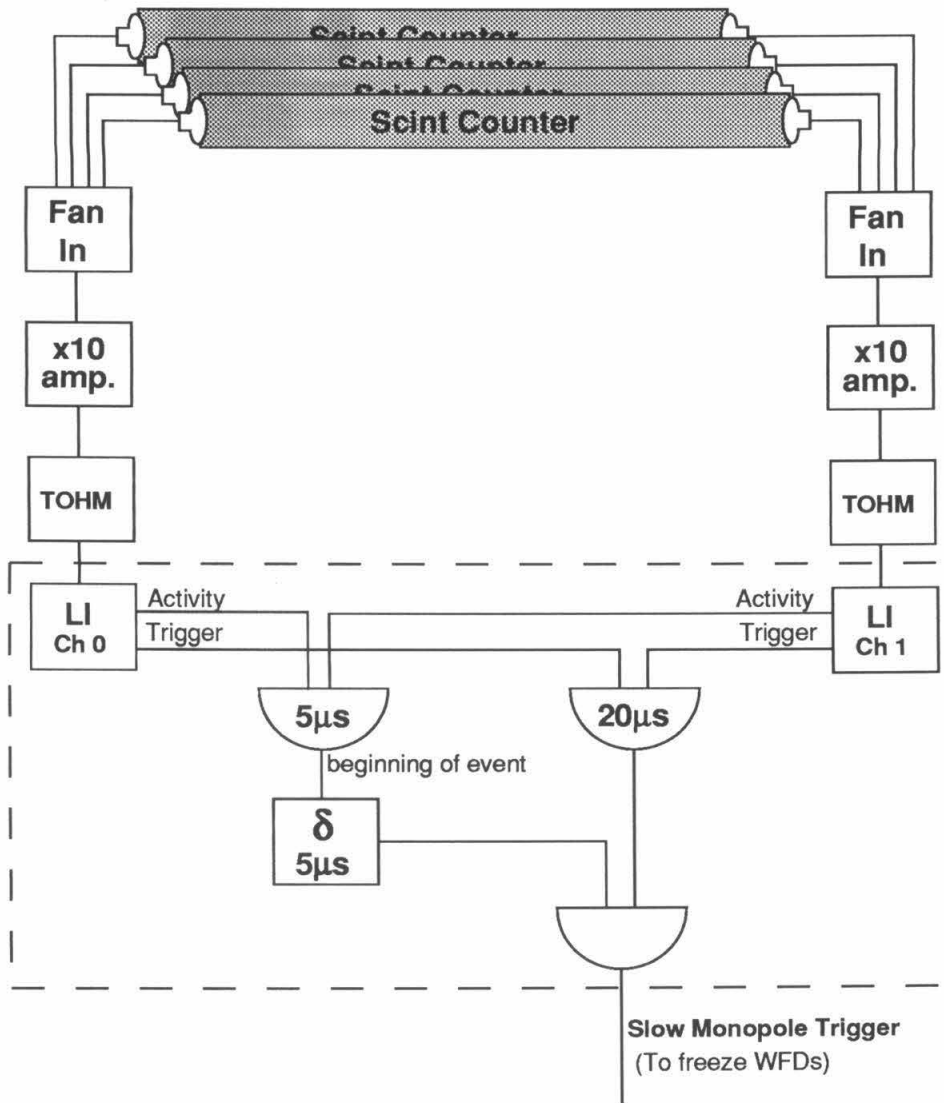


Figure 3.9: The configuration of the slow monopole trigger in the first supermodule. PMT signals are sent to linear fan-outs (not shown in the diagram) and then multiplexed as described in section 3.4. The Leaky Integrator module contains the part of the logic diagram enclosed in the dashed box.

$5 \mu\text{s}$ later than the beginning of the event so that the beginning of the pulse train is placed roughly coincident with the beginning of the $6.4 \mu\text{s}$ WFD time window. However, if the coincidence of the two trigger pulses occurs $5 \mu\text{s}$ later than the beginning of event, the freeze signal occurs $20 \mu\text{s}$ after the beginning of event.

Section 3.4 will describe the overall configuration of monopole electronics, including the slow monopole trigger circuits, in the first supermodule and the optimization of the parameters of the SMT circuits. Improvements to this trigger system have been implemented for full MACRO operation.

3.3 Fast Monopole Trigger

As discussed in section 1.1.4, the fast GUT monopoles are not bound to the galaxy and they are expected to travel at the galactic escape velocity of $10^{-2}c$. Particles traversing the first supermodule, say, vertically, at this velocity have a time of flight (TOF) of about $1.5 \mu\text{s}$ between the center and the bottom faces, while relativistic particles have a TOF of about 15 ns . This TOF is used to establish a fast monopole trigger, based on the conventional coincidence technique. Although in the case of slow monopoles ($\beta \lesssim 10^{-3}$) the coincidence technique cannot be employed (*cf.* page 49), it is possible for fast monopoles because

- A fast monopole has a much shorter TOF than a slow one. For example, the TOF of $1.5 \mu\text{s}$ for a $\beta = 10^{-2}$ monopole is to be compared with the $150 \mu\text{s}$ for a $\beta = 10^{-4}$ monopole. Thus, the coincidence window can be reasonably narrow, reducing the accidental coincidence of the background pulses.
- The $\beta = 10^{-2}$ monopoles have a light yield about 30 times larger than that of muons (Fig. 3.2). Thus, the front end discriminator can have a reasonably high threshold, eliminating most of the radioactivity pulses. Consequently, the background trigger rate due to the accidental coincidence of radioactivity pulses is significantly reduced.

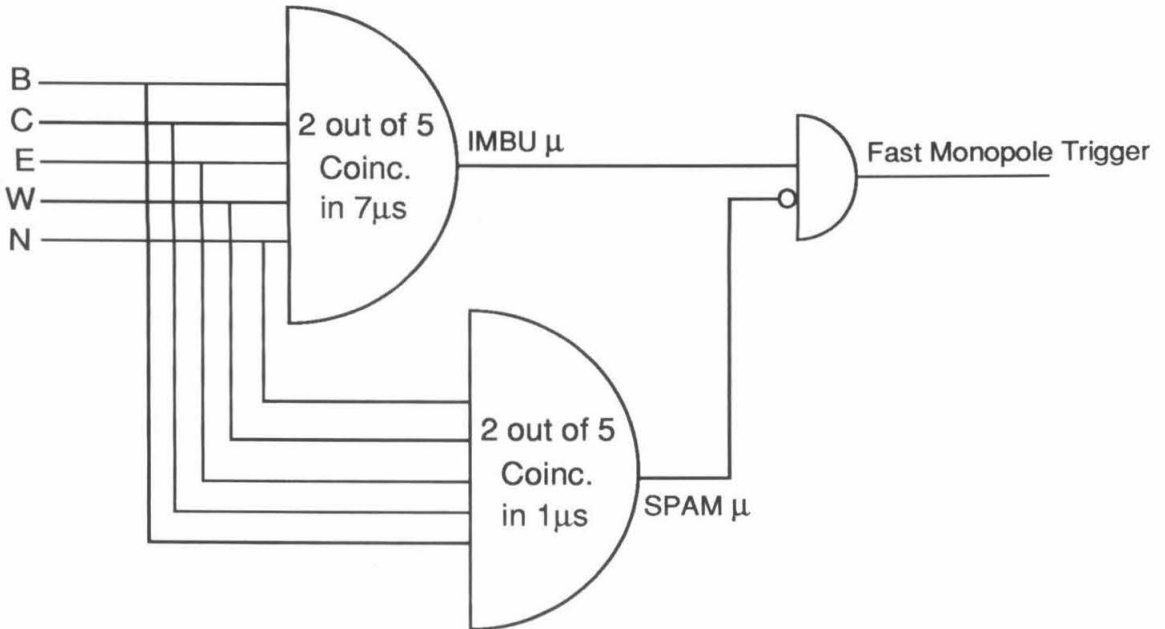


Figure 3.10: Fast monopole trigger.

In the first supermodule, the fast monopole trigger has a coincidence window from $1 \mu\text{s}$ to $7 \mu\text{s}$, selecting those particles having a TOF longer than $1 \mu\text{s}$ but shorter than $7 \mu\text{s}$. This $1\text{-}7 \mu\text{s}$ TOF requirement translates into a velocity range of $2.1 \times 10^{-3} < \beta < 1.5 \times 10^{-2}$ for monopoles with vertical trajectories (Fig. 3.1) since the distance between the center and the bottom face is 4.5 m . This trigger scheme is implemented as the IMBU muon trigger vetoed by the SPAM muon trigger (Fig. 3.10). The IMBU muon trigger has a coincidence window of $7 \mu\text{s}$, selecting particles having velocities greater than 2.1×10^{-3} (assuming vertical trajectories). The SPAM muon trigger has a coincidence window of $1 \mu\text{s}$, and thus its veto rejects $\beta > 1.5 \times 10^{-2}$ particles (again assuming vertical trajectories), mainly the cosmic ray muons. These two muon triggers are described below. This fast monopole trigger system is being replaced for the full MACRO detector.

Consisting of fast particle trigger circuits and ADCs/TDCs, the IMBU system derives its name from and owes credit to the IMB proton decay experiment for which much of the

electronics was originally built and then modified at Boston University for implementation in the first supermodule of the MACRO detector. At the heart of the IMBU system are a charge integrating ADC system with about 2500 pC full scale (9 bit resolution) and two types of TDC: a common stop fast TDC (500 ns full scale) and a common start slow TDC (7 μ s full scale), both having 9 bit resolution. The fast TDC has a better time resolution (~ 1 ns/least count) and is used to measure the time of flight of relativistic particles such as cosmic ray muons. The slow TDC has a longer full scale and is used to measure the TOF of relatively slow particles such as $\beta \approx 10^{-2}$ monopoles. The ADC system is used to measure the ionization of relativistic particles; it is not suitable for slower particles because of its limited gate width. The ionization of slow particles is measured using the waveform digitizers since they have reasonably long time windows as described in the next section.

Most particles traversing the first supermodule cross two active faces, and a few of them cross one active face and the inactive south face. They produce PMT signals at both ends of the scintillator counters they cross. The coincidence of the PMT signals from two faces gives a trigger. A PMT signal from either counter end, when exceeding a discriminator threshold, produces a logical output which starts the fast TDC for that counter. The discriminator threshold is set to be less than 1/4 of the minimum ionizing muon pulse height, sufficiently low to select most muons and fast monopoles while rejecting most of radioactivities. A coincidence of the discriminator output within 100 ns from both ends of any counter in a face produced a face pretrigger. The first established face pretrigger (*i.e.*, the one from the first counter the particle enters) serves as the common stop of the fast TDCs and the common start of the slow TDCs. After being started, the slow TDC is stopped by the subsequently-arriving discriminator output, or reaches the full scale if there is no subsequent discriminator output. To improve the limited dynamic range of the IMBU system and to handle PMT saturation from heavily-ionizing particles, two identical sets of IMBU channels are implemented, one for PMT anode signal, the other for the

dynode signal, $\sim \frac{1}{15}$ of the anode signal.³ The majority coincidence of the dynode face pretriggers from two out of the five faces of the detector within $7 \mu\text{s}$ establishes an IMBU muon trigger since a particle crossing the detector goes through two faces only. To produce a fast monopole trigger, this IMBU trigger is vetoed by another muon trigger, the SPAM trigger. The SPAM muon trigger uses only commercially available electronics such as discriminators, coincidence units, etc. It has the same coincidence requirement as the IMBU muon trigger, but with a time window of $1 \mu\text{s}$.

Most IMBU trigger events and SPAM events are from cosmic ray muons. Their rates are both higher than the muon rate in the first supermodule, 130 muons per hour, typically by 10-15%. The IMBU trigger vetoed by the SPAM gives the fast monopole trigger, whose rate is about ten events per hour. These events are mainly caused by the accidental coincidence of radioactivity pulses. At the beginning of this data taking, occasionally there was a sporadic increase of the fast monopole trigger rate. The reason was later found to be that the IMBU threshold was set so low that a small increase in PMT gain, a small reduction in the threshold itself, or environmental electrical noise gave relatively large increase in the trigger rate. The threshold on such counters was later increased by less than 10% and the trigger rate subsequently became quite stable.

3.4 Configurations in the First Supermodule

The first supermodule had its initial data taking run from February 27 to May 30, 1989. During summer 1989, we made significant improvements to the detector, including turning on its north face (giving increased acceptance), less multiplexing and reduction of ground loop noise (allowing more sensitive monopole triggering), etc. From October 25, 1989 to November 12, 1991, the first supermodule had an extended data taking run under this improved configuration and this data set is used for the monopole search in this thesis. This

³In this thesis, the term "PMT signal" means the anode signal, unless explicitly stated otherwise.

Face	Supercounter	Counters
Bottom	B1	1B01-1B04
	B2	1B05-1B08
	B3	1B09-1B12
	B4	1B13-1B16
Center	C1	1C01-1C04
	C2	1C05-1C08
	C3	1C09-1C12
	C4	1C13-1C16
East	E1	1E01-1E04
	E2	1E05-1E07
West	W1	1W01-1W04
	W2	1W05-1W07
North	N1	1N01-1N04
	N2	1N05-1N07

Table 3.1: Multiplexing scintillator counters into supercounters. For the nomenclature of the counters, see page 27.

section describes the overall configuration of the monopole-related scintillator electronics for this run. The configuration for the previous run in spring 1989 is also described when a comparison is needed. For the non-monopole-related electronics, see reference [69].

Due to limited electronics available for these two data taking runs, the scintillator counters were multiplexed into *supercounters* before their signals were fed into the slow monopole trigger circuits and the waveform digitizers (WFDs) (Table 3.1, also see Fig. 3.9 and Fig. 3.11). This 4:1 multiplexing increased the singles counting rate in each channel by a factor of four. Furthermore, the multiplexer (linear fan-in) itself introduced extra electronic noise (Fig. 3.13). These increased backgrounds limited the choices of parameters of slow monopole trigger (SMT) circuits, thus requiring a less sensitive SMT trigger than would be possible with an unmultiplexed system. This 4:1 fan-in is to be compared with the 8:1 multiplexing used for the horizontal counters in the spring 1989 run; less multiplexing

allows a better trigger sensitivity. However, the inputs to the fast monopole trigger and the IMBU ADC/TDC system are not multiplexed.

Besides the search for slow-moving supermassive GUT monopoles which produce a very small amount of scintillation light in the very low β region, MACRO also searches for other types of heavily ionizing particles with lighter masses (thus moving at higher velocities) which yield much more light. For example, a relativistic Dirac monopole loses energy through ionization at a rate 4700 times greater than a minimum ionizing muon, since its magnetic charge is 68.5 greater than the electron charge. In order to have as large a dynamic range as feasible to accommodate the wide range of possible signal size, the PMT *gain* was set nominally at 5×10^6 , corresponding to an average single photoelectron pulse height of ~ 3 mV. However, the very slow GUT monopoles leave their signatures as long trains of single photoelectron pulses (Fig. 3.4). Both the trigger and measurement electronics, *i.e.*, the SMT and the WFD, have to process these signals at the SPE level. The lowest possible threshold of the TOHM discriminator is ~ 8 mV. The internal noise of the WFD is ~ 1 -2 mV. Thus, in order to detect the very slow monopoles, inputs to both the SMT and the WFD were amplified ten times (Fig. 3.9 and Fig. 3.11).

To record the qualitatively different signals from monopoles of different possible velocities, two sets of waveform digitizers (WFDs) were used in the implementation of the first supermodule (Table 3.2). Clocked at 50 MHz, LeCroy 2261 modules were used as the fast WFDs, matching the ~ 30 ns widths of muons signals. Their 11 bit dynamic range of the digitizing amplitude gives a full scale of 2 V with 1 mV per least count. This feature and their $6.4 \mu\text{s}$ time window allow the proper recording of various PMT signals from relatively fast monopoles. Signals from slower monopoles have longer duration and a much less demanding dynamic range of pulse heights. Fabricated at Texas A&M University, the slow WFDs are clocked at 20 MHz, giving a longer time window of $22.75 \mu\text{s}$, allowing the recording of long pulse trains from slow monopoles. Their digitizing amplitude has an 8 bit dynamic range with 1 mV per least count, sufficient for the low ionization of slow

Name	Type	Speed (MHz)	Number of Samples	Time Window (μ s)	Dynamic Range	Voltage Resolution (mV/count)
Fast WFD	LeCroy 2261	50	320	6.4	11 bits ^a	1
Slow WFD	Texas A&M Units	20	455	22	8 bits	1

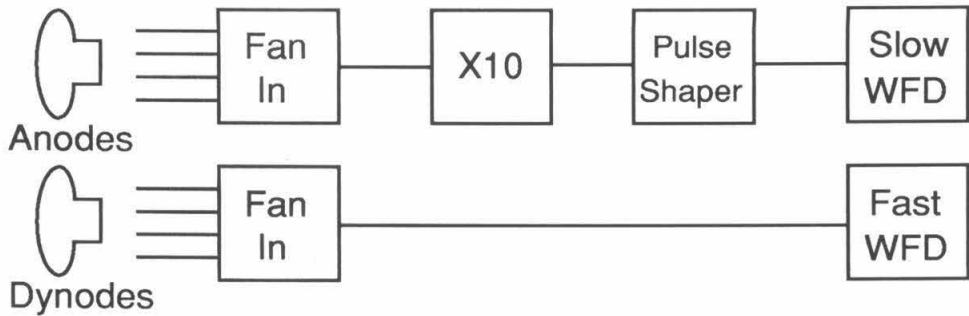
^aThe LeCroy 2261 module has 12 bit dynamic range for a bipolar pulse, but only 11 bits can be used for a negative-going pulse.

Table 3.2: The two sets of waveform digitizers.

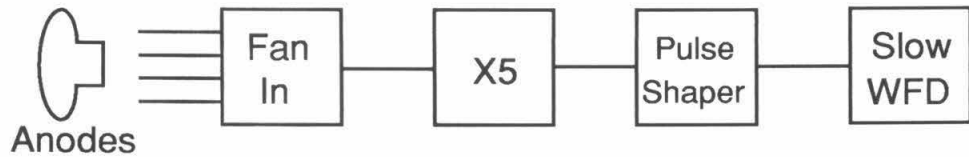
monopoles. To digitize input pulses, both WFDs use charge coupling devices (CCDs), resulting in waveform baseline drifts intrinsic to any CCDs (Fig. 4.21 on page 122). The configurations of the WFDs changed twice, as shown in Fig. 3.11. Since the average SPE width is ~ 15 ns but the slow WFDs digitize a sample every 50 ns, the amplified PMT signals were stretched by pulse shapers. The ability of the slow WFDs to see a single photoelectron train is demonstrated in Fig. 3.12, which shows the waveforms of LED-generated long pulse trains as recorded by the slow WFD in configuration B shown in Fig. 3.11. Since the LED was located at one end of a counter, the pulse train from the far end consisted of single photoelectrons while the near end pulse was much larger.

Waveforms were recorded for the two monopole triggers and one muon trigger. The OR of the slow monopole triggers from the supercounters in a face established a face trigger, which froze the WFDs of that face. The longest time of flight for a $\beta = 10^{-4}$ particle to pass through the first supermodule, *i.e.*, the time in traversing its two opposite corners, is 600μ s. Therefore, all face triggers within 600μ s were treated as one event and their OR caused the computer to read out the waveforms and other data. The relative timing between WFD freeze signals for different faces from the slow monopole triggers was recorded by a latching scaler clocked at 5 MHz, which could be used to calculate the

Config. A: From 25 Oct 1989 to 8 May 1990 (Runs 784-1668).



Config. B: From 8 May 1990 to 6 Nov 1990 (Runs 1669-2585).
The fast WFD is configured same as A.



Config. C: From 7 Nov 1990 to 12 Nov 1991 (Runs 2586-4120).

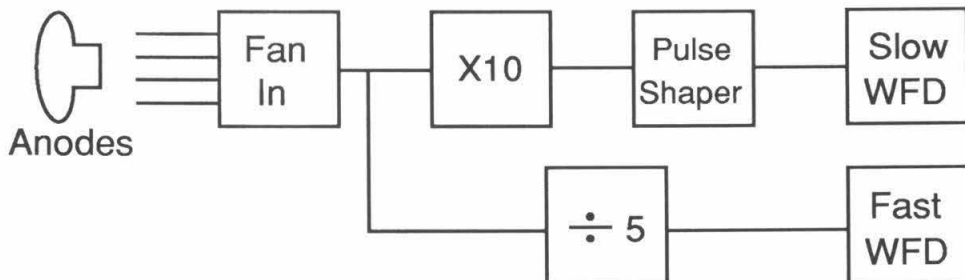


Figure 3.11: WFD configurations in the first supermodule.

LED Generated Pulse Trains

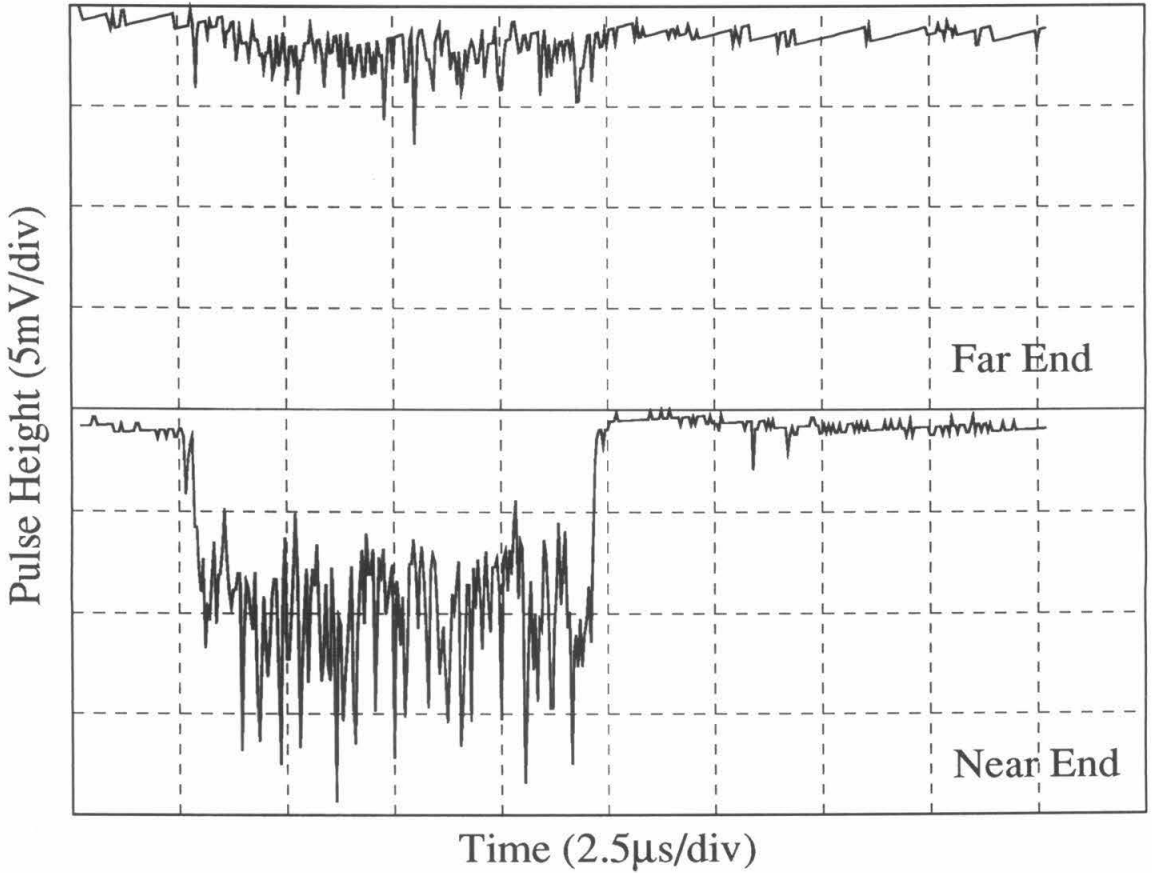


Figure 3.12: LED generated pulse trains as recorded by the slow WFD. The waveform baseline drift (intrinsic to CCD devices) is subtracted. The indicated scale for pulse heights is for the signal before the amplifier. The LED is located at one end of counter 1W05. The signal at the far end (the top trace) is a single photoelectron pulse train containing about 80 photoelectrons. They are consistent with the Monte Carlo generated pulse trains in Fig. 3.4 on page 53.

time of flight of slow particles. The information about which supercounter had either a trigger or an activity was recorded using a LeCroy 4448 coincidence register.

The fast monopole trigger and the SPAM muon trigger were produced by coincidence between faces (Fig. 3.10) and they froze the WFDs all at the same time instead of freezing each face at a different time. This is acceptable because the length of the coincidence window ($7 \mu\text{s}$) is comparable to that of the waveform sample windows and consequently signals are properly placed in the slow waveform window and almost properly in the fast waveform window.

The sensitivity of the SMT circuit to slow monopoles greatly depends on the choice of its parameters, which in turn is limited by the environmental noise — electrical noise or natural radioactivities. The challenge is to achieve the best possible trigger efficiency for a trigger rate low enough for the data acquisition system to tolerate. In the summer after the spring 1989 run, we discovered that much electrical noise was caused by the ground loops consisting of the PMT high voltage cable ground, the anode-to-fanout cable ground, and the dynode-to-fanout cable ground (Fig. 3.13). Running from the first supermodule to the counting house, these cables were about 40 m long. To break the ground loop, we put a 150Ω resistor in the high voltage cable ground and a 10Ω resistor in the dynode-to-fanout cable ground. Studies showed that pulse shape distortions due to these resistors were negligible. After fixing the ground loop noise, we were able to set TOHM threshold as low as 25 mV, corresponding to 2.5 mV before amplification, which was below the average single photoelectron level of 3 mV. Compared to the threshold in spring 1989 run of $\gtrsim 8 \text{ mV}$, this improved the sensitivity of the slow monopole trigger by five times in detectable light yield.

Another type of electrical noise came from PMT discharges, which occurred when end chambers of scintillator counters were not filled with oil and thus were quite humid. These discharges displayed themselves as wide ($\sim 1 \mu\text{s}$), wiggly pulse trains, properly satisfying the SMT trigger requirements. They contributed significantly to the background trigger

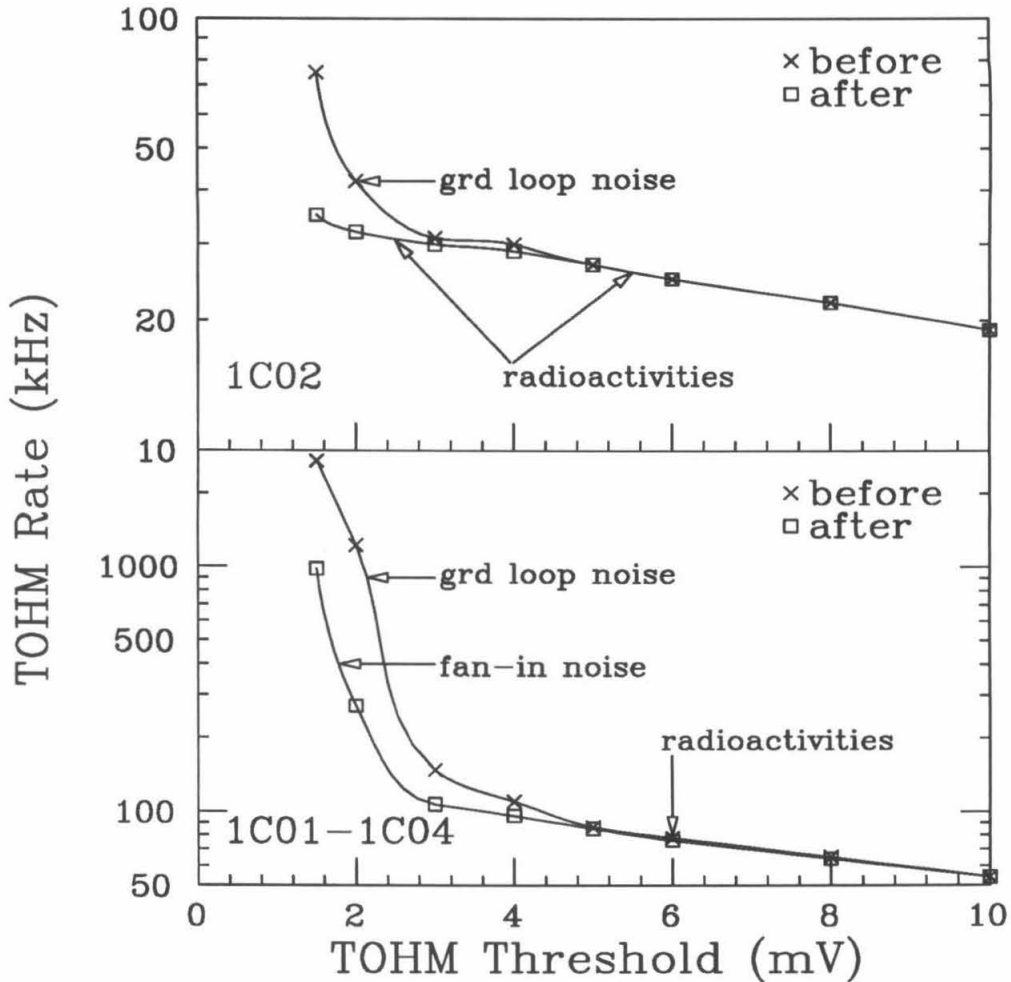


Figure 3.13: Ground loop noise reduction. Shown are the background singles counting rates before and after breaking the ground loops. The top figure is for an end of counter 1C02 and the bottom one is for an end of the multiplexed supercounter 1C01-1C04 (or C1 in the nomenclature in Table 3.1). A TOHM was used as the discriminator to measure the singles rates. An $\times 10$ amplifier was used to achieve the low thresholds — the plotted thresholds reflect those before amplification. Ground loops contribute significantly to the low level noise, which is dominated by noise introduced by the fan-in after the reduction of the ground loop noise. At higher thresholds, the singles rates are dominated by radioactivity pulses.

rate. While the end chambers of the horizontal counters were filled with pure mineral oil in summer 1989 before this run started, those of the vertical counters were filled in February 1990 during the run. This operation significantly reduced the PMT discharges, allowing a better choice of the SMT parameters as detailed below.

The trigger level of the Leaky Integrator was set as $C_{tr} = 16$. Consequently, according to Eq. 3.8 on page 57, the high β cutoff of the SMT sensitive range was $\beta_{max} = 3 \times 10^{-3}$, slightly overlapping with the sensitive β range of the fast monopole trigger. The selection of the activity level affects the timing of the beginning of event. A low activity level allows the activity to occur near the very beginning of a pulse train, but it also increases the background activity rate. If the activity rate is too frequent, the background activity confuses the true beginning of event. The activity was thus chosen as $C_{act} = 6$ for the first year of data taking (October 1989 to November 1990). As shown in Figs. 3.7-3.8 and also implied by Eq. 3.9, a slow down-counting clock rate improves the SMT sensitivity to monopoles. But it also inevitably increases the background trigger rate. A slow monopole trigger causes the recording of waveforms, which occupy much more space on data tapes than data from other acquisition systems (*e.g.*, ADC/TDC). Because of this, the slow monopole trigger rate had to be reasonably low. Initially, it was preferred to be around 10 events per hour. This limited the down-counting period as $D = 180$ ns for the first year.

As mentioned above, the PMT discharges were reduced as a result of filling the end chambers with pure mineral oil, lowering the background trigger rate. In fall 1990, a feature was added to the data acquisition system which compressed the waveform data using Huffman's algorithm [89,90], reducing the waveform data size by a factor of ~ 5 and allowing the acquisition system to tolerate a higher SMT rate. As a result of these two changes, on November 9, 1990, the down-counting clock period was increased to $D = 420$ ns for the center, bottom and north faces, and $D = 600$ ns for the east and west faces to improve the trigger sensitivity in the low β region. The east and west faces have lower radioactivity singles rates because of their smaller volume, allowing a slower

down-counting clock than other faces. Because of the reduction in PMT discharge noise, the activity level was reduced to $C_{\text{act}} = 3$, giving a better timing of the beginning of event. After these changes, the average SMT rate is around 60 per hour. Thus, in the second year (November 1990 to November 1991) of data taking, the slow monopole trigger had a better sensitivity to slow monopoles than in the first year. However, to be conservative, we only quote our sensitivity as that of the first year, which is based on the measurement described in below.

3.5 Measurement of Slow Monopole Trigger Sensitivity

Described in this section is the empirical measurement of the sensitivity of the slow monopole trigger circuit. For the measurement, LEDs were driven by square pulses to generate wide phototube signals of various widths, in order to simulate passages of slow particles at various velocities. For each given width, the pulse amplitude was adjusted to trigger the SMT circuit at 90% trigger efficiency. The number of photoelectrons in the pulse train was measured using an ADC and then compared with the number of photoelectrons from a minimum ionizing particle. Thus, we obtain the light yield (in units of the minimum ionizing particle's light yield) required to trigger the SMT circuit at 90% efficiency. This is to be compared with the predicted light yield of slow monopoles or other slow particles.

The sensitivity measurements were performed sequentially on four arbitrarily chosen counters, 1C15, 1W05, 1B06 and 1N02 for six different pulse train durations from 200 ns to 5 μ s. At each setting, square pulses were generated by a Hewlett-Packard 8013B pulser and fed to one of the four LEDs in the counter. A LeCroy visible scaler was used to measure the pulser rate and the SMT trigger rate; the ratio of the latter over the former defined the trigger efficiency. The LED intensity was adjusted until the trigger efficiency was approximately 90%. This was a delicate adjustment because the efficiency depended on the light level which in turn depended on the amplitude of the LED-driving pulse and

both of these dependences were very steep functions. Trigger efficiencies from 70% to 95% were accepted. The LED was located at one end of the counter and the PMT signal from the near end was much larger than the signal from the far end (Fig. 3.12). If the signal from the far end triggered the SMT circuit with 90% efficiency, the near end signal would trigger with 100% efficiency. Hence the coincident trigger efficiency was completely determined by the far end signal. In this section, the term “PMT signal” implies the PMT signal at the far end from the LED.

Once the desired efficiency was achieved, a LeCroy 2249W wide-gate ADC (10 μ s maximum gate width) was employed to measure the number of photoelectrons in the LED pulse. At each setting, more than 5000 pulses were recorded and the ADC counts were histogrammed and fit to Gaussian distribution, an example of which is shown in Fig. 3.14. The ADC pedestal was also measured for each setting. From the photoelectron statistics, the gain of the PMT in ADC counts/photoelectron can be determined using the relation

$$G = \frac{\sigma^2 - \sigma_P^2}{2(\mu - \mu_P)} \quad , \quad (3.12)$$

where μ and σ are the Gaussian fit mean ADC and the standard deviation for the LED pulse, μ_P and σ_P , for the pedestal. The factor of two is due to the dynode statistics (Appendix B). Thus, a linear fit is performed to σ^2 as a function of μ (Fig. 3.15) and we obtain the PMT gain G as half of the fit slope. Using the LeCroy 2249W ADC specification of 0.25 pC/count \pm 5% [91], the PMT gain in ADC counts can be converted into absolute PMT gain. The results are listed in Table 3.3.

These gains were subsequently used to determine the numbers of photoelectrons for the measured counters at different settings,

$$N_{pe} = \frac{\mu - \mu_P}{G} \quad , \quad (3.13)$$

which are plotted in Fig. 3.16. At a given setting, *i.e.*, a given pulse train duration, the required light levels at 90% trigger efficiency are quite similar to each other for different counters, except for the very short pulses discussed below. The thin curve is drawn

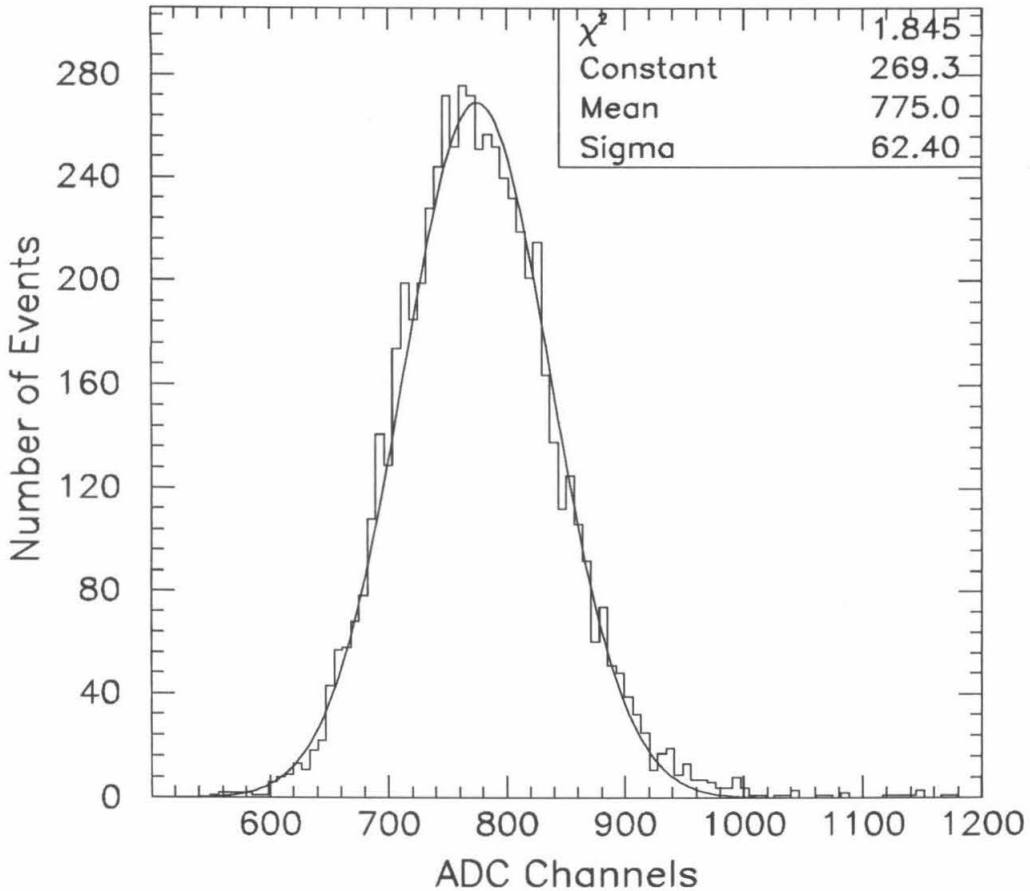


Figure 3.14: An example of an ADC distribution and its Gaussian fit for the SMT sensitivity measurement. Shown in the upper right corner are the chi-square per degree of freedom, the normalization constant, the mean and the standard deviation. This histogram is for counter 1W05 with pulse train duration $3 \mu\text{s}$. For comparison, the Gaussian fit of the pedestal for this setting gives a mean of 345.4 and a standard deviation 13.1. The outliers on the high side are from extra radioactivity pulses within the wide gate of the ADC.

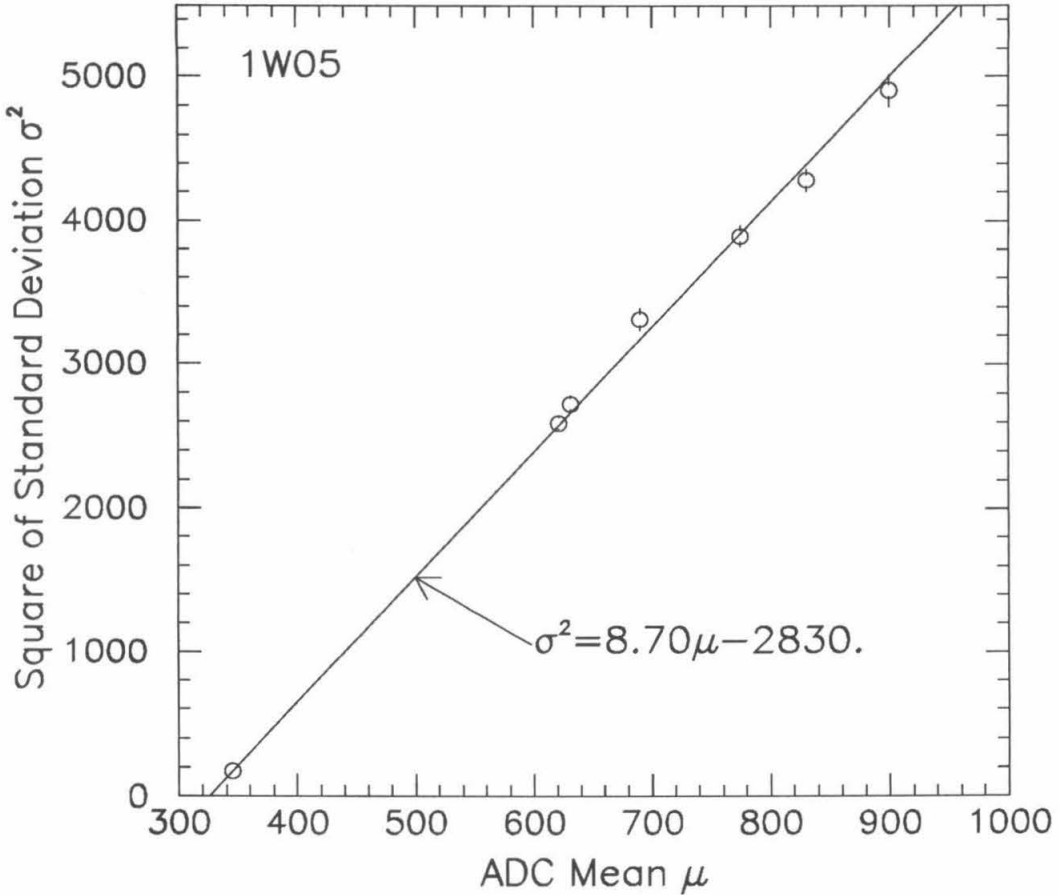


Figure 3.15: The squares of the Gaussian fit standard deviations of ADC distributions σ^2 as a function of the mean ADC μ . An example of an ADC distribution and its Gaussian fit is shown in Fig. 3.14. The line is the best linear fit and its slope is twice the PMT gain. The fit chi-square per degree of freedom is 1.36. The measurement at the lower left corner is for the pedestal and other measurements are for various pulse train durations for counter 1W05.

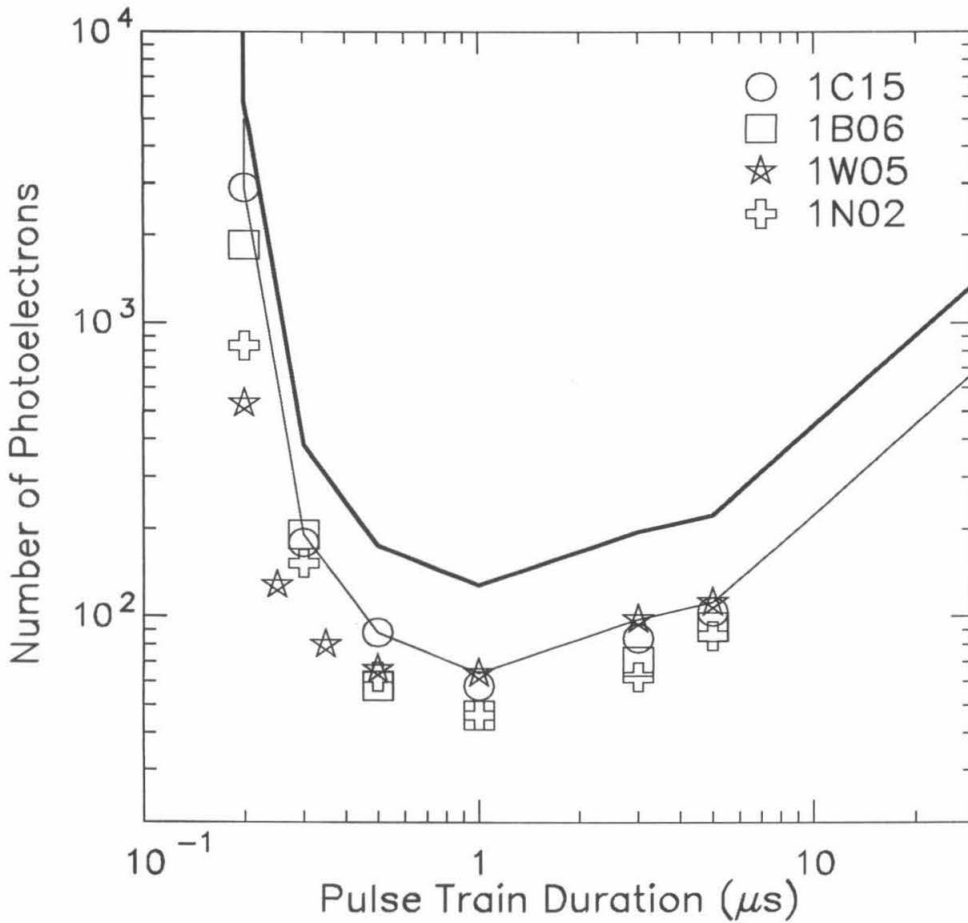


Figure 3.16: The slow monopole trigger sensitivity curve. Plotted are the required numbers of photoelectrons as a function of the pulse train durations at 90% trigger efficiency. The measurements were done on four arbitrarily chosen counters. The thin curve is drawn through the worst case measurements and the line for pulse trains longer than 5 μs is a conservative upper limit on the required signal size given by Eq. 3.14. To take care of counter to counter variations, this curve is multiplied by a conservative factor of two, which gives the thick curve. This thick curve is used to obtain the quoted sensitivity shown in Fig. 3.18 and Fig. 3.19.

Counter End	PMT Gain (ADC Count/PE)	Absolute PMT Gain ($\times 10^6$)
1B06-0	4.69 ± 0.07	7.3 ± 0.4
1C15-0	4.19 ± 0.07	6.5 ± 0.4
1W05-0	4.35 ± 0.04	6.8 ± 0.4
1N02-0	6.21 ± 0.06	9.7 ± 0.5

Table 3.3: PMT gains obtained in the sensitivity measurement.

through the worst counter for each pulse train duration. To take care of counter to counter variations discussed below, this worst case curve is multiplied by a conservative factor of two, yielding the thick curve. This thick curve is later used to calculate the SMT sensitivity, making the resulting sensitivity very conservative. No measurements were made for pulse trains of durations $\mathcal{T} > 5 \mu\text{s}$, partly because the LeCroy 2249W ADC has a maximum gate width $10 \mu\text{s}$, partly because in the first supermodule setup, a pulse train with $\mathcal{T} > 5 \mu\text{s}$ was properly recorded by the waveform digitizer only if the SMT trigger occurred within $5 \mu\text{s}$ after the beginning of event. However, we can set an upper limit on the required signal size $N_{\mathcal{T}}$ for $\mathcal{T} > 5 \mu\text{s}$ by noting that if any $5 \mu\text{s}$ part of a long pulse train can fire the SMT alone, the whole pulse train must be able to trigger as well. Since the penetrating monopoles produce scintillation light uniformly in time (fluctuations are averaged out in the microsecond scale), this limit is

$$N_{\mathcal{T}} = N_{\mathcal{T}_0} \frac{\mathcal{T}}{\mathcal{T}_0} \quad , \quad \text{for } \mathcal{T} \geq \mathcal{T}_0 = 5 \mu\text{s} \quad (3.14)$$

as shown in Fig. 3.16. As has been discussed, the Leaky Integrator acts like a width discriminator, whose threshold is ideally 240 ns for the chosen SMT parameters (*cf.* page 75). This threshold displays itself as a steep rise on the left side in Fig. 3.16. Ideally the SMT should not fire for the pulse duration 200 ns (the leftmost setting in the plot). However, when fed a pulse larger than $\sim 1 \text{ V}$ (signal size before the $\times 10$ amplifier), the TOHM

gives an output pulse wider than the input's width at half maximum. This characteristic varies from channel to channel, which explains the variations of the four measurements for 200 ns pulse trains shown in the plot. To be conservative, a cut of minimum width 200 ns is imposed on the sensitivity of the SMT circuit, even though the SMT may still be triggering when fed a shorter but larger pulse.

These measurements were done on only four arbitrarily chosen counters. To apply the results to all counters in the first supermodule, we need to study counter to counter variations. As shown in Fig. 3.16, the four measurements approximately agree with each other, except the big variations at the 200 ns duration discussed above. Counter to counter variations can only be caused by channel to channel differences of the SMT circuits or by variations in the PMT gains. Bench tests showed that both the TOHM and the Leaky Integrator circuits behaved essentially the same from channel to channel, which is expected since the Leaky Integrator is a digital circuit and the TOHM is just a fancy discriminator using relatively simple circuitry. All PMTs in the first supermodule were *nominally* set at a gain of 3 mV/pe, but their actual gains varied from counter to counter (Fig. 3.17). It turns out that the PMT gains of three of the four arbitrarily chosen counter ends are about the same as the average gain. The upward variation in gain increases the monopole sensitivity. The gains of the counters with the worst downward variations is roughly about the half of the average gain and we have studied its implications to the monopole sensitivity using the Monte Carlo simulations described in Appendix C. The Monte Carlo demonstrated that, as the gain is reduced by a factor of two, the required amount of light at 90% trigger efficiency increases by a factor less than two, depending on pulse train durations (Fig. C.2). This factor is about 1.8 for pulse trains longer than 5 μ s. This Monte Carlo result qualitatively agrees with the LED measurements: one of the measured counters, 1N02, has a gain of $\sim 40\%$ larger than others, and it requires less light by about the same factor to achieve the 90% trigger efficiency. To conservatively take care of the counter to counter variations, we multiply the worst case measurements (the thin curve in Fig. 3.16) by a factor of two

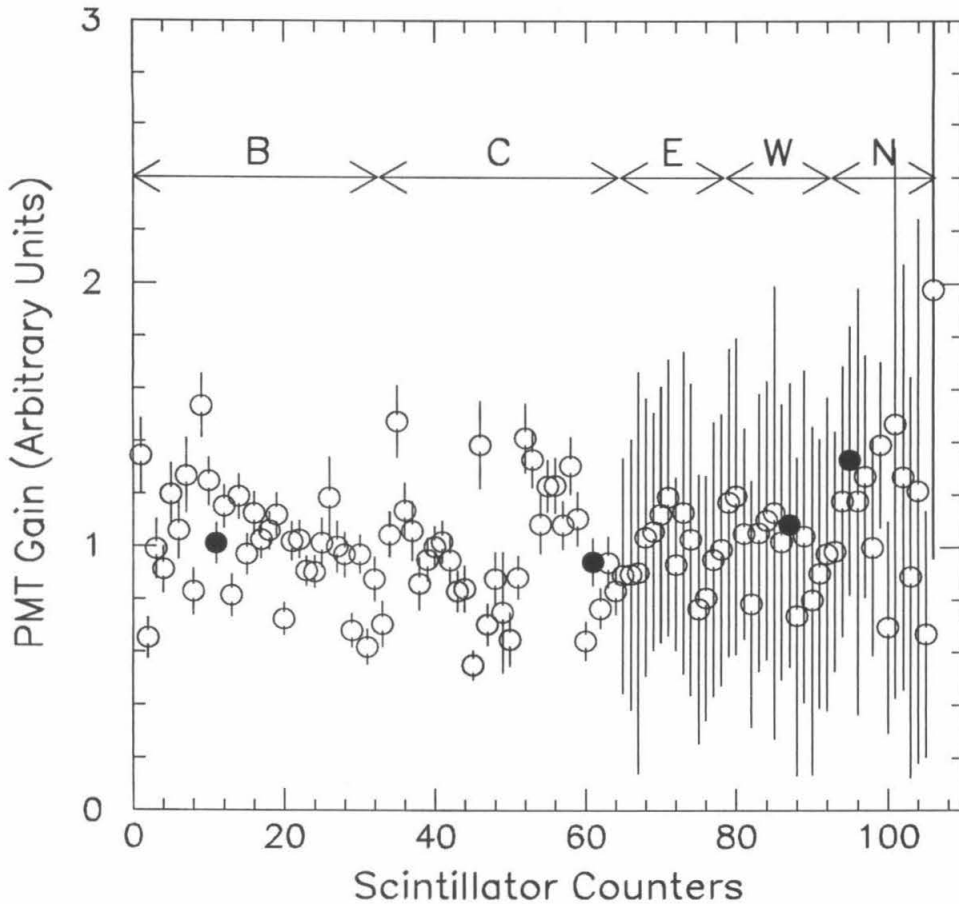


Figure 3.17: Counter to counter variations of the PMT gains. There are 53 counters or 106 counter-ends in the first supermodules. The data are obtained from muon signals normalized by their pathlengths and corrected for their locations along a counter. Also corrected for are the different light collection efficiencies for horizontal and vertical counters. The large errors in vertical counters (in the east, west and north faces) are due to the large uncertainties in determining the pathlengths. The blackened circles indicate the channels in which monopole sensitivity was measured, and their gains agree with Table 3.3 within errors.

and obtain the thick curve in Fig. 3.16. This thick curve is also plotted in Fig. C.3, which shows that it is very conservative, compared with the Monte Carlo results using half the average gain. We are confident that this thick curve is conservative even if it is applied to the worst counters.

Now we can express our trigger sensitivity at 90% efficiency in terms of the light yield and the velocity of penetrating particles. The velocity is obtained from the aforementioned pulse train duration assuming the minimum pathlength 19 cm through the scintillator; this is conservative because if a particle with the minimum pathlength can fire the monopole trigger circuit, the particle with the same amount of ionization per unit pathlength must be able to fire the trigger circuit as well. The light yield is obtained by dividing the above measured number of photoelectrons required for 90% trigger efficiency (the thick curve in Fig. 3.16) by the number of photoelectrons from minimum ionizing particles. Thus, the unit used for the light yield is minimum ionizing light yield instead of the usual unit MeV/cm. The amount of the minimum ionizing light yield is scintillator dependent because the absolute scintillation efficiency depends on the scintillator. Measurements show that 1.2×10^3 photoelectrons are observed when a minimum ionizing cosmic ray muon passes through the center of the horizontal scintillator counter (Fig. 2.8). To be conservative, we shall use the light yield from a muon hitting the far end of the counter, which is 7.3×10^2 photoelectrons. The same quantity for a vertical counter is 3.8×10^2 photoelectrons. The required light yield at 90% trigger efficiency and specific light yields from various supermassive particles (section 3.1) are plotted in Fig. 3.18 and Fig. 3.19.

In the same two plots, we also show the sensitivity curve of the fast monopole trigger circuits (FMT). The discriminator threshold of the FMT is set to be less than 1/4 of the muon pulse height. Since the muon pulse width is 30 ns, we obtain the sensitivity line shown with a negative slope; it is cut off at both ends because of the 1-7 μ s time of flight requirement (see Fig. 4.33).

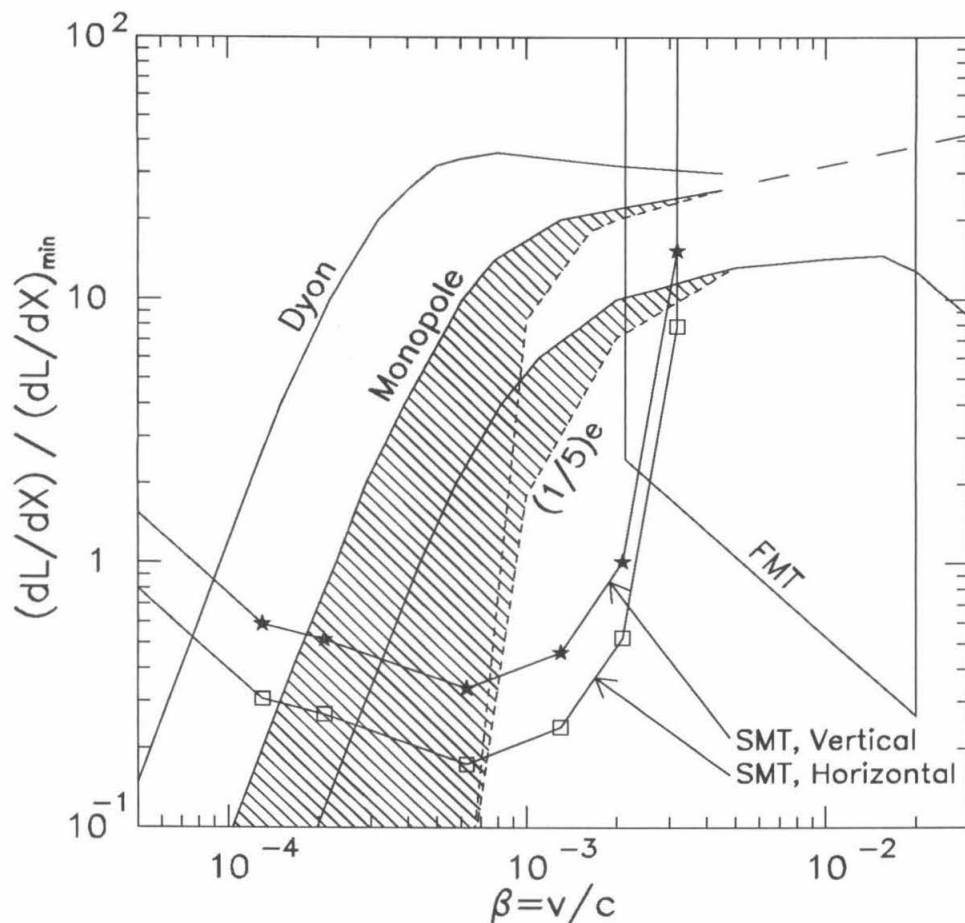


Figure 3.18: Sensitivities of the monopole trigger circuits as compared with expected light yield from the ionization of charged supermassive particles. Shown are the sensitivity curves of the required light yield versus the velocity for the slow monopole trigger circuits (SMT) at 90% efficiencies for the horizontal counters and the vertical counters. The probability for a particle with light yield above the curves to fire the SMT is greater than 90%. Also plotted is the sensitivity of the fast monopole trigger circuits (FMT). For comparison, the expected light yield from the ionization of magnetic monopoles, dyons and $(1/5)e$ charge particles (Fig. 3.2) is shown as well. The light yield is in units of the light yield of minimum ionizing particles.

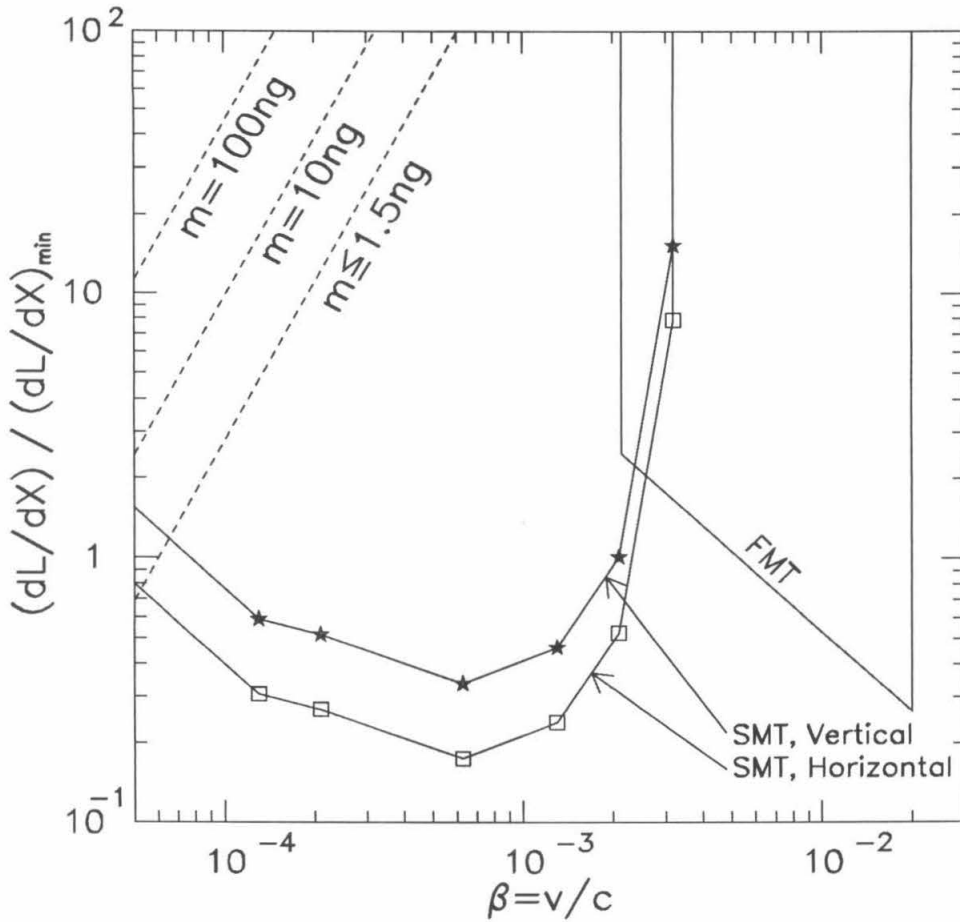


Figure 3.19: Sensitivities of the monopole trigger circuits as compared with expected light yield from the black body radiation of nuclearites of various masses. Shown are the sensitivity curves for the slow monopole trigger circuits (SMT) at 90% efficiencies for the horizontal counters and the vertical counters, the same as in Fig. 3.18. Also plotted is the sensitivity of the fast monopole trigger circuits (FMT). For comparison, the expected light yield from the black body radiation of nuclearites of various masses (section 3.1.2) is shown as well. The light yield is in units of the light yield of minimum ionizing particles.

3.6 Conclusions

In this chapter, we have discussed the ideas and the circuitry of the two monopole triggers and their configurations in the first supermodule. Each of them is sensitive to monopoles at their respective velocity range. We have also described the empirical measurements of the slow monopole sensitivity.

Chapter 4

Data Analysis

In the previous chapter we have described the trigger and measurement electronics for search for GUT monopoles with the first supermodule of the MACRO experiment. This chapter presents the analyses of the data collected using the described apparatus to search for monopoles. A quality assessment of data selected for these analyses is given in section 4.1. As described in the previous chapter, there are two different types of monopole triggers. The analyses of data collected from these two triggers are quite independent to each other: the analysis of data from the slow monopole trigger system is given in section 4.2, while the fast monopole analysis is given in section 4.3.

4.1 Run Selections

In the MACRO experiment, the scintillator counters and the streamer tubes are operated independently, in the sense that one system may be working while the other may be turned off. To accurately assess the quality of the scintillator data, I define a *scintillator muon* as the majority two AND of the three scintillator muon triggers used in the first supermodule: two of which (SPAM and IMBU muon triggers) are described in section 3.3 and also in figure 3.10 on page 65; the other scintillator muon trigger is the ERP muon trigger [69],

which is a single face trigger based on the amount of energy deposition. Since the ERP trigger is not used in this thesis except here, I am not going to discuss it in detail in this thesis. Thus defined, this scintillator muon signal is a very good indicator on whether the scintillator counters were functioning normally and its average rate is $134 \pm 5 \text{ hr}^{-1}$.

As previously said, this thesis uses data collected from October 25, 1989 to November 12, 1991. The data taking is performed in units of runs; a run is a continuous period of data collection with the detector undisturbed. On average a normal run lasts about ten hours. Each run's livetime is computed as the time difference between the first and the last scintillator muon in that run (further dead time corrections will be described in the next paragraph). Under normal running conditions, this livetime is slightly smaller than the real livetime, but the average discrepancy is less than 1 minute per run: Since the average muon rate is roughly two per minute, the first muon occurs less than ~ 30 seconds later than the start of run, and the last muon, ~ 30 seconds earlier than the end of run. Thus, this error is $\leq 0.2\%$ for a typical run lasting ten hours and it is on the conservative side (the calculated livetime is smaller than the real livetime), so it is ignored. For some abnormal runs, this approach is an improvement over using the run duration as the livetime: In the first supermodule, power flickers frequently turned off the high voltage supply (HV) for the scintillator PMTs during a data run, while leaving other parts of the detector intact. Some of these occurrences were corrected immediately by the shift workers (e.g., by stopping the run, turning on the power supply and starting a new run), while some went unnoticed. The above method of livetime calculation nicely takes care of those unnoticed situations; the HV-off periods are excluded from the livetime, because no more scintillator muon is produced if the HV is turned off. Summing over all runs having at least one scintillator muon, the total livetime computed this way is 2% less, *i.e.*, 2% closer to the real livetime, than the simple sum of run durations, because run durations include those unnoticed HV-off periods. For all runs passing the livetime cut and the logbook cut discussed below, this reduction in livetime is 0.7% (Fig. 4.1).

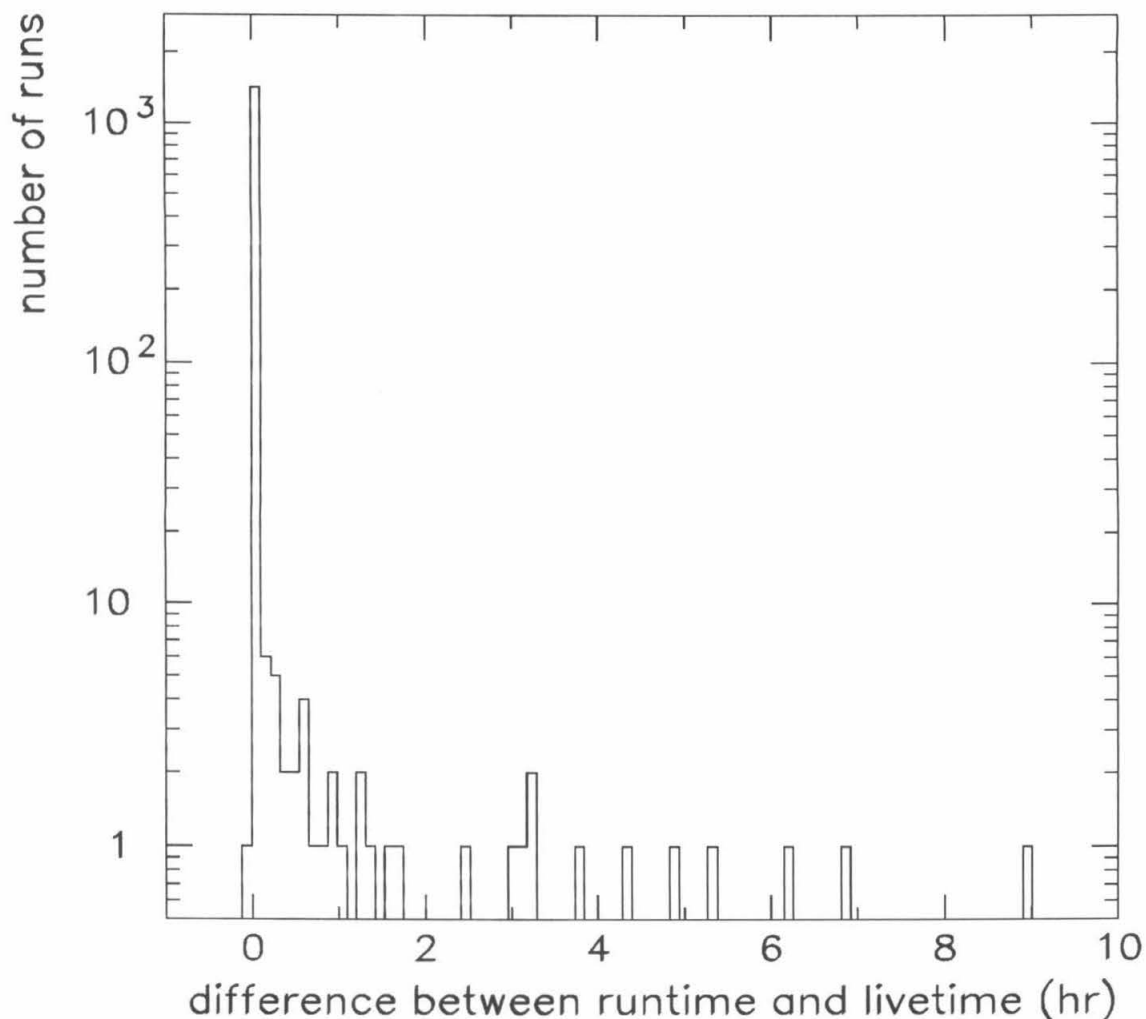


Figure 4.1: Effect of calculating the livetime using scintillator muons. The horizontal axis is the difference between the runtime and the livetime. The runtime is the time difference between the first and the last event in the run, while the livetime is the time difference between the first and the last scintillator muon in the run (not yet corrected for dead time). Normally these two times should agree within ~ 1 minute as shown by the peak at the origin; their differences were caused by the situation when power flickers turned off the high voltage system for the scintillator PMTs while the run continued. This plot is for all runs which passed the livetime cut and the logbook cut.

This livetime is further corrected by the dead time when the computer is busy in processing each incoming event. In a normal run in the first supermodule the event rate is roughly ten events per minute, while the average dead time is about 50 millisecond per event. The dead time is measured online and recorded in the data: A scaler is used to count both a free running 10 Hz clock input and the same clock vetoed by the computer busy signal; their difference yields the dead time. Although the 10 Hz clock may seem slow, it is capable of accurately measuring the dead time statistically since the number of events is large. The dead time averaged over all runs used in this thesis is 0.6% of the livetime.

The livetime distribution for all runs is shown in Fig. 4.2. The peak at the far left is mainly composed of abnormal runs, which tended not to last as long as good runs, since a run was stopped short as soon as a problem was discovered. Many abnormal runs occurred on Tuesdays¹ as the detector was being switched from the calibration mode back to the normal data acquisition mode after the weekly calibration and maintenance. In addition to mistakes associated with human activities (*e.g.*, forgetting to plug back a temporarily unplugged cable), the online data acquisition system hanged some Tuesdays when being switched back to its normal mode. To reject these short abnormal runs, a minimum livetime requirement of two hours is placed to ensure the quality of runs for data analysis. This unbiased cut reduces the total livetime by 2%. There are 1616 runs which meet the minimum two hour livetime requirements and in which at least one of the two monopole triggers was working; the corresponding total livetime is 602 days.

For these 1616 runs, the data taking logbook was consulted to check the run conditions. The runs under abnormal conditions were rejected from further analyses. If only one of the two monopole trigger systems was abnormal in a run, that run was kept at this stage and was cut when the corresponding trigger was analyzed. This logbook cut reduces the livetime by 8% to 552 days. Here are some of the major abnormal conditions causing significant livetime reduction:

¹Tuesday is the weekly calibration and maintenance day.

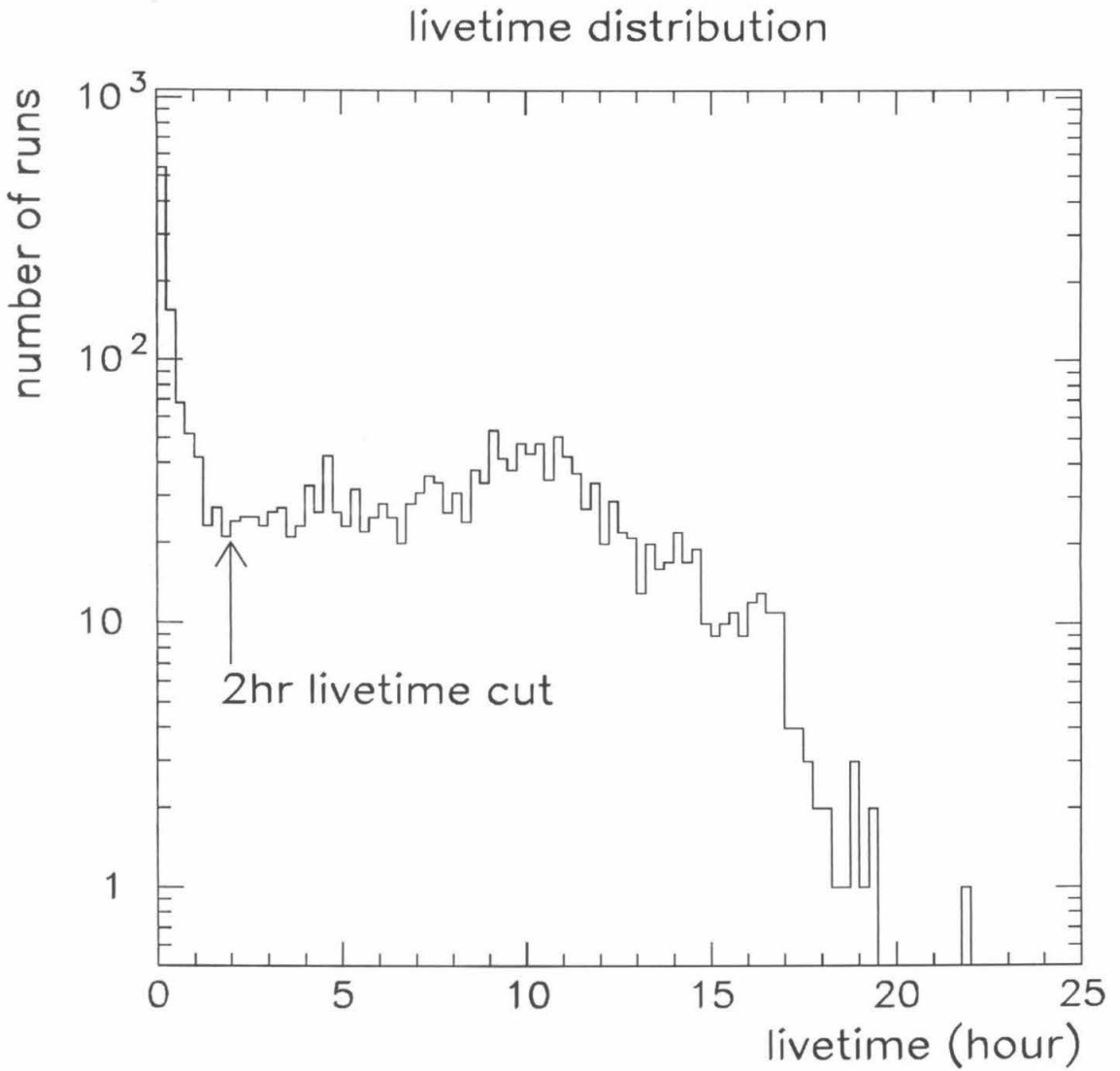


Figure 4.2: Lifetime distribution for all data runs having at least one scintillator muon. A minimum run lifetime requirement of two hours is placed to reject the short and usually abnormal runs for data analysis.

- As described on page 75, the end chambers of the vertical scintillator counters were filled with pure mineral oil during this data run in February 1990. A significant part of the detector was turned off to allow the end chamber filling. Throwing away these runs reduces the livetime by nine days, or 1.5%.
- One crate containing monopole electronics and waveform digitizers lost power for about seven days.
- The fast monopole trigger sometimes gave abnormally high rates because of its extreme sensitivity to environmental noise (page 67). If it occurred when there was no expert around, this trigger got unplugged temporarily. At earlier stages, the cable disconnection was done at an incorrect place and consequently garbage waveform data may have been recorded for other triggers including the slow monopole trigger. Such errors cost about 13 days of livetime. There were more runs in which the fast monopole trigger was unplugged correctly so that the slow monopole trigger was not affected; these runs were deducted only from the livetime of the fast monopole analysis (page 121).
- Other various abnormalities: power glitches causing high voltage supply faults, people doing tests, some electronics broken, etc.

After this logbook cut, the quality of the scintillator data is quite good, as can be seen from the distribution of *normalized scintillator muon rates* (defined below in Eq. 4.2) shown in Fig. 4.3. If the detector behaves ideally, the (unnormalized) scintillator muon rate r in each run follows a Gaussian distribution whose width depends on the run livetime T , namely,

$$g(r; T) = \left(2\pi \frac{\langle r \rangle}{T}\right)^{-1/2} \exp\left(-\frac{(r - \langle r \rangle)^2}{2 \langle r \rangle / T}\right), \quad (4.1)$$

where $\langle r \rangle$ is the mean muon rate. So the rate distribution in all runs is a superposition of many Gaussian distributions of different widths. Fig. 4.2 shows the distribution of the

Distribution of normalized scint muon rate

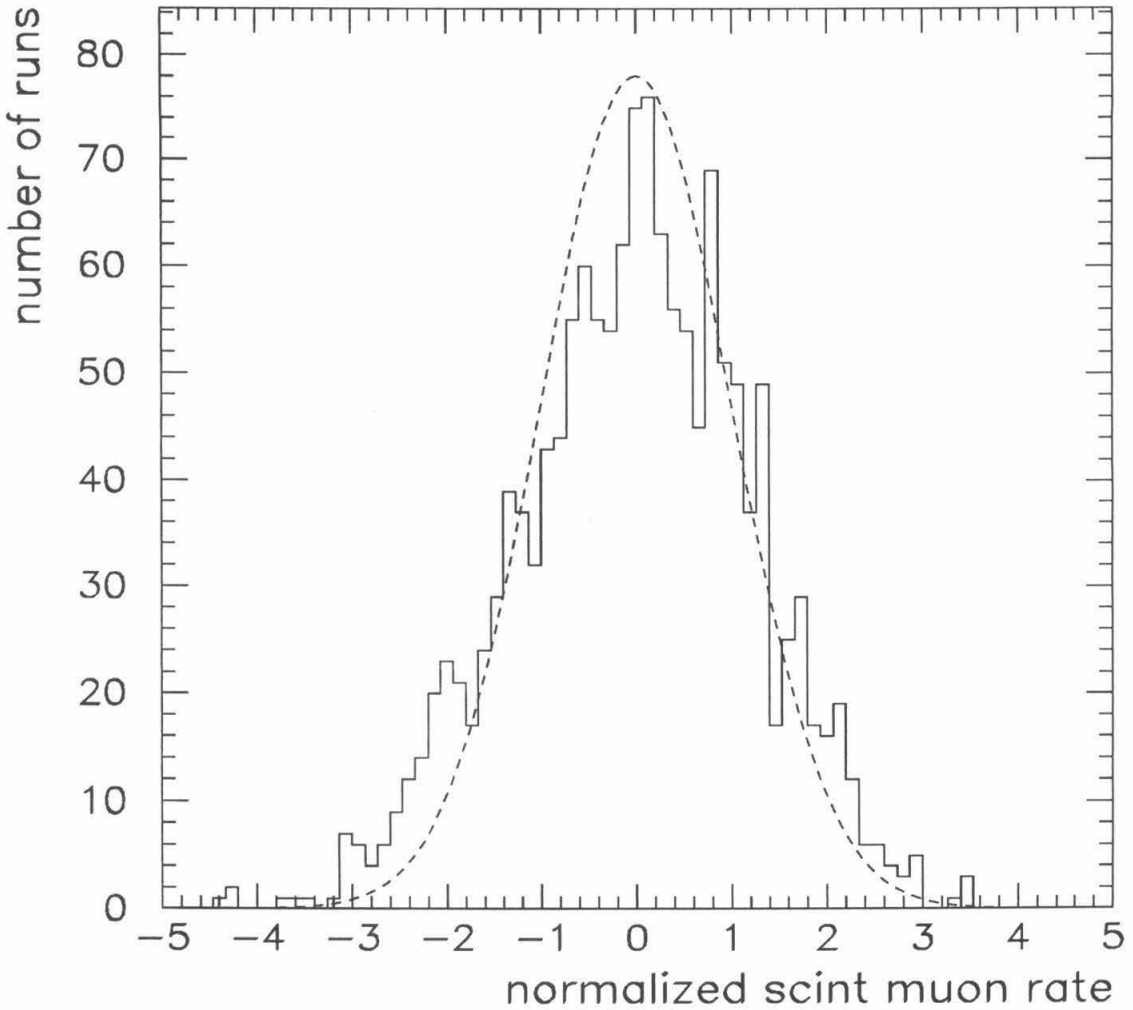


Figure 4.3: Distribution of normalized scintillator muon rates for all runs passing the livetime cut and the logbook cut. This normalized rate is expected to follow a Gaussian distribution with vanishing mean and unit width as shown by the dash curve. The excess in the high tails is caused by the occasional noise firing the trigger, while the excess in the low tails is due to occasional absence of single counters. However, in general the observed distribution agrees with the expected one.

normalized rates,

$$r_n = (r - \langle r \rangle) / \sqrt{\langle r \rangle / T} \quad . \quad (4.2)$$

From Eq. 4.1, this should follow a Gaussian distribution with vanishing mean and unit width, which is also plotted in Fig. 4.3. The observed distribution agrees with the expected one reasonably well.

A summary of the run selections is given in Table 4.1.

Run Selections	Number of Runs	Livetime (days)
scintillator is on	2540	617
at least one of the two monopole triggers is on	2262	615
livetime > 2 hours	1616	602
logbook cut	1467	552

Table 4.1: Run selections. The logbook cut in this table only ensures that at least one of the two monopole triggers was functioning.

4.2 Slow Monopole Analysis

This section describes the analysis of data collected using the slow monopole trigger while the next section will present the fast monopole analysis. Although sharing a common goal to search for monopoles, the fast and the slow monopole trigger systems are very different and quite independent of each other. This fact requires that the two analyses be quite different. So it is necessary to treat them completely separately.

4.2.1 Selection of Candidates

Among the runs which passed the logbook cut in Table 4.1, there are a few indicated by the logbook which are abnormal for the slow monopole trigger while adequate for the fast monopole trigger. After cutting these runs, the livetime is reduced to 548 days. During the 1454 runs finally selected for slow monopole analysis, 594,512 events fired the slow monopole trigger.

These events are then vetoed by a fast muon trigger, the SPAM trigger. As shown in Fig. 3.10 on page 65, the SPAM trigger requires time of flight between different faces shorter than $1 \mu\text{s}$, and so it selects only particles with velocity $\beta > 0.015$. Hence it is legitimate to use the SPAM trigger to veto the slow monopole trigger events, since the slow monopole trigger is sensitive to particles with velocity $\beta < 3 \times 10^{-3}$. This veto reduces the number of events to 552,430. The effect of this veto is relatively small (8%) because it was implemented in hardware for the second year (since November 1990) of this two year data taking. Furthermore, the trigger rate in the second year was much higher than in the first year, since the trigger parameters were changed to improve monopole sensitivity in November 1990, as described on page 75.

The slow monopole trigger is a single counter trigger and the majority of the slow monopole trigger events are single face events. As an example, the waveforms of the first few slow monopole events from an arbitrarily chosen run are shown in Fig. 4.4. Specializing in selecting wide pulses and long pulse trains, the slow monopole trigger legitimately picked up these pulse trains, which can apparently be attributed to radioactivity pileups — many background radioactivity pulses accidentally occurring within a short time interval.

To pursue redundancy and clear signatures as a general philosophy of a search for rare events, we require the two face coincidence, which leaves us 1260 candidates. Fig 4.5 shows a distribution of the run numbers and the relative times of these candidates. There are two outstanding bursts: run 2911 contains a burst of 130 two face events which occurred

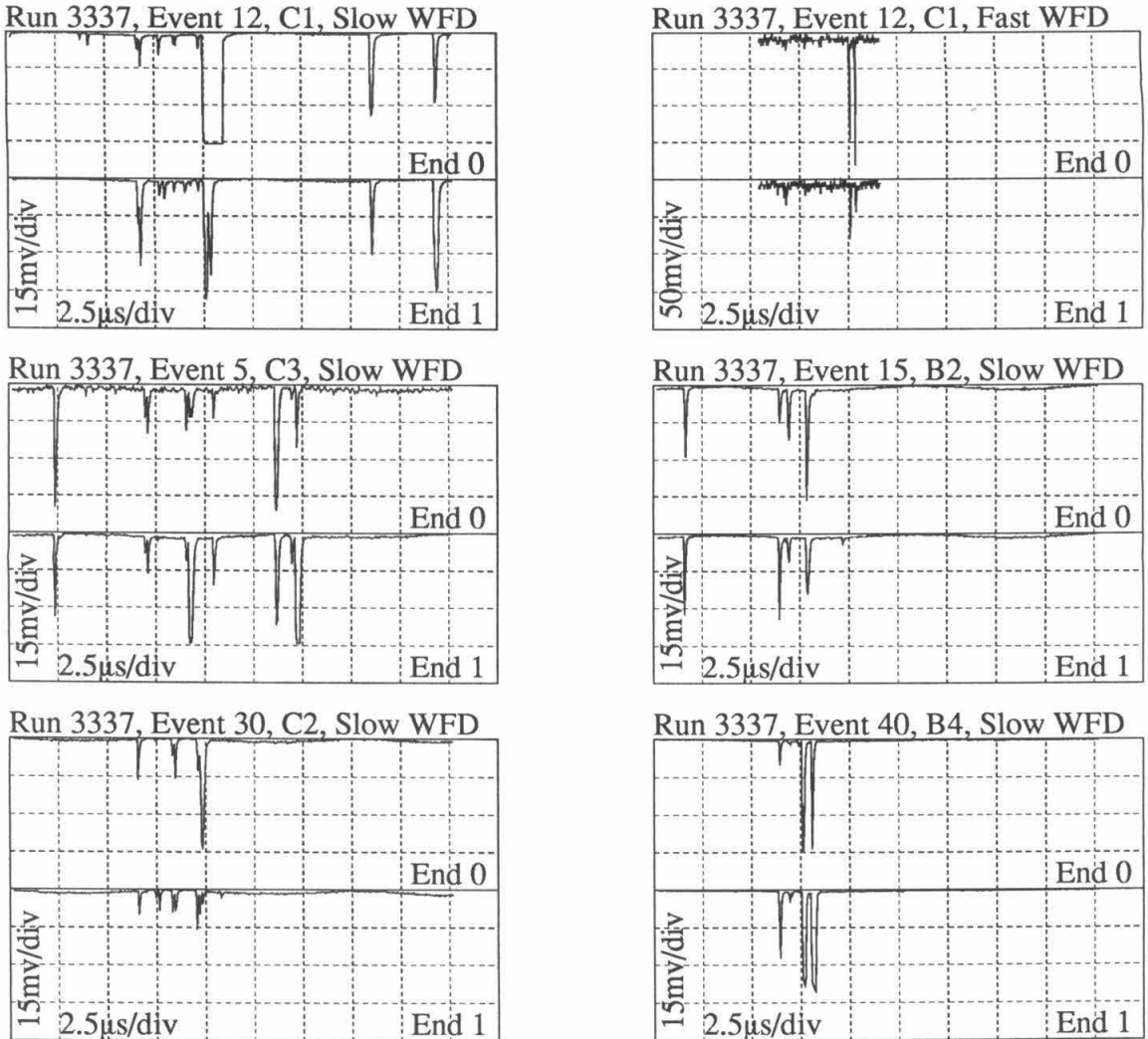


Figure 4.4: Sample waveforms of five randomly chosen single face slow monopole trigger events. The signals were multiplexed as shown in Table 3.1. all waveforms except the upper right one were recorded by the slow WFDs (waveform digitizers), while the upper right one, showing the same event as the upper left one, were recorded by the fast WFDs (Table 3.2). The WFDs were configured as in Fig. 3.11.C. A single photoelectron pulse height of around 3 mV would be about one fifth of a division in the slow WFD graphs, and invisible in the fast WFD graph. The “apparently large wide” pulse in the upper left plot saturated the slow WFD and was widened by the pulse shaper; the fast WFD, configured to handle large pulses, shows that it actually consists of two well-separated sharp pulses. The time window of the fast WFD is 6.4 μ s long while the slow one is 22.75 μ s long.

1260 two face slow monopole events

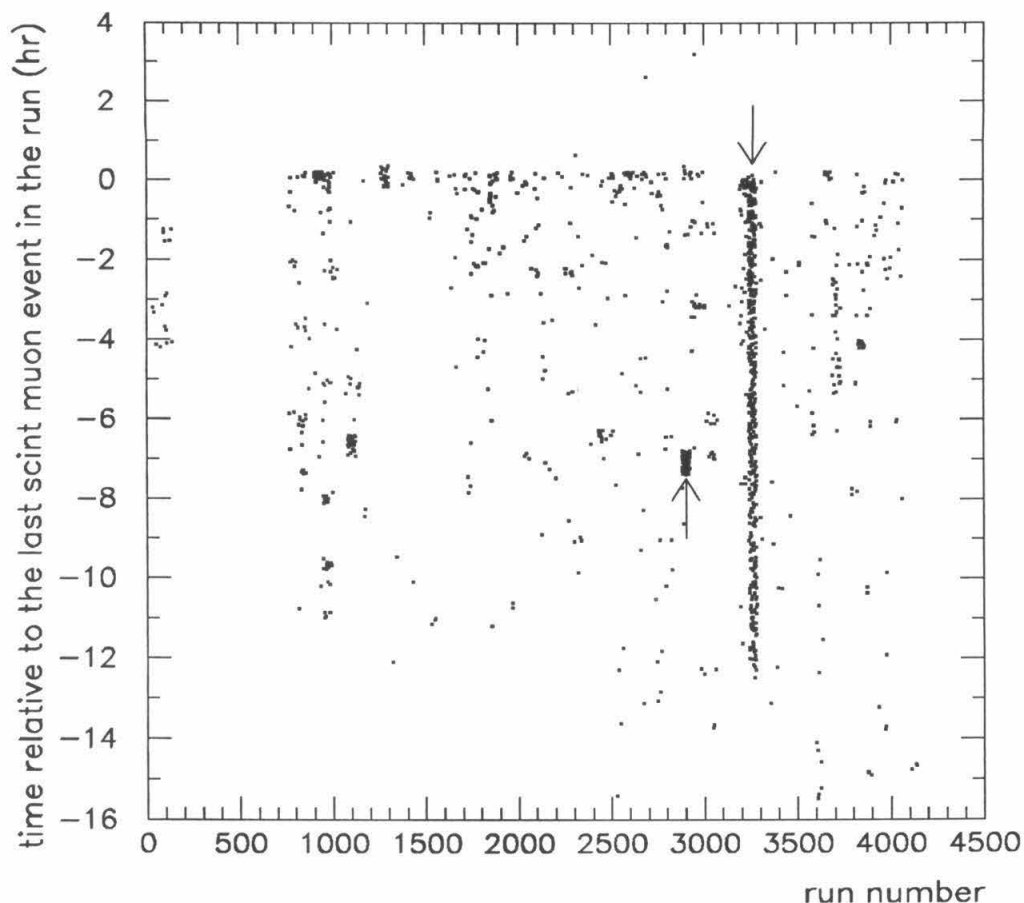


Figure 4.5: The distribution of the run numbers and relative times of the 1260 two face slow monopole events. The run number of this data set starts from 784; a few runs whose data were taken using a backup computer were assigned with run numbers starting from 80001; their run numbers, modulo 80000, were plotted. The vertical axis is the time relative to the last scintillator muon event in the run, which shows the candidates' relative time in a run and will be explained further later in Fig. 4.8. The bin sizes are 45 runs by 0.2 hours and the dots are randomized within a bin. The arrows point to two bursts: one in run 2911 and another in runs 3245-3255, both of which were studied with the possibility of monopole bursts in mind.

within half an hour; runs 3245-3255 contain another burst of 407 events almost uniformly spread over a period of 4.5 days. To check against the possibility of monopole bursts, 10% of the candidates from these two bursts were randomly selected and their waveforms were visually scanned. The waveforms of 15 randomly selected candidates out of the 130 in run 2911 were scanned, and they all looked like the event shown in Fig. 4.6: the noise of the shown type appeared in all supercounters (for their nomenclature, see Table 3.1) of the bottom and center faces and fired the slow monopole trigger in every channel in these two faces. Among the 407 candidates in runs 3245-3255, 33 candidates (three per run) were arbitrarily chosen, and visual scanning revealed that their waveforms all looked like the event shown in Fig. 4.7: clear bipolar oscillations in every channel. Thus, we can safely assert that these two bursts are definitely not monopole bursts and discard these runs in further slow monopole analysis. This reduces the livetime by 1% to 542 days and number of candidates to 723. Other bursts not so outstanding as these two bursts are accepted as candidates to be further analyzed, making this analysis conservative against the possibility of a monopole burst.

For the surviving candidates, the distribution of their times with respect to the last scintillator muon event in the run is shown in Fig. 4.8, which is actually a projection of Fig. 4.5 (minus those events in the two discarded bursts). The outstanding peak around the origin is caused by power glitches, which turned off the high voltage system for the scintillator PMTs and thus defined the timing of the last scintillator muon in the run. The transient electrical noise accompanying the power glitches triggers the slow monopole circuit. After the high voltage is turned off, there are no more scintillator muons, but there may still be more electrical noise, such as another power glitch, firing the slow monopole trigger. That explains the events with positive time in the plot. To reject these near-end-of-run events induced by power glitches, a cut is placed to require candidates to occur 0.015 hour (54 seconds) earlier than the last scintillator muon. Since in total 1442 runs are used in the slow monopole analysis, this end-of-run cut reduces the livetime by 22 hours.

Run 2911, Event 12218, Slow WFD
Scales: horizontal=2mv/div, vertical=2.5 μ s/div



Figure 4.6: A randomly selected two face slow monopole event from run 2911, which contains a burst of 130 candidates.

Run 3245, Event 6144, Slow WFD
Scales: horizontal=3mv/div, vertical=2.5 μ s/div

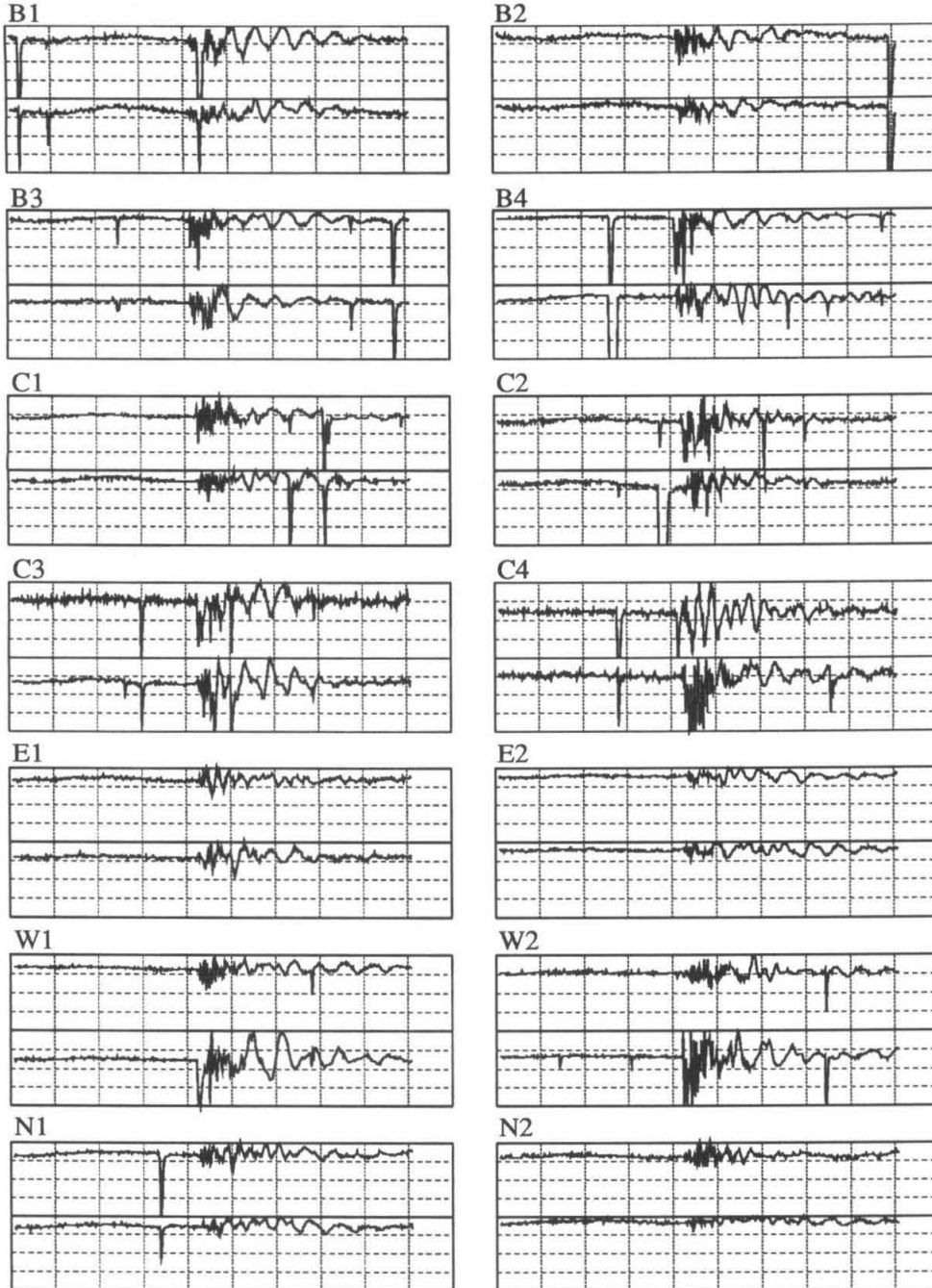


Figure 4.7: A randomly selected two face slow monopole event from runs 3245-3255.

723 two face slow monopole events

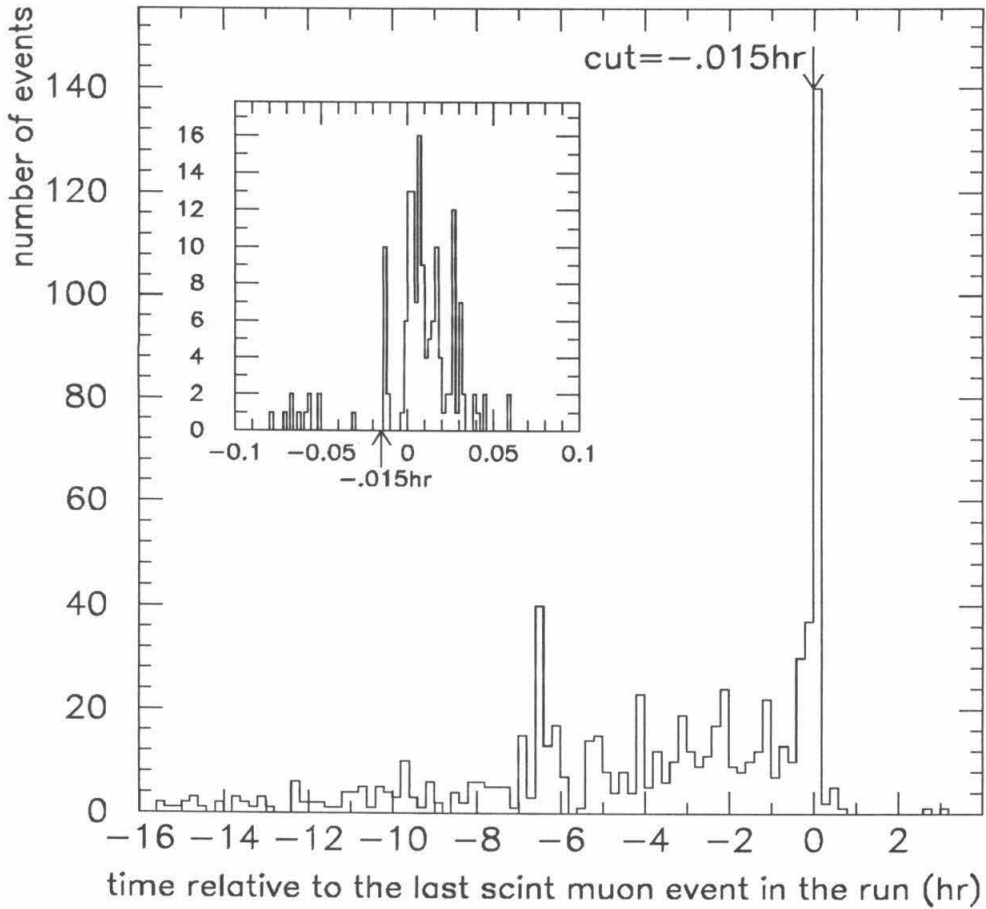


Figure 4.8: The distribution of the times at which the candidates occurred relative to the last scintillator muon event in the run. It is a projection of Fig. 4.5 excluding run 2911 and runs 3245-3255. The plot in the upper left corner is a blow-up around the origin, showing the detail of the outstanding peak there.

The final livetime for the slow monopole analysis is thus 541 days or 4.7×10^7 seconds. This end-of-run cut, the final cut prior to detailed study, leaves us 573 candidates.

Cuts	Livetime (days)	Number of Candidates
from Table 4.1	552	—
logbook cut for SMT	548	594,512
discard runs 2911, 3245-3255	542	583,999
fast muon veto (SPAM veto)	542	541,918
two face coincidence	542	723
end of run cut	541	573

Table 4.2: Summary of cuts for slow monopole analysis.

Table 4.2 shows a summary of all cuts for slow monopole analysis. While the cuts are described in the chronological order in the preceding paragraphs, they are given in a more logical order in the said table – the discarding of runs 2911 and 3245-3255 is listed prior to the fast muon veto and two face coincidence requirement, and so the first two entries in the table cut out whole runs.

Fig 4.9 shows a distribution of the run numbers and the relative times of the finally selected candidates. The candidates are uniformly distributed in a very crude way, and there are a few bursts which are accepted as candidates in case of a possible burst of *real* monopoles, as said before. The effect of these bursts on the dead time is negligible because each burst typically lasts less than a couple of minutes. Assuming that all these monopole candidates are randomly and uniformly distributed and assuming that the run livetime distribution is flat, which is crudely true in the range of livetime from two hours to 15 hours as shown in Fig. 4.2, we can deduce that the candidates' time with respect to the

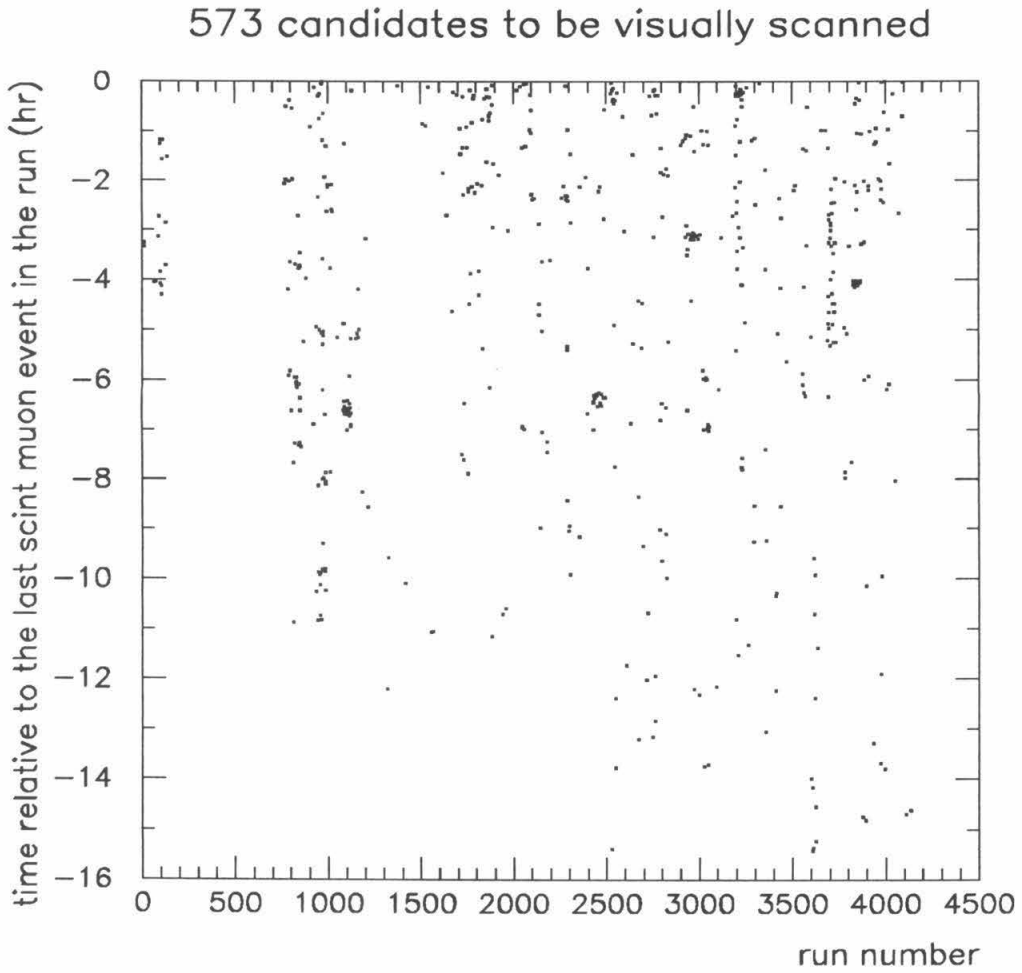


Figure 4.9: The distribution of the run numbers and relative times of the finally selected slow monopole candidates. This is a similar plot to Fig. 4.5, but the entries here are only a subset of those in Fig. 4.5.

last muon in the run follows a *linear* distribution. This deduction is a first approximation to the observed distribution shown in Fig. 4.10, which is a projection of Fig. 4.9 on the axis of the relative time.

4.2.2 Visual Scanning of Candidates

The waveforms of all 573 candidate events were visually scanned. It was found that 565 events were caused by electrical noise and the remaining eight events were of non-electrical origin.

Among the 565 events of electrical noise, 388 events clearly display bipolar oscillations in either the slow waveform or the fast waveform or both, an example of which is shown in Fig. 4.11. Signals from phototubes are always negative-going. Thus this bipolar feature definitely identifies these events as electrical noise. The possible sources for the electrical noise are radio-frequency pick-up and power line noise. Another eight events show negative-going pulse trains of durations longer than $4 \mu s$ (Fig. 4.12), but these pulse trains are simultaneously present in all channels. Hence they must have been produced by electrical sources, because if they had been generated by traversing monopoles or showers of monopoles, the long durations of the pulse trains would determine the velocities of the monopoles to be very slow, conflicting with the fact of simultaneous presence of these pulse trains in all channels. One may question in general the possibility of this kind of electrical noise confusing us if it occurs only in two channels and with correct timing, thus undermining our ability to differentiate a true monopole from this kind of electrical noise. We argue that this possibility can be excluded, because it is quite unlikely for the electrical noise to affect only two channels, and even if the unlikely happens, the electrical noise would affect these two channels at the same time, thus making the time of flight inconsistent with the pulse train duration. The other 169 events show only baselines and occasional radioactivities (Fig. 4.13). No appreciable feature in the waveform indicates how these events could have fired the slow monopole trigger. These events are interpreted as having

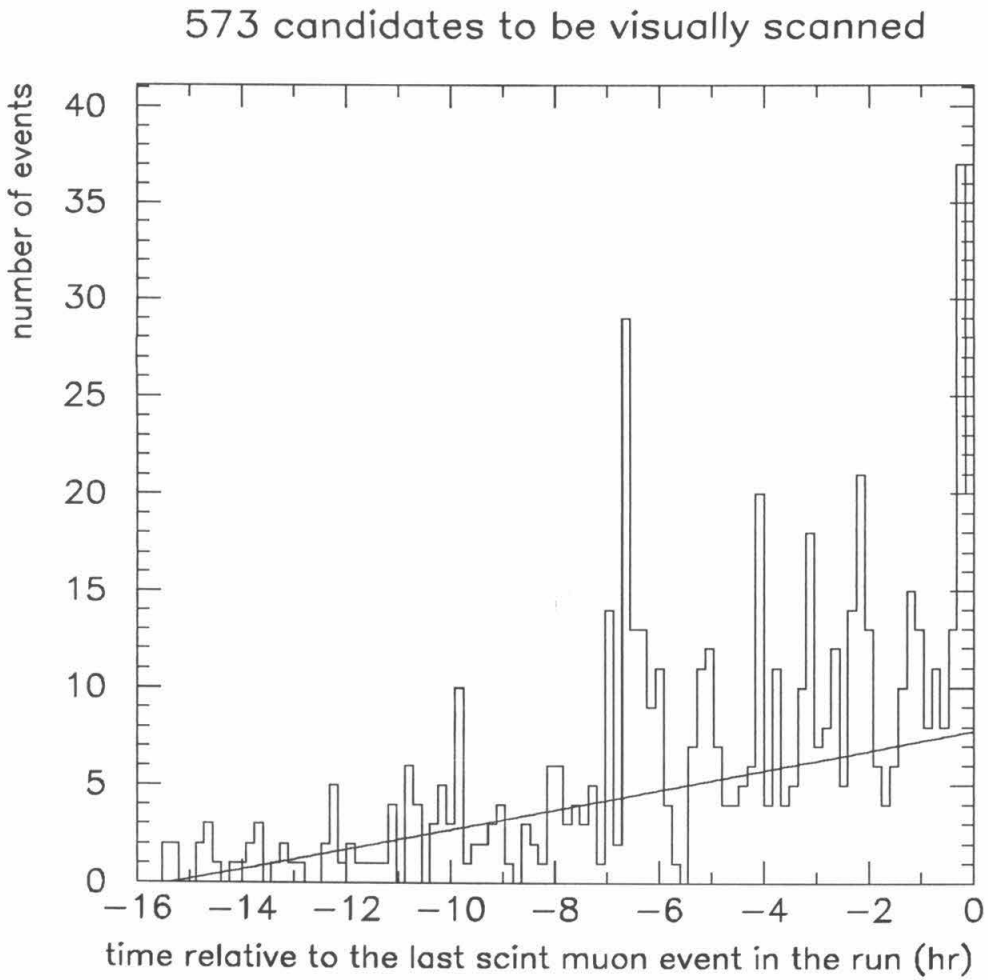


Figure 4.10: The distribution of the relative times of the final selected slow monopole candidates. The line drawn is just a simple linear fit (page 105) to the histogram.

Run 3205, Event 641, Slow WFD
Scales: horizontal=3mv/div, vertical=2.5 μ s/div

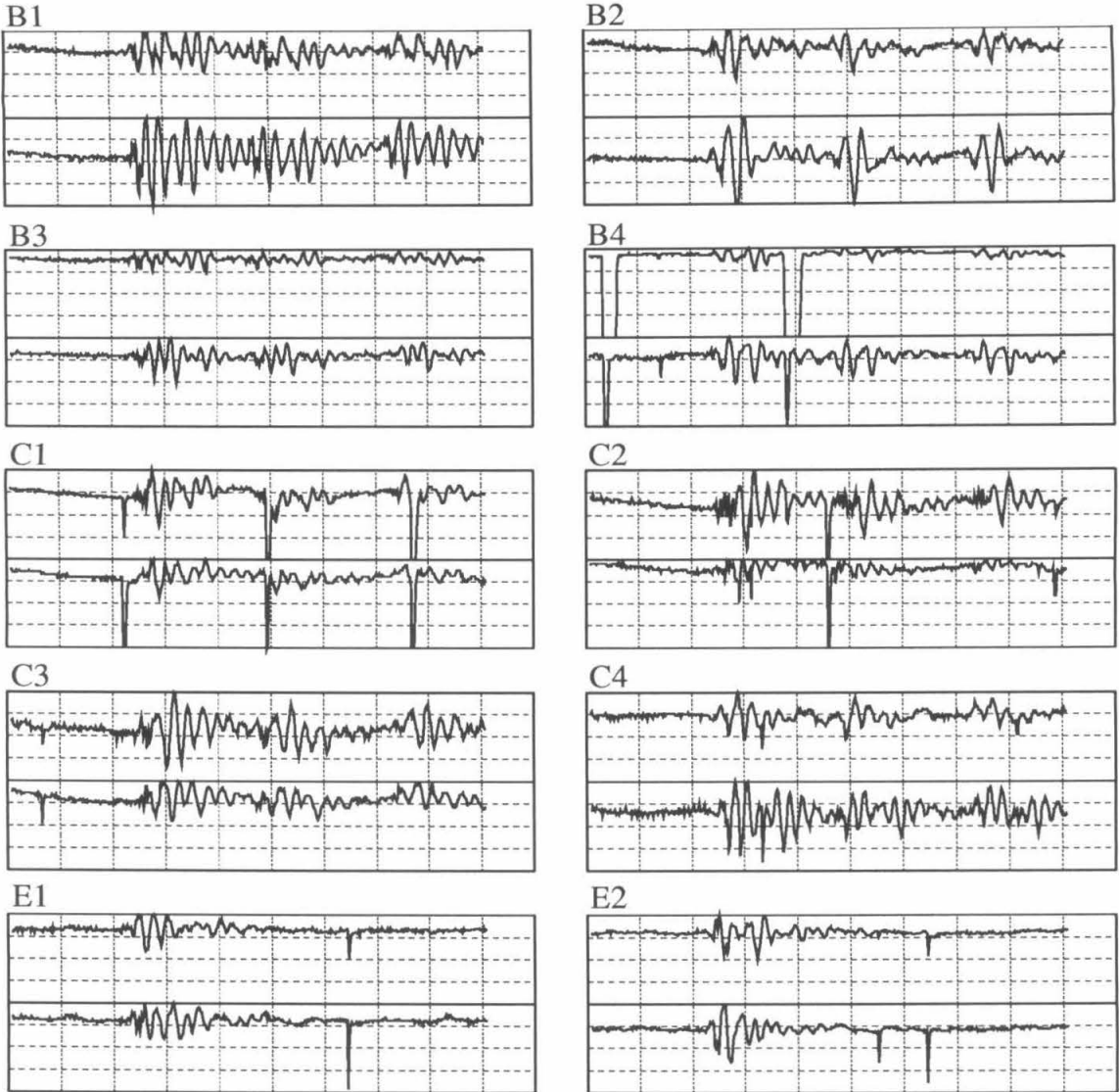


Figure 4.11: An example of an event with bi-polar oscillations. For this particular event, the slow monopole trigger for the West and North faces were not fired so the corresponding waveforms were not recorded. The “apparent large wide” pulses in B4 are produced by radioactivities (see the caption of Fig. 4.4 and of Fig. 4.15).

Run 2834, Event 1937, Slow WFD
Scales: horizontal=6mv/div, vertical=2.5 μ s/div

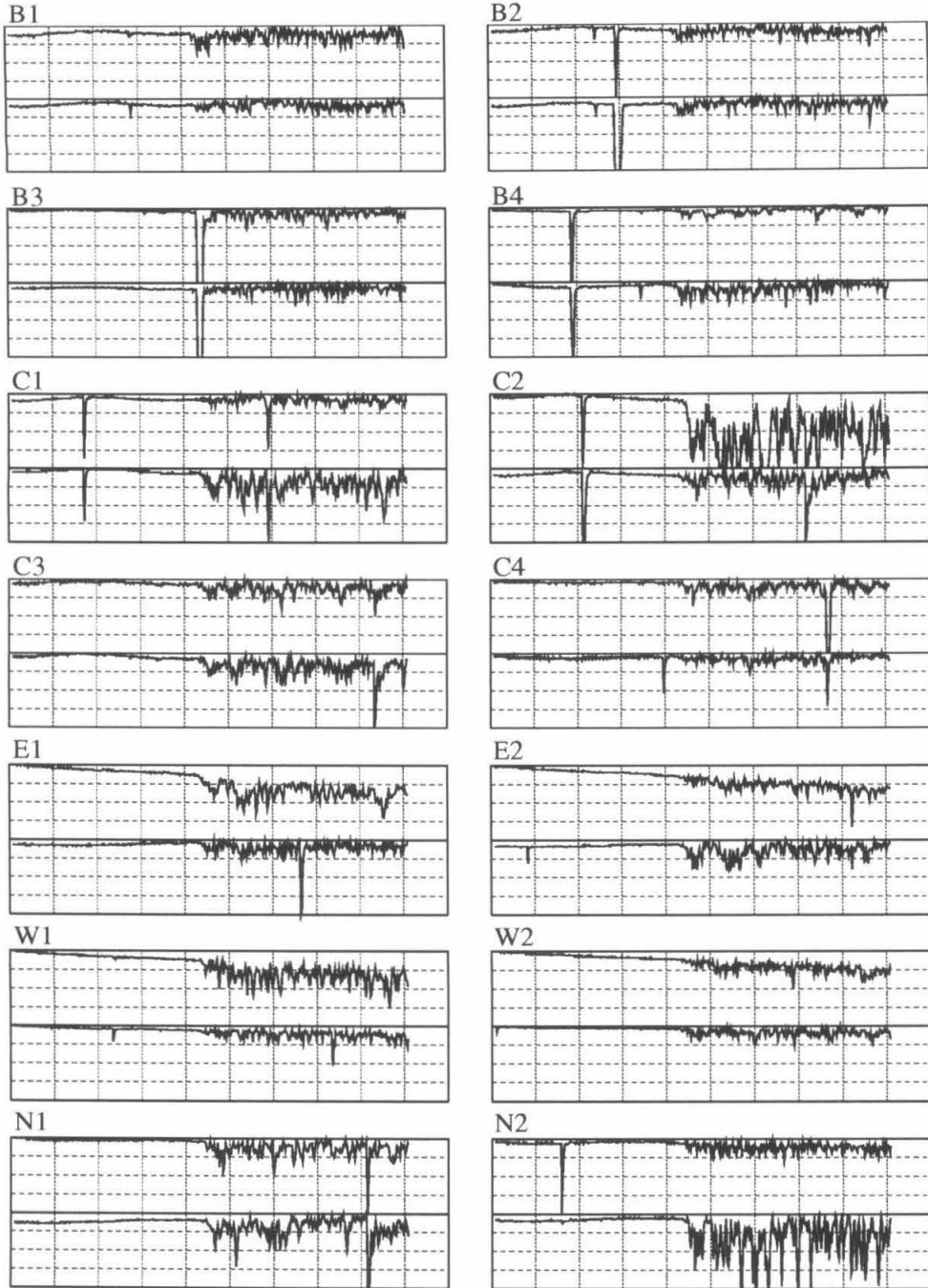


Figure 4.12: An example of an event with simultaneous presence of long negative pulse trains in all channels.

Run 1877, Event 6703, Slow WFD
Scales: horizontal=1mv/div, vertical=2.5 μ s/div

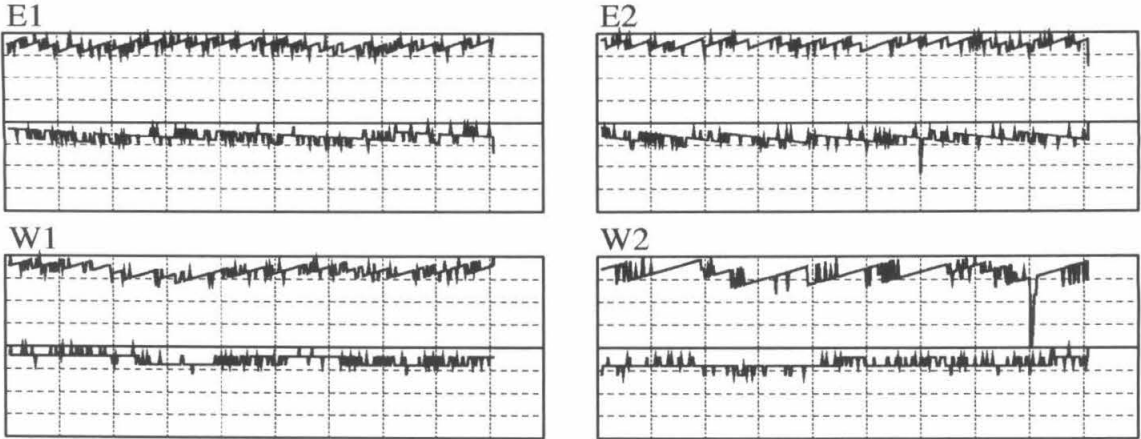


Figure 4.13: An example of an event with featureless waveforms.

been caused by electrical noise, such as power-line fluctuations, which is picked up at the trigger circuits but not picked up by the WFDs (the inputs to the slow monopole trigger circuits went through different paths from the WFD inputs). This type of featureless waveforms occur quite frequently among those events which are identified as power flicker-induced by other means, *e.g.*, those events which do not survive the end-of-run cut (page 99) — an indication that power flickers or power-line fluctuations are fully capable of producing this kind of event.

The remaining eight events are of non-electrical origins, and so more interesting. Their waveforms are like those of PMT signals (rather than electrical noise) in both faces where the slow monopole triggers (SMTs) fired, that is, the two faces through which the possible monopole enters and exits the MACRO detector.

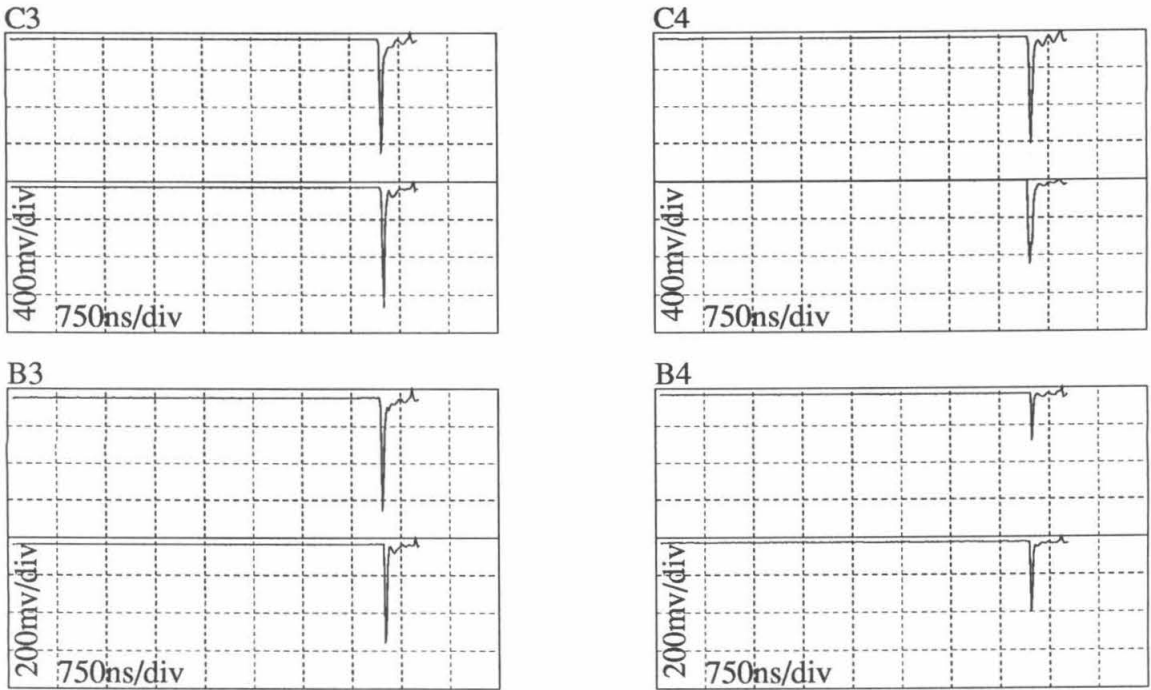
Among these eight events, two events are easily identified as muons, according to their time of flight and pulse shapes. The streamer tube tracking system (section 2.2.2) also confirms them as muons. These two events occurred in runs when the SPAM muon trigger

encountered problems (bad cables); thus they were not rejected by the SPAM muon veto. This SPAM failure does not affect the sensitivity of the monopole detection (its only effect is that we have two extra candidates to scan), hence the runs in which the SPAM failed were not removed from the analysis, and thus not from the accumulated livetime. One of these two events is shown in Fig. 4.14. This event occurred when the fast WFDs were configured to take dynode signals as their inputs (Fig. 3.11). However, all other waveforms shown as examples in this thesis have anode signals as their inputs. Both the fast waveforms and the streamer tube signals are consistent with the passage of a di-muon accompanied by showers. The streamer tubes are only used as a confirmation to reject these events as muons instead of a required tool in this analysis, so they are not discussed in detail in this chapter.

Three other events are accidental coincidences of muons firing the SMT in one face and pileups of radioactivities firing the SMT in another face. One of these events is shown in Fig. 4.15. While the center face shows a very large sharp pulse (consistent with a muon), the bottom face is a collection of smaller shape pulses (consistent with a radioactivity pileup). One may argue that the collection of short pulses in the bottom face is a long pulse train, a signature of a slow traversing particle. But this long pulse train in the bottom face immediately conflicts with the short, sharp pulse in the center face.

Finally, the last three candidates are accidental coincidences of radioactivity pileups firing the SMT in both faces. They are our *best* candidates because only these three candidates have waveforms of negative-going wide pulses or pulse trains in two different faces, expected from the passage of a slow monopole through the MACRO detector. The waveforms of these three events are shown in Figs. 4.16-4.18. Their waveforms, especially the fast waveforms (whose input signals did not go through a pulse shaper as did the input signals of the Slow WFDs), clearly show that each signal is a superposition of several sharp spikes, characteristic of a radioactivity pileup. The pulse heights indicate that each spike contains several photoelectrons, while the photoelectrons from the passage of a slow

Run 2270, Event 4180 Fast WFD (input is dynode)



Streamer Tubes, Wire View only

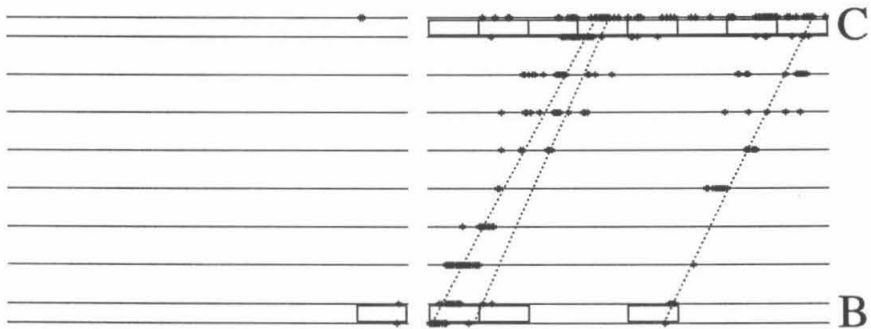


Figure 4.14: A slow monopole candidate faked by a di-muon accompanied by showers. For simplicity, we only show the streamer tube wire view, in which a dot indicates a hit wire, a box indicates a fired scintillator counter and the dashes are best-fit muon tracks. The middle track apparently has been faked by accompanying showers.

Run 3427, Event 2847

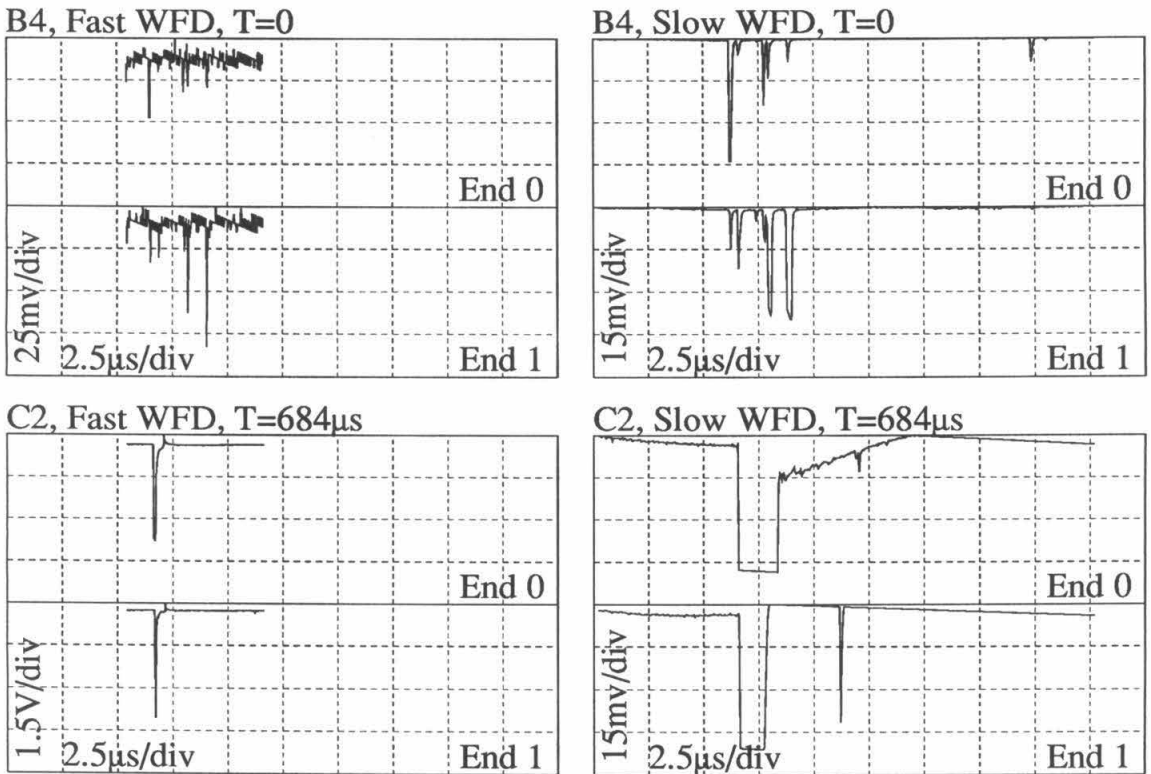


Figure 4.15: Accidental coincidence between a muon in the center face and a radioactivity pileup in the bottom face. As mentioned in the caption of Fig. 4.4, the “apparently wide” pulse in the slow waveform for C2 is widened by the pulse shaper and the saturation of the slow WFD — the full scale of the 8-bit slow WFD is about 200 mV, corresponding to about 40 mV at phototube after taking account of the amplifier and the pulse shaper.

Run 2752, Event 1422

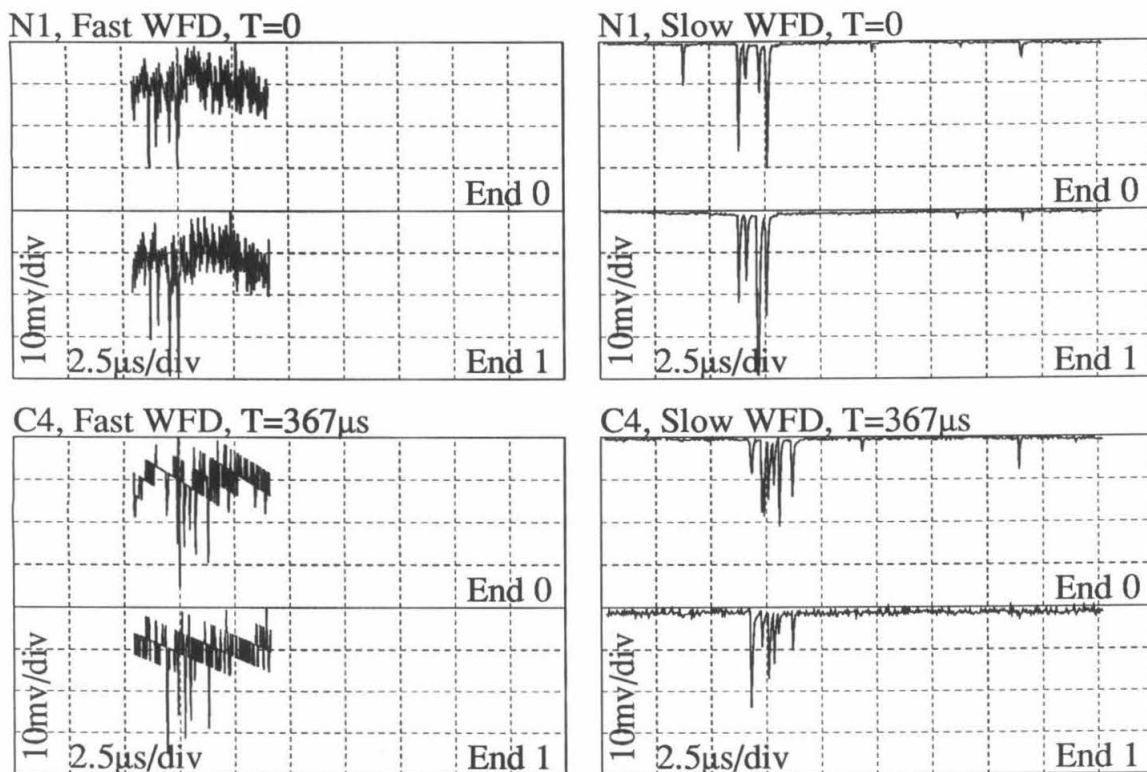


Figure 4.16: Accidental coincidence of radioactivity pileups (I). The average single photoelectron pulse height is 3 mV, one third of a division in the plots, and thus the waveforms are too spiky to be consistent with a continuous light source (*e.g.*, the passage of a slow particle). Nevertheless, it is the *best* slow monopole candidate because the waveforms are the least spiky. If we assume that this event is due to the passage of a particle, its time of flight is 367 μs and its distance of flight could range from 10.5 m to 17.2 m due to the uncertainty in the hit positions in the supercounters N1 and C4, giving a velocity in the range $(0.95-1.56) \times 10^{-4}c$. Assuming this velocity range, the pulse train duration in each supercounter gives the pathlength through that supercounter: for N1, the duration is 1.4 μs, so the pathlength is (4.0-6.6) cm; for C4, the duration is 1.9 μs, so the pathlength is (5.4-8.9) cm. For comparison, if we assume no corner-clipping, the minimum pathlength through N1 is 21 cm, and C4, 52 cm. Monte Carlo simulations give that the acceptance requiring that the pathlengths in both hit faces be greater than 15 cm is 870 m²sr (section 4.4), and the acceptance requiring that the pathlengths in both faces be less than 10 cm is 3.2 m²sr, so the probability to have such a corner-clipping event is reasonably small (0.4%).

Run 2974, Event 10702

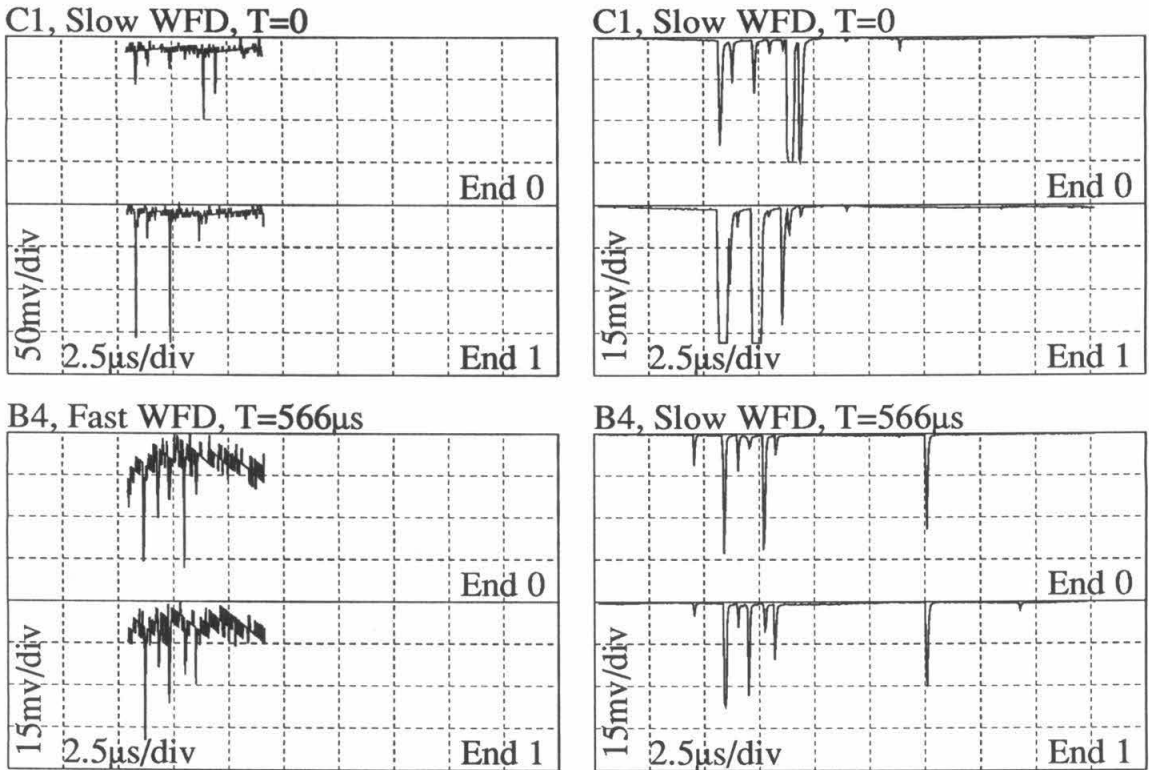


Figure 4.17: Accidental coincidence of radioactivity pileups (II). The average single photoelectron pulse height (3 mV) is one fifth of a division in the plots, except the top left plot where 3 mV is almost invisible. See the caption of Fig. 4.15 for an explanation of the “apparent wide” pulse in the top right plot. The waveforms are more spiky (or less “monopole like”) than those in Fig. 4.16. For this event, the time of flight is 566 μ s and the distance of flight could range from 8.4 m to 17.3 m, so the possible velocity range is $(0.49-1.02) \times 10^{-4}c$. For supercounter C1, the pulse train duration is 3.8 μ s, giving the pathlength in the range of (5.6-11.6) cm; for B4, the duration is 3.7 μ s, giving the pathlength as (5.4-11.3) cm. For comparison, the minimum pathlength for non-corner-clipping trajectories is 35 cm for both supercounters. The acceptance requiring that the pathlengths be less than 15 cm in both hit faces is 7.9 m^2sr (0.9%).

Run 2662, Event 5018

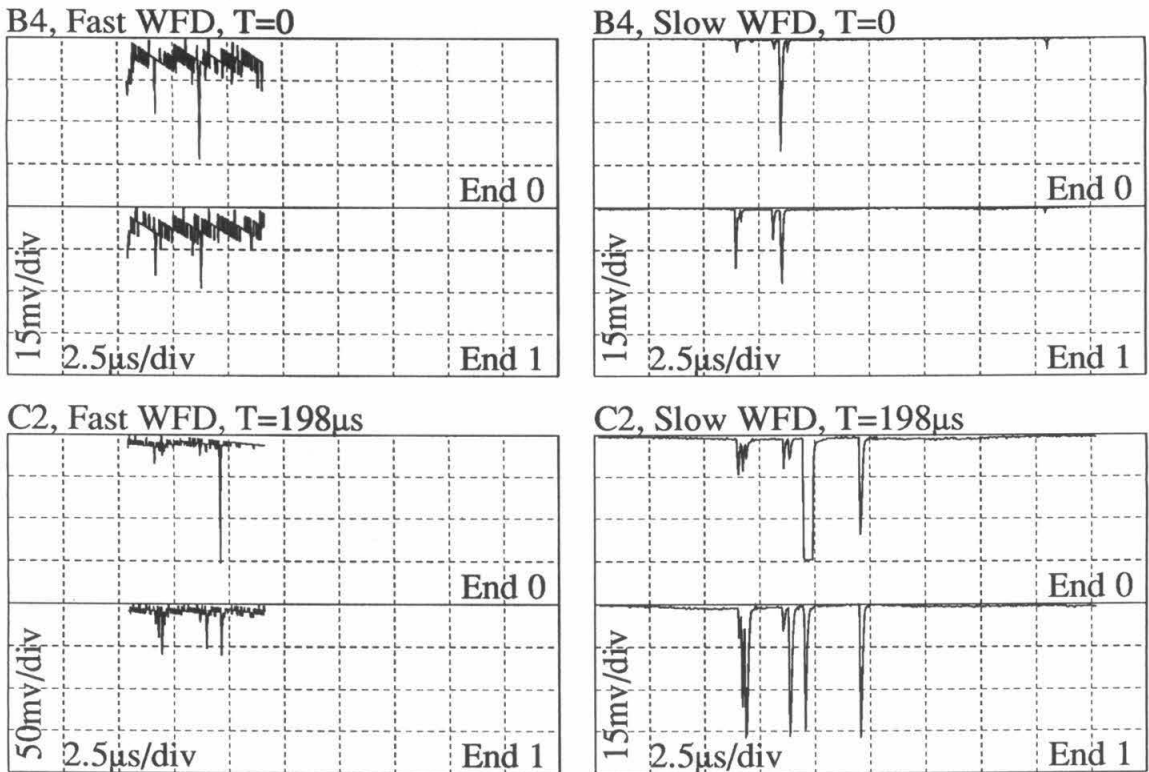


Figure 4.18: Accidental coincidence of radioactivity pileups (III). The average single photoelectron pulse height (3 mV) is one fifth of a division in the plots, except the bottom left plot where 3 mV is almost invisible. See the caption of Fig. 4.15 for an explanation of the “apparent wide” pulse in the bottom right plot. The waveforms are the most spiky (or the least “monopole like”) among the three radioactivity pileup events. For this event, the time of flight is 198 μs and the distance of flight is (6.0-15.5) m, and thus the possible velocity is $(1.0-2.6) \times 10^{-4}c$. For supercounter B4, the pulse train duration is 2.1 μs, giving the pathlength as (6.3-16) cm; for C2, the duration is 5.5 μs, giving the pathlength as (17-43) cm. The minimum pathlength for non-corner-clipping trajectories is 25 cm for both supercounters. So this event requires corner-clipping in at least one face.

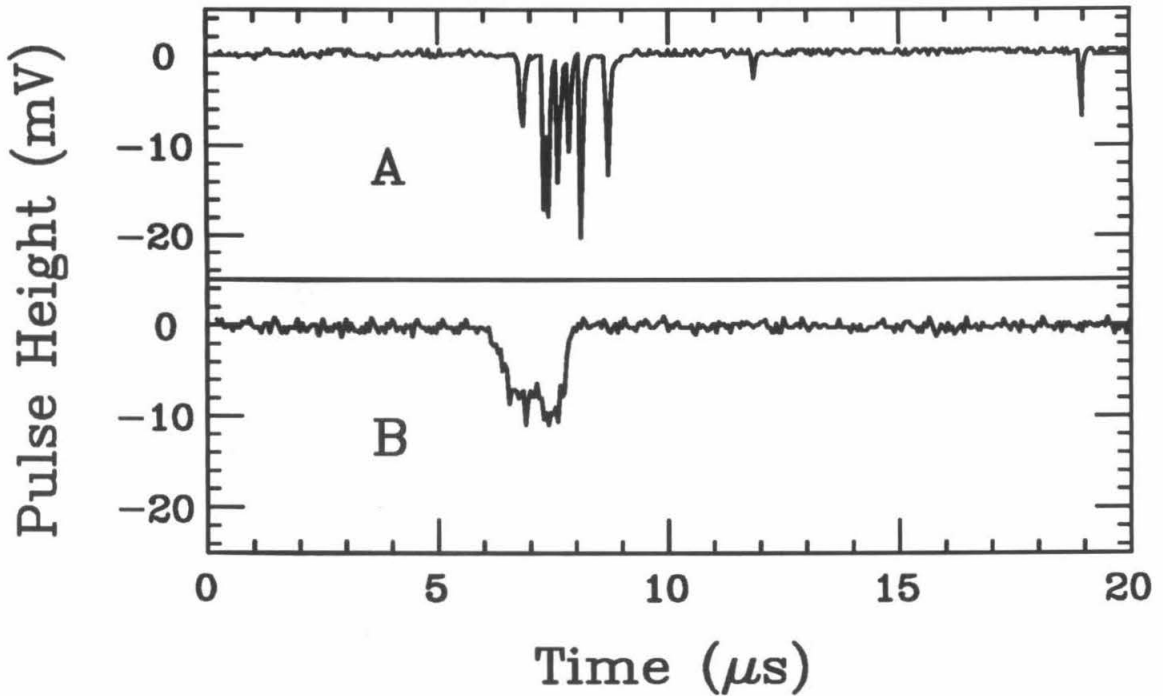


Figure 4.19: (A) The *best* (least spiky) waveform among the slow particle candidates. (B) Waveform of an LED pulse of approximately the same width and area.

particle or any other continuous light source (*e.g.*, an LED) are uniformly and randomly distributed. Hence, these waveforms are all too spiky to be consistent with the passage of a slow particle. Among these waveforms, the slow waveform of end 0, supercounter C4, event 1422 in run 2752 (Fig. 4.16) is the least spiky one, and thus best resembles the signature of a slow traversing particle. For comparison, this best-looking waveform is re-plotted in Fig. 4.19(A) along with an LED simulated waveform of approximately the same width and area shown in (B). This LED pulse is much smoother and the small fluctuations are consistent with the photoelectron statistics. Furthermore, streamer tube signals were absent for these three events as one would expect of radioactivity pileups in the scintillator counters. Assuming these events are due to passages of slow particles, corner-clipping

trajectories are required to reconcile the time of flight between supercounters and the time of passage through each supercounter, as discussed in the captions of Figs. 4.16-4.18. Thus, we conclude that these events are not due to with passages of slow particles, and they are consistent with the radioactivity pileups. We studied the positions where the radioactivities occurred along the counter and found that the positions are randomly and uniformly distributed along the counter within errors, as expected of radioactivity pulses (Fig. 4.20).

Since we have contended that these three candidates are radioactivity pileups, they ought to be randomly and uniformly distributed in time. Noting that they occurred on November 25, December 20, 1990 and February 25, 1991, one may question the statistical probability for them to have occurred within a period of three months while the data were collected over a period of two years. Firstly we argue that it is easy to understand that they all occurred in the second year: in early November 1990 the parameters in the trigger circuits were changed to improve the sensitivity (*cf.* page 75); the trigger circuits were not sensitive enough to pick up this kind of radioactivity pileups in the first year, while in the second year they were. Secondly let us consider only the second year and compute the statistical probability for the three events to occur within three months in the second year. For N random numbers uniformly distributed between zero and one, the probability for the difference between the largest and the smallest number to be less than α ($0 \leq \alpha \leq 1$) is

$$\mathcal{P} = N\alpha^{N-1} - (N-1)\alpha^N. \quad (4.3)$$

In our case, $N = 3$ and $\alpha = 1/4$, therefore the probability is $\mathcal{P} = 5/32 = 15.6\%$. Thus, we conclude that it is not unlikely to observe three events of radioactivity pileups to occur within three months.

In summary, no evidence is found for the passage through the MACRO detector of any slow-moving, light-yielding particle in the data collected using the slow monopole trigger.

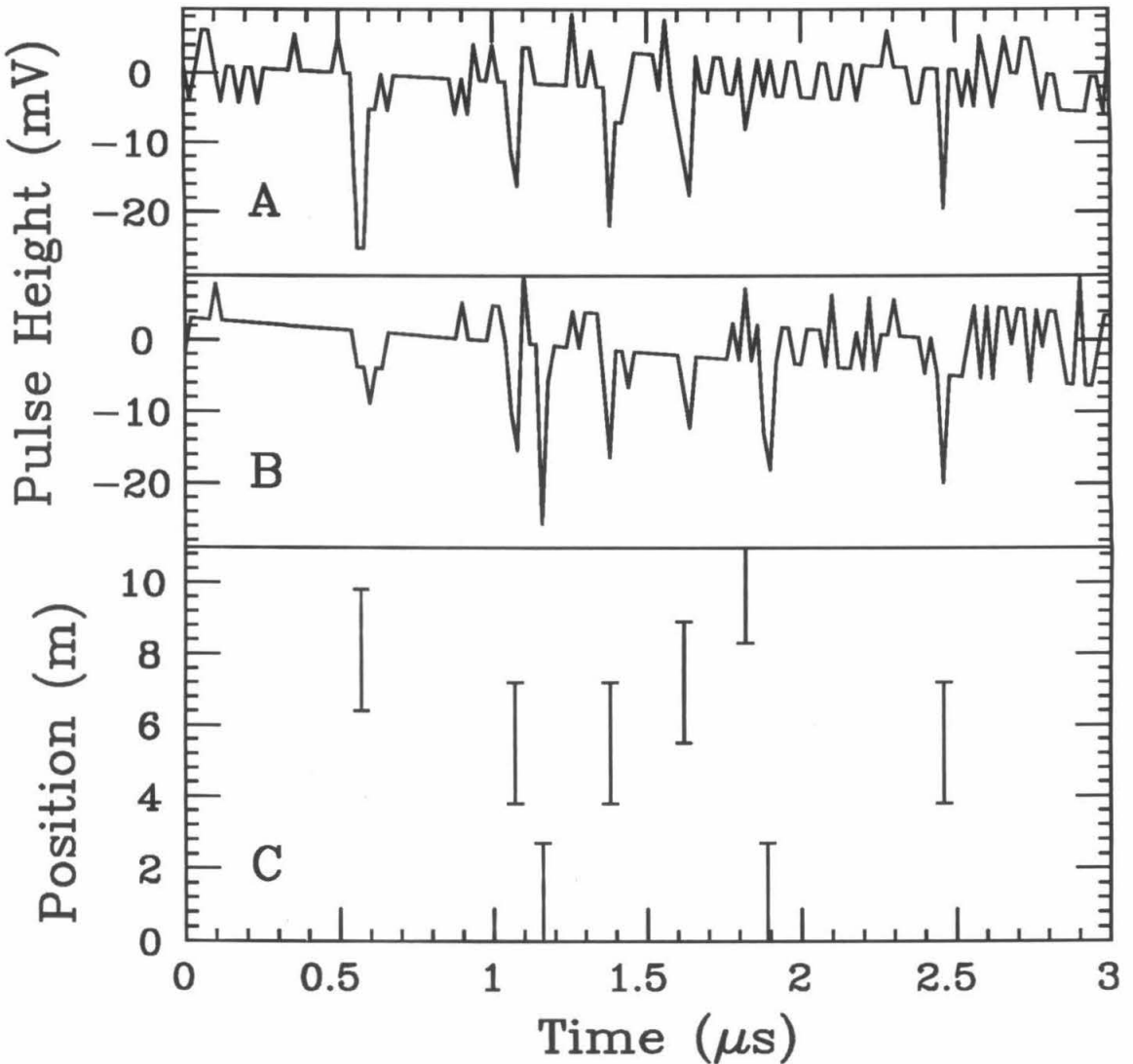


Figure 4.20: Positions of radioactivity pulses along the counter. (A) and (B) are the blown-up fast waveforms for the ends 1 and 0 of supercounter C4 of run 2752, event 1422 (Fig. 4.16); the slow waveforms of these two ends are the most “monopole-like” (least spiky). Using the time difference between the two ends, we obtain the position along the counter (11 m long) for each radioactivity pulse. The errors are large due to the 20 ns time resolution of the fast waveform digitizers.

4.3 Fast Monopole Analysis

In the previous section we have presented the analysis of the slow monopole data and found no evidence for the passage through the MACRO detector of slow monopoles or any other slow-moving ($\beta < 3 \times 10^{-3}$) and light-yielding particles. In this section we shall describe the analysis of the data collected using the fast monopole trigger in search for relatively fast monopoles in the velocity range of $2 \times 10^{-3} < \beta < 1.5 \times 10^{-2}$.

4.3.1 Waveform Baseline Fitting

Due to the large ionization of the relatively fast monopoles, their signals are so large that the 8 bit dynamic range of the slow WFDs (Table 3.2) is always saturated. And the signals are short (50-300 ns for the minimum pathlength of 19 cm) enough to fit in the fast WFD window (6.4 μ s). So only the fast WFDs are used for the fast monopole analysis.

The area of the waveform is a good measurement of the light yield of the traversing particles, while the usual ADC system has too narrow a gate for the relatively wide pulse produced by a particle within the velocity range of the fast monopole trigger. To compute the area, one needs to know the waveform baseline, which drifts with time because the WFD uses charge coupling devices (CCDs). This drift is approximately linear with the addition of a small non-linear term which is ignored. The baseline is fit with a linear function using an algorithm called *median fit* [92] which minimizes the sum of absolute deviations from the baseline: this reduces the effect of outliers. For comparison, the conventional least square fit minimizes the sum of squares of deviations and works best if the deviations are Gaussianly distributed which is not true in the case of waveform baseline fitting.

The fast waveform digitizer has a dynamic range of 11 bits and a voltage resolution of 1 mV per least count (Table 3.2). It took inputs from PMT dynode signals in the first year of this data taking, and from attenuated anodes in the second year (Fig. 3.11). One channel

of the fast WFD holds 320 samples. To select the initial data samples to fit, we first cut out those data significantly deviating from the baseline. Assuming that the waveform samples are $\{x_j, j = 1 \dots 320\}$, we define

$$\delta_j = [\max(0, |x_{j+1} - x_j| - 3)]^2, \quad (4.4)$$

where *three* is chosen because the waveform intrinsic fluctuation is of the order of two least counts. We remove any two contiguous samples j and $j + 1$ which satisfy $\delta_j + \delta_{j+1} > 20$ from the ensemble of samples to be fit. This removes samples containing significant jumps (fluctuations), such as fast phototube signals from muons and radioactivities. Large wide pulses from relatively fast monopoles are removed because of their photoelectron fluctuations.

We do a median fit to the remaining samples, find the mean absolute deviation σ , and remove any outliers defined as

$$|x_j - (a + bj)| > 5\sigma, \quad (4.5)$$

where a and b are the parameters for the fit baseline. This cycle of median fit and outlier removal is repeated until the fitting can be determined either as a success or as a failure. The fitting is flagged as a success if any one of the following conditions is met:

1. $\sigma < 1$;
2. no more outliers (as defined in Eq. 4.5) are present and $\sigma \leq 10$;
3. having iterated for nine times, and no more than five outliers are present, and $\sigma \leq 10$.

This is to be compared with that, in addition to its linear drift, the waveform baseline fluctuates with a magnitude of order of two least counts, varying from channel to channel. The fitting is flagged as a failure if

1. number of the remaining samples after the outlier removal is less than a certain number N , which we choose to be 75% of the total number of samples in the

waveform (denoted as N_t). For the fast WFD, $N_t = 320$ (Table 3.2), and thus we choose $N = 240$. For the slow WFD, $N_t = 455$ and we set $N = 340$.²

2. no more outliers are present and $\sigma > 10$;
3. having iterated for nine times, and no more than five outliers are present, and $\sigma > 10$;
4. having iterated for nine times, and still having more than five outliers.

The failures in the fast monopole analysis are treated on page 127.

All waveforms shown in this thesis have had their baseline fit and subtracted, except the top trace in Fig. 4.21 which is a raw waveform as recorded by the slow WFD. The bottom trace is the same waveform with the baseline subtracted. To show the size of the CCD-induced pedestal drift, the vertical scale is the signal scale at the input to the slow WFD, while all other waveforms in this thesis have their vertical scales converted back to the signal scale at the PMT fanout.

4.3.2 Fast Monopole Analysis

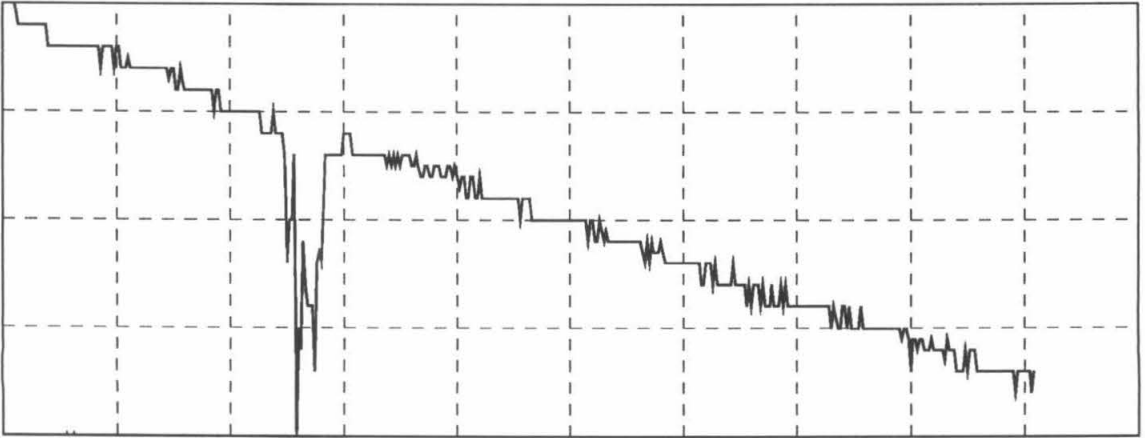
Among all runs selected in Table 4.1, a significant number of them are abnormal for the fast monopole trigger (FMT) while apparently normal for the slow monopole trigger. The logbook cut for the FMT reduces the number of good runs from 1467 to 1192 and the livetime is reduced from 552 days to 453 days (Table 4.3). The major contribution comes from those runs in which the FMT was unplugged (page 93) and this alone causes a livetime reduction of 51 days. The other major contribution comes from the runs in which the fast WFDs were malfunctioning and this reduces the livetime by another 45 days. Runs in which a fraction of the fast WFD channels were abnormal are kept, but the bad channels are excluded both from the following analysis and from the acceptance Monte Carlo simulations (Fig. 4.34). Although the fast monopole analysis cannot be performed for the runs with abnormal fast waveforms, the slow monopole analysis was still done with

²For muon events, a smaller number of waveform data samples were recorded because muon signals are fast and short: for the fast WFD, $N_t = 150$ and we choose $N = 80$. The muon slow waveform is not used in this thesis because it is absolutely saturated.

An LED Pulse

Scales: Horizontal= $2.5\mu\text{s}/\text{div}$, Vertical= $10\text{mV}/\text{div}$

Raw Waveform



With Baseline Subtracted

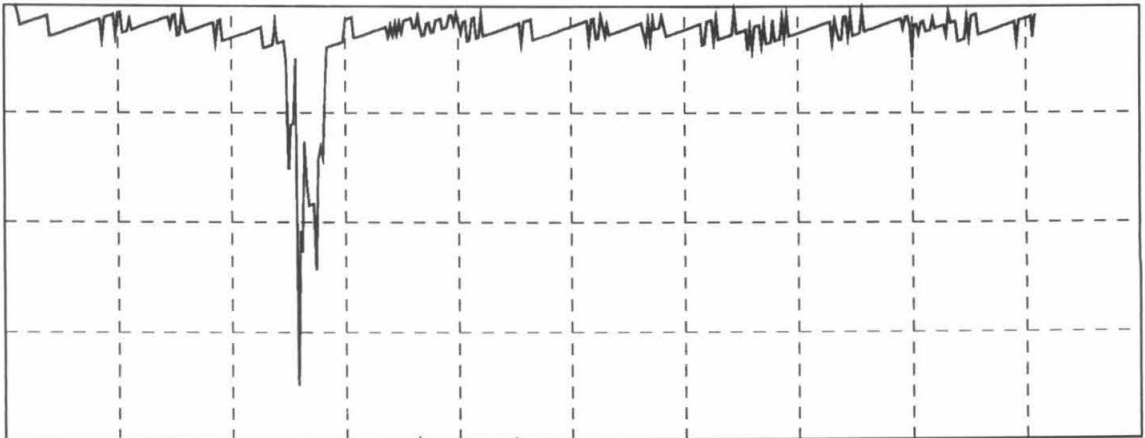


Figure 4.21: Waveform baseline subtraction. The vertical scale is the signal scale at the input to the slow WFD, while all other waveforms in this thesis have their vertical scales converted back to the signal scale at the PMT fanout.

Cut	Livetime (days)	Number of Candidates
from Table 4.1	552	—
logbook cut for FMT	453	140,173
IMBU hits in ≥ 2 faces	453	76,854
$\text{TOF}_{\text{max}} \geq 1\mu\text{s}$	453	47,496

Table 4.3: First cuts for the fast monopole analysis.

the slow waveforms in the previous section. In all 1192 selected runs, 140,173 events fired the fast monopole trigger.

For every FMT event, the IMBU ADCs/TDCs (page 65) were recorded. We define an IMBU hit as a scintillator counter whose two IMBU channels (corresponding to both counter ends) have numerically plausible ADC and TDC values — ADC value must not be zero, and either of the two TDCs (page 65) must be neither zero nor 511, the saturated count. This is quite a minimal requirement for an IMBU hit. An acceptable FMT event must have IMBU hits in at least two faces, because the FMT is a two face coincidence trigger. This requirement reduces the number of candidates to 76,854. The events removed by this requirement are due to electronic faults in the IMBU circuits generating extra noise events. This requirement does not reduce the trigger efficiency for real events. The noise events slightly increased the dead time, but this has been taken care of (page 91). These 63,319 noise events are a significant fraction (45%) of the FMT events, but they are only a small fraction (4.0%) of all 1.6×10^6 IMBU events (mainly consisting of muons).

For the 76,854 acceptable FMT events, we compute their time of flight (TOF) between two hit counters using the IMBU TDC system (page 65). Because the FMT trigger is the IMBU trigger vetoed by the SPAM trigger (Fig. 3.10) which has a $1\mu\text{s}$ coincidence gate, we reject any events with TOF less than $1\mu\text{s}$. For events firing more than two counters,

the maximum TOF between any pair of counters in different faces is used to make this cut conservative. This reduces the number of candidates to 47,496. The distribution of the maximum TOF is shown in Fig. 4.22. The peak at the far left consists of 2.2×10^4 muons which escaped the SPAM veto. They represent a small fraction (1.6%) of all 1.4×10^6 muons collected, which implies that the SPAM muon trigger has an efficiency of 98.4%. The flat TOF distribution is consistent with the hypothesis that these FMT events are accidental coincidences of radioactivity pulses (Fig. 4.23). Apparently the SPAM veto did not induce any appreciable deficit in the TOF range of 0-1 μ s. This is because the SPAM trigger has a higher discriminator threshold than the IMBU trigger and radioactivities have a very steep pulse height spectrum. However, the origin for the small dip at the left side is not understood. As said, the 47,496 FMTs are mainly composed of the accidental coincidence of radioactivities. Considering that they occurred over 453 days livetime, the average rate is 1.2×10^{-3} Hz, while the expected accidental coincidence rate from the background radioactivities is roughly estimated to be 0.5×10^{-3} Hz — they are approximately in agreement with each other. We believe that the reason the actual average accidental rate is higher than the estimate is due to upward fluctuations in IMBU singles rates due either to small discriminator level shifts or to small phototube gain drifts.

Since the light yield of monopoles in the FMT-sensitive velocity range is at least twenty times greater than that of minimum ionized muons (Fig. 3.2), the next logical step is to impose a cut on the amount of light yield, or the amount of charge produced by the phototube. To calibrate the response of the apparatus, we fit the fast waveform baseline and compute the integral charge (area) for muons. When we fit the muon waveform baseline, we follow the same fitting procedure for monopole events prescribed in the subsection 4.3.1, but we use the least square fit rather than the median fit to save computing time. The muon integral charge is computed by a simple sum of the deviations of all data samples from the baseline. The distribution of this charge for each counter-end is fit using a parametrized Landau function (Fig. 4.24),

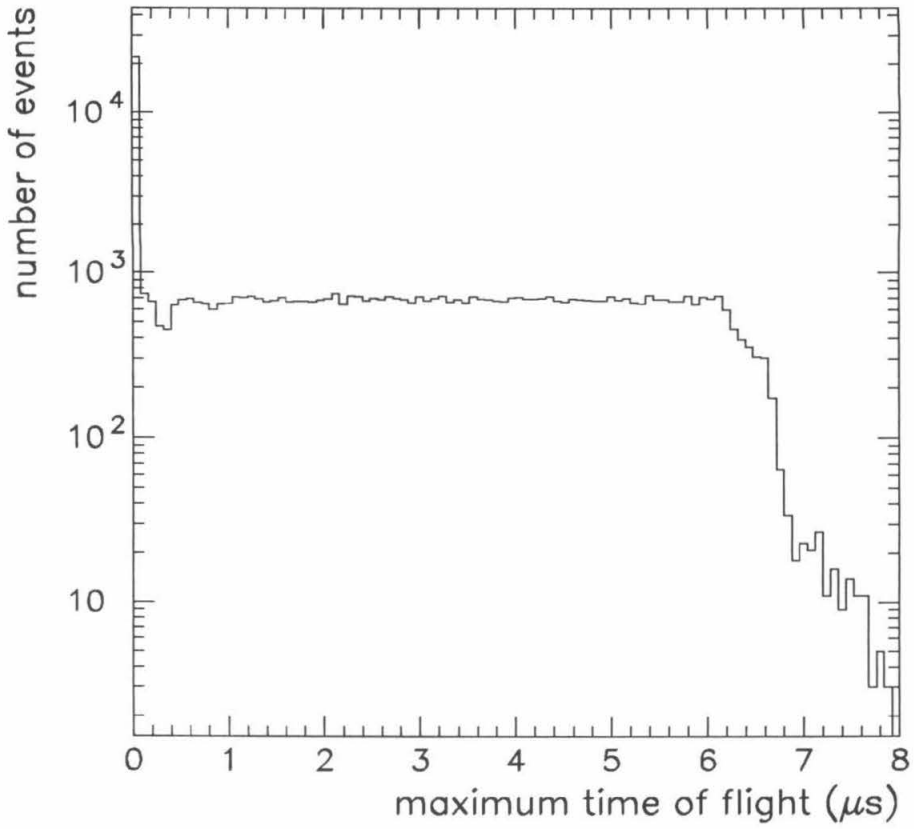
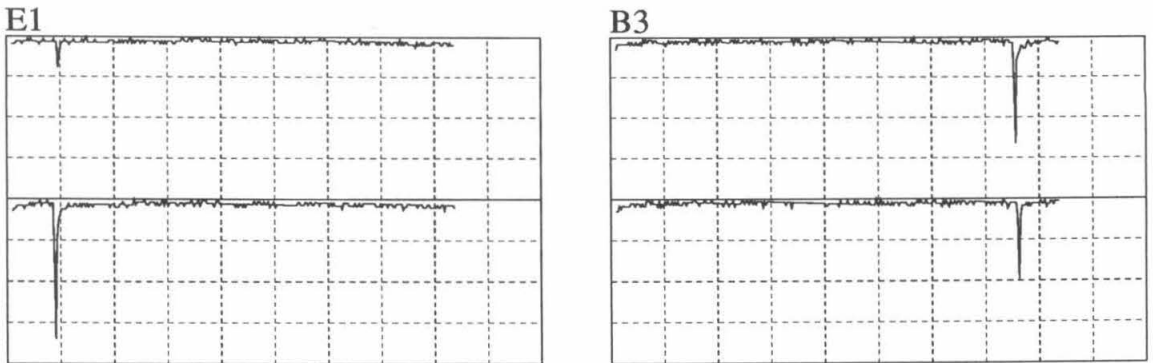


Figure 4.22: Maximum time of flight of the 76,854 acceptable fast monopole events.



Scales: Horizontal=0.75 μs/div, Vertical=70mV/div

Figure 4.23: An example of an FMT event which is an accidental coincidence of radioactivities. For reference, a typical muon pulse height is about 1.5 Volts.

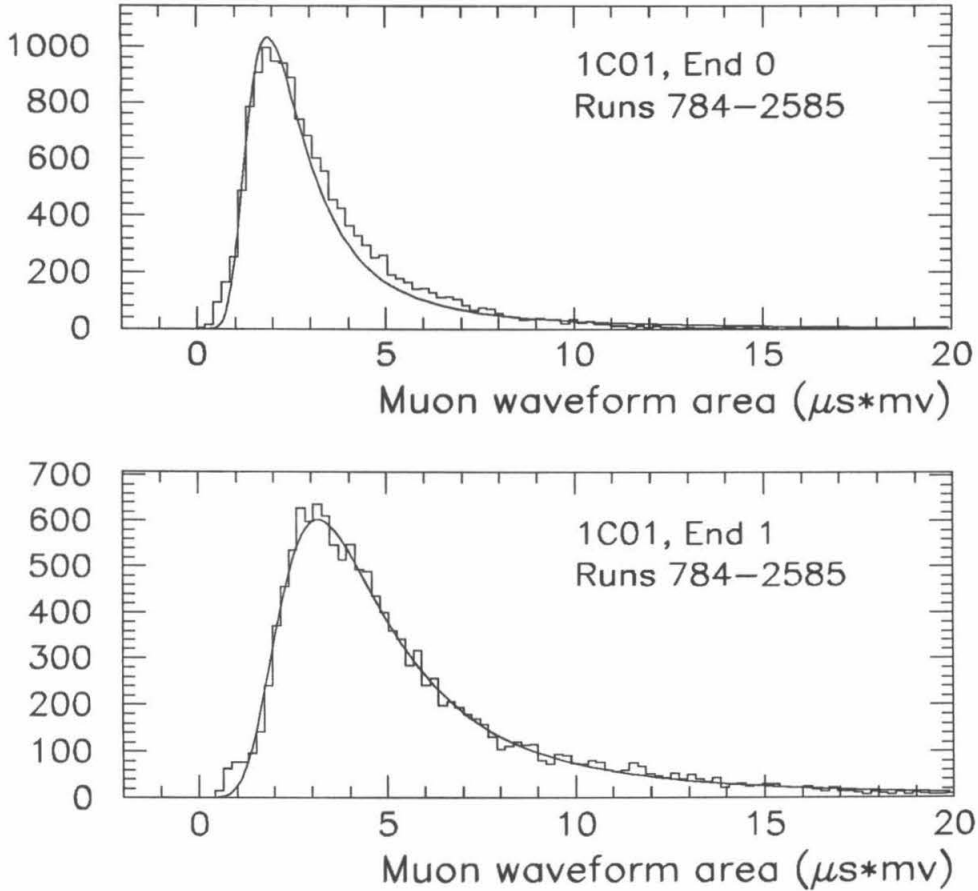


Figure 4.24: An example of the muon waveform area distributions. See Fig. 3.11 for the fast WFD configuration in runs 784-2585. The curves are fit using the parametrized Landau function in Eq. 4.6. The WFDs are multiplexed into supercounters while the IMBU system has no multiplexing. Thus, the IMBU system identifies which counter in a supercounter has the muon signal.

$$f(q) = a\phi\left(\frac{q - q_0}{b}\right), \quad (4.6)$$

where ϕ is the Landau distribution,

$$\phi(\lambda) = \frac{1}{2\pi i} \int_{\sigma - i\infty}^{\sigma + i\infty} \exp(\lambda u + u \ln u) du \quad (\sigma > 0), \quad (4.7)$$

q is the integral charge, and a , b and q_0 are the fit parameters. In particular, q_0 is the peak charge, which will be quoted as the muon charge in the further analysis. This makes the charge cut discussed below conservative, since the peak charge is smaller than the average charge.

For the 47,496 FMT events which survived the TOF cut, we fit the fast waveform baseline and the fitting *fails* for 194 events. The waveforms of these 194 events were visually scanned and found to fall into the three categories shown in Fig. 4.25:

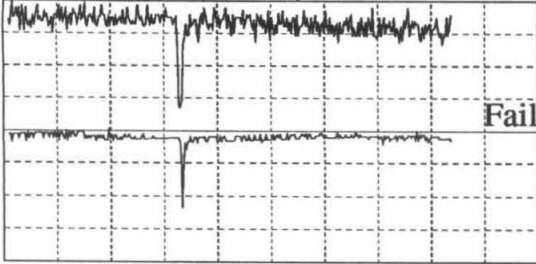
- (A) In 117 events the baseline of one waveform channel is too noisy to satisfy the fitting requirement. Despite the noisy baseline, the radioactivity pulses are still quite evident in all four waveform channels (four supercounter-ends). With their signal size much smaller compared to muons, obviously these pulses would not be able to pass the charge cut (requiring the charge to be greater than the muon charge) detailed below even if the fitting were successful.
- (B) In another 57 events the waveform channels for the bottom face have a sporadically malfunctioning seventh bit. This notwithstanding, the radioactivity pulses are still evident and can be rejected by the charge cut.
- (C) In the remaining 20 events, electronic oscillations show up in one supercounter, causing the failure of the baseline fitting. The other supercounter displays a radioactivity pulse, which does not survive the charge cut.

In summary, all 194 events which failed the fitting are rejected using the charge cut, and thus we do not lose any efficiency because of the baseline-fitting-failure.

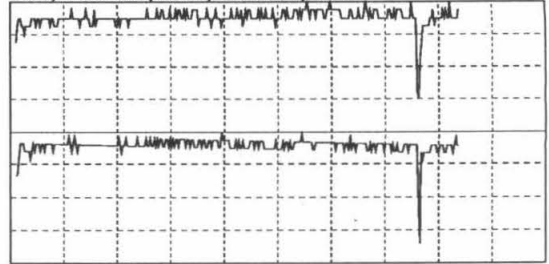
For the FMT events whose baselines have been fit successfully, we compute the integral charge. We ignore the “positive” waveform samples (those at the positive side of the baseline) when computing the charge of the FMT events, and thus the charge may be *larger* than the actual charge, making this charge calculation conservative. For comparison,

Run 3675 Event 11199

B1, 750ns/div, 70mv/div



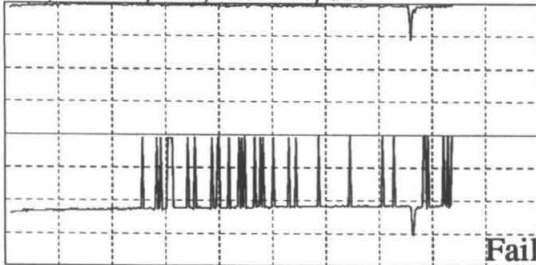
E1, 750ns/div, 20mv/div



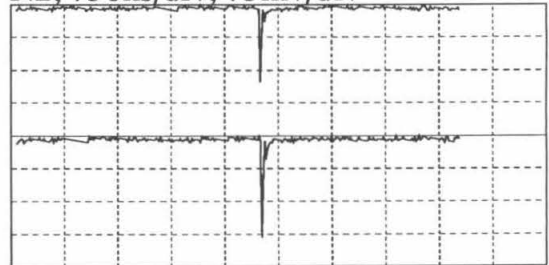
A. Baseline too noisy, making the fitting a failure. There are 117 events like this.

Run 3759 Event 22986

B3, 750ns/div, 150mv/div



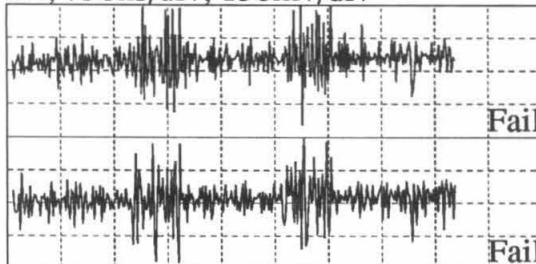
N2, 750ns/div, 75mv/div



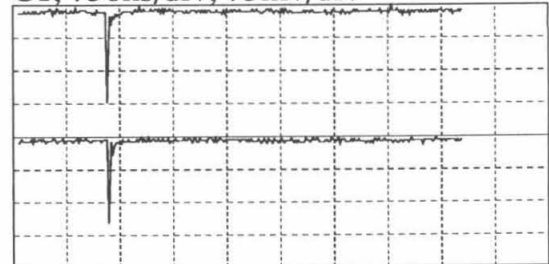
B. The 7th bit of the WFD channel is bad sporadically, but the radioactivity pulse is still quite visible. There are 57 events like this.

Run 3237 Event 9364

B4, 750ns/div, 150mv/div



C1, 750ns/div, 75mv/div



C. Electronic noise in one counter and the other counter is radioactivity. There are 20 events of this type.

Figure 4.25: Categorization of the 194 FMT events which failed the baseline-fitting.

when calculating the charge of the muons for calibration purpose, we subtract the positive samples from the integral area to get a more accurate result, because the positive samples and the negative ones from electronic oscillations would cancel each other — in any case this is only a small effect for muons because the large muon signals dominate. We normalize this waveform charge of each counter-end of an FMT event by the muon charge of that counter-end and denote the geometric average³ of the charges from both ends as the “normalized” charge in a counter, a detector-independent measurement of the amount of light yield in the counter in units of muon light yield. Then we place a *double face charge cut* by requiring that the normalized charge in both hit faces be greater than unity (Fig. 4.26). This is a very strong cut and only 58 candidates survive. The events removed by this cut are due to the aforementioned accidental coincidence of radioactivity pulses.

Before we proceed with further analysis of these 58 candidates, let us examine a caveat associated with this cut and a remedy for potential problems. The maximum possible time of flight covered by the FMT trigger is $7 \mu\text{s}$, determined by its coincidence gate length. But the fast WFD time window is only $6.4 \mu\text{s}$ long. Thus, if the time of flight is longer than $6 \mu\text{s}$, the first signal (produced when the particle enters the detector) is outside the WFD time window and thus is missed — the *double face charge cut* in the preceding paragraph is *invalid* for $\text{TOF} \gtrsim 6 \mu\text{s}$. A remedy for this problem is to use only *single face* information for those events with $\text{TOF} > 5 \mu\text{s}$ ($5 \mu\text{s}$ is chosen in order to be conservative). For a particle with a vertical trajectory, a TOF longer than $5 \mu\text{s}$ translates into the signals in both faces having a pulse width longer than 200 ns, if we assume no corner-clipping. Therefore, for events with TOF longer than $5 \mu\text{s}$, we place a *single face charge and width cut* by requiring that in either of the two hit faces the normalized charge be greater than unity and the signal width be greater than 100 ns. The width cut is also placed in the Monte Carlo simulations (section 4.4) to exclude the extreme corner-clipping trajectories

³If we assume a simple exponential counter response which is true except near the ends (Fig. 2.8), the geometric average of charges from both ends does not depend on the location of the light source along the counter.

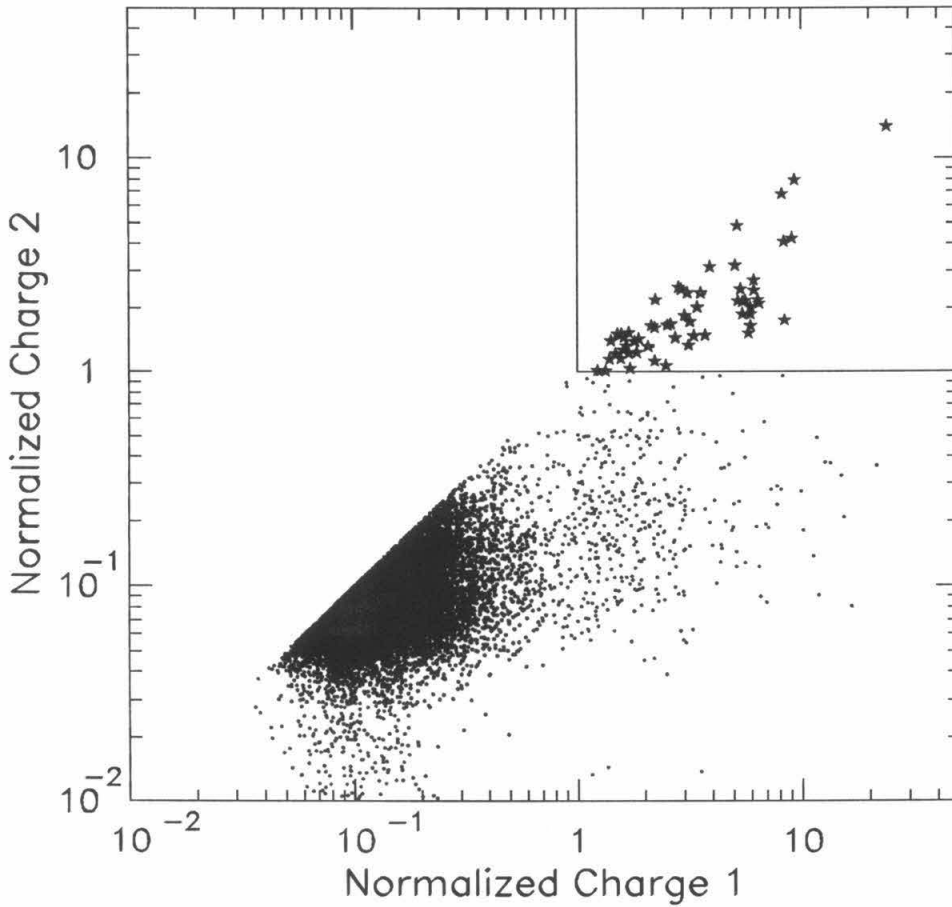


Figure 4.26: Double face charge cut. Plotted are the largest normalized charge (the horizontal axis) and the second largest one (the vertical axis) among the hit counters for all the events whose maximum time of flight is longer $1 \mu s$. Also indicated the cut placed at $1 \times$ minimum ionizing charge. There are 58 events which survived this cut.

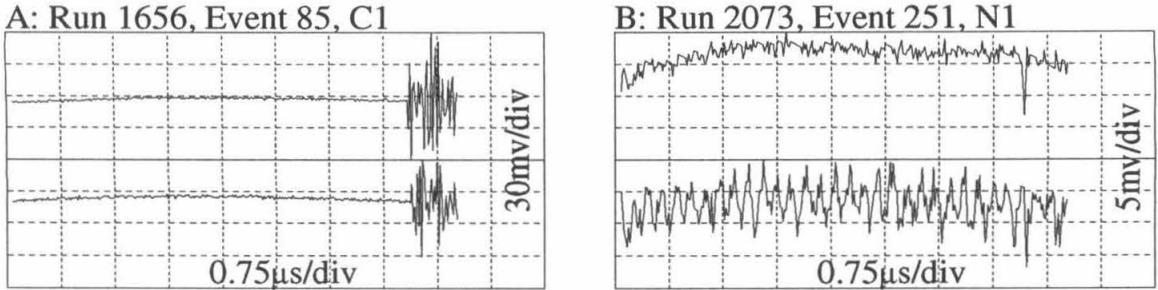


Figure 4.27: Categorization of the 29 fast monopole events with $\text{TOF} > 5 \mu\text{s}$ which passed the single face charge and width cut: (A) Seven events are electrical noise; (B) The remaining 22 events are radioactivity pulses having noisy baselines.

from the computer acceptance. The width is calculated as the integral area over the pulse height. Only 29 events with $\text{TOF} > 5 \mu\text{s}$ meet this single face charge and width cut. Visual scanning of these 29 events reveals that they are composed of two categories of events as shown in Fig. 4.27 and neither of them resembles a monopole signal:

- (A) Seven events are electrical noise. Although the amplitude of noise varies from channel to channel, the noise appears simultaneously in every channel. The TOF is miscalculated to be greater than $5 \mu\text{s}$ due to the error of the IMBU TDC system in recording the electrical noise events. When computing the integral charge, the positive samples are ignored in order to be conservative (page 127). Thus, the computed charge for electrical noise waveform is sufficiently large to pass the charge cut. The electrical noise lasted long enough ($\sim 1 \mu\text{s}$), satisfying the width cut requirement.
- (B) The remaining 22 events are due to accidental coincidence of radioactivity pulses with $\text{TOF} > 5 \mu\text{s}$, accompanied by noisy waveform baseline in one of the WFD modules. The noisy baseline is similar to that in Fig. 4.25(A), but not as bad; so the fitting succeeded. Because we ignore the positive samples in computing charge, the contribution from the noisy baseline dominates the total charge (or area) and inflate it to pass the charge cut. The radioactivity pulse height is very small, making the computed width (integral area over pulse height) artificially large to pass the width cut.

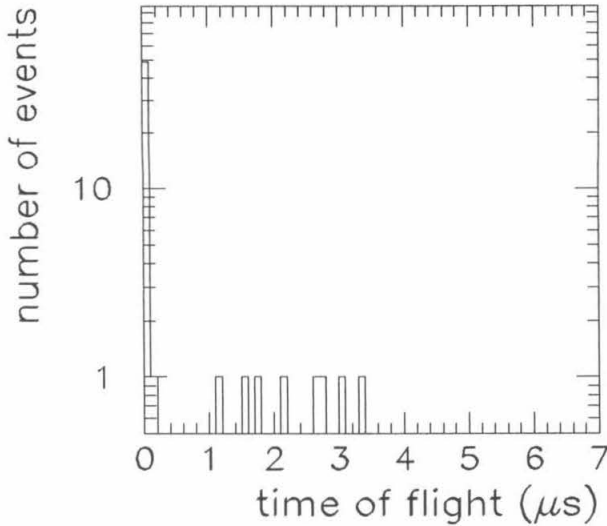


Figure 4.28: Time of flight between the two counters having the largest charges for the 58 fast monopole candidates which have passed the double face charge cut.

Now that we have provided the single face charge and width cut as a remedy to the shortcoming of the double face charge cut, let us go back to those 58 candidates which passed the double face charge cut. We compute their time of flight between the two counters having the largest charges and require this TOF to be greater than $1 \mu s$ (Fig. 4.28). Only eight events meet this requirement. The events rejected by this cut are muons accompanied by accidental radioactivity pulses in other counters (Fig. 4.29). They occurred when the SPAM muon trigger had problems, and thus they escaped the SPAM veto. The accidental radioactivity pulses enlarged the maximum time of flight, allowing the events to pass the $\text{TOF}_{\text{max}} \geq 1 \mu s$ cut in Table 4.3.

For the eight finally selected candidates, their charges in the two hit counters is shown in Fig. 4.30. The charges are all less 2.5 times the muon charge. The fast monopole trigger is only sensitive to particles in the velocity range from $2 \times 10^{-3}c$ to $1.5 \times 10^{-2}c$. In this velocity range, the monopole light yield is at least 20 times the muon light yield; even

Run 3213 Event 3988

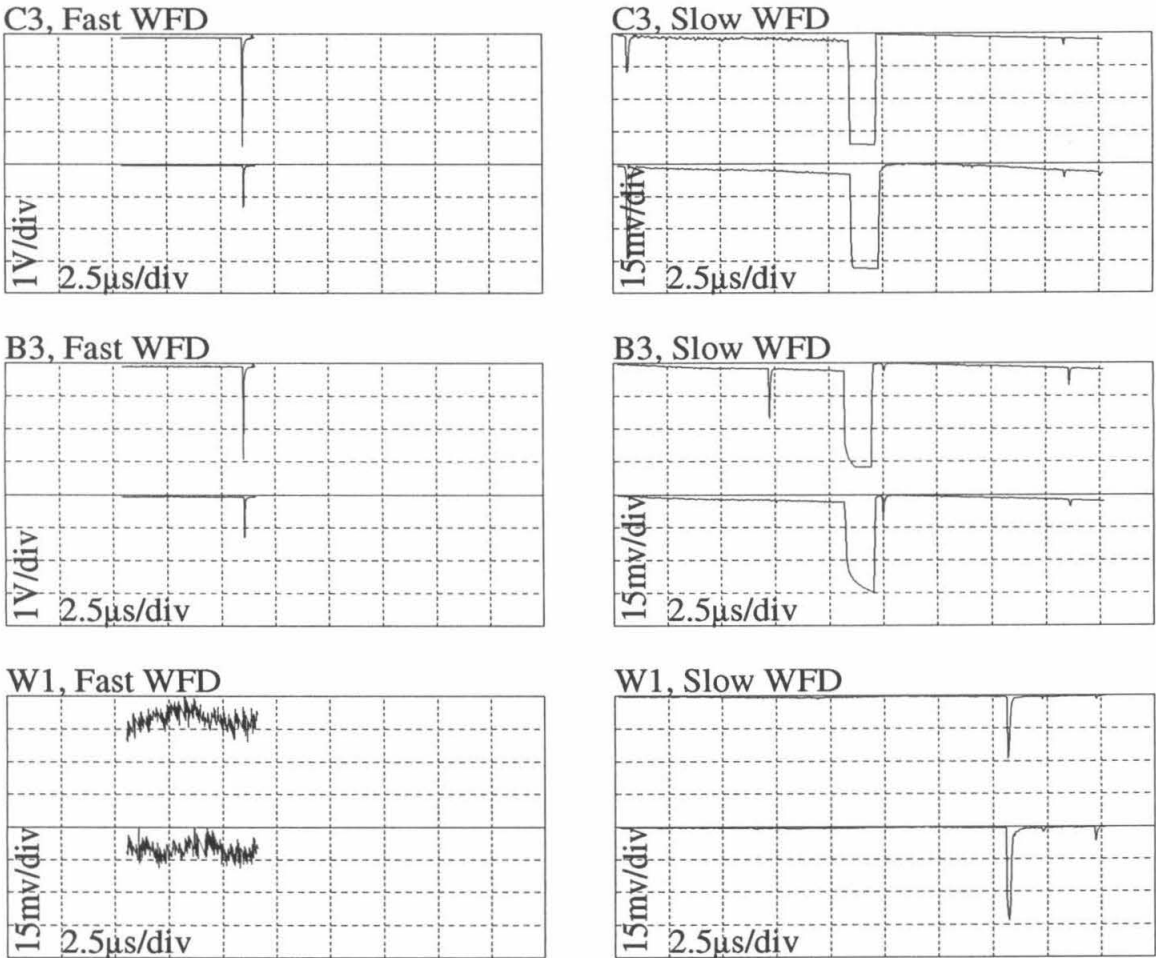


Figure 4.29: A fast monopole candidate faked by a muon accompanied by an accidental radioactivity pulse. The muon went through counter 1C11 (supercounter C3) and 1B09 (B3) and saturated the slow WFDs as expected. The radioactivity pulse occurred in counter 1W01 (W1) $7\ \mu\text{s}$ later, and thus is outside the fast WFD time window.

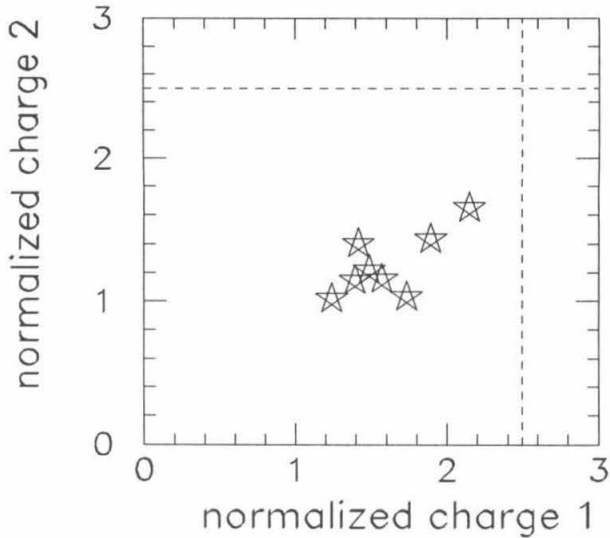
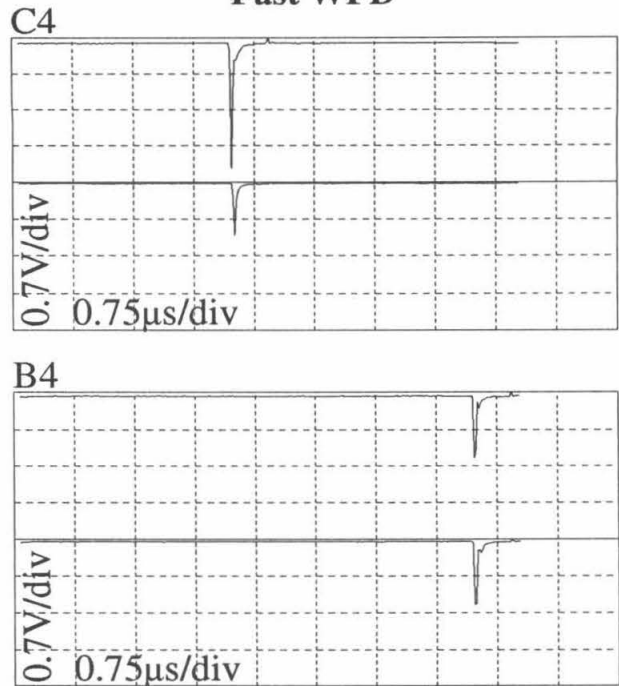


Figure 4.30: The charges of the eight final fast monopole candidates. For each event, we plot the normalized charges at the two hit counters, the larger one of which is used as the horizontal coordinate.

the $\frac{1}{5}e$ particle produces at least eight times as much light as the muon (Fig. 3.2); and nuclearite light yield is orders of magnitude larger than the minimum ionizing light yield (Fig. 3.19). This alone can exclude these eight events as candidates for monopoles, $\frac{1}{5}e$ superstring particle, or nuclearites.

To investigate further, the waveforms and the streamer tube tracks of these eight events are visually scanned. Both the waveforms and the tracks of six events are consistent with signatures of stopping muons — a muon penetrated one layer of scintillator counters and then stopped inside the first supermodule, and its decay electron fired another scintillator counter (Fig. 4.31). Since muons have a lifetime of $2.2\mu\text{s}$, the stopping muons easily satisfy the 1-7 μs time of flight requirement. In the seventh event, the track entered the first supermodule from the inactive south face (Fig. 4.32). Thus, it hit only one counter and the FMT was fired because of another activity in another counter. Finally, the eighth event occurred when the streamer tubes were not functioning, and its waveforms are consistent

Run 3153, Event 490 Fast WFD

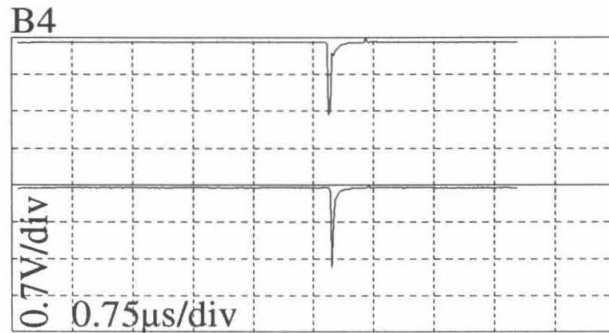
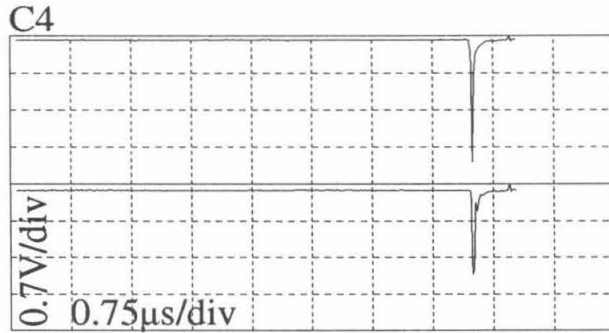


Streamer Tubes, Wire View only



Figure 4.31: An FMT candidate which is a stopping muon. Six of the eight final FMT candidates have similar signals in both waveforms and streamer tubes, indicating that they are stopping muons. For simplicity, we only show the streamer tube wire view, in which a dot indicates a hit wire, a box indicates a fired scintillator counter and the dashes are best-fit muon tracks.

Run 80066, Event 1506
Fast WFD



Streamer Tubes, Wire View only

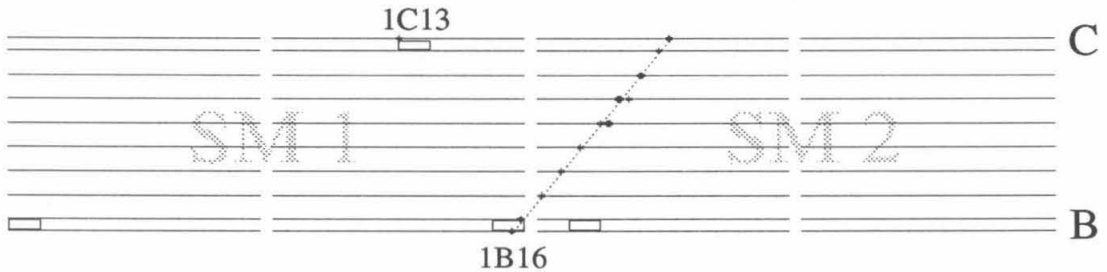


Figure 4.32: An FMT candidate in which a muon crossed two supermodules (SMs). Because of the inactive south face in the first supermodule (SM 1), the muon hit only one counter (1B16) in SM 1. The FMT trigger is fired because another activity occurred $1.7 \mu\text{s}$ later in counter 1C13.

with those expected of stopping muons. The number of stopping muons (6 or 7) agrees with the expected number of 8.1 which is calculated in Appendix D.

In conclusion, we found no evidence of the passage through the first supermodule of particles with 2.5 times the muon light yield in the velocity range from 2×10^{-3} to 1.5×10^{-2} .

4.4 Acceptance and Flux Limits

To convert our negative search into a detector independent flux limit, we need to compute the acceptance of the detector, which is integral over the exterior area of the detector of the solid angle of sensitivity at each place. Since supermassive particles can easily penetrate the earth, their fluxes are expected to be isotropic. Taking into account the detailed geometry of the scintillator counters, we have simulated the acceptance of the first supermodule for isotropic trajectories using the Monte Carlo technique.

A trajectory is generated randomly and isotropically and projected on the first supermodule. If its pathlength through a scintillator counter (in case of the fast monopole trigger with no multiplexing) or a supercounter (in case of the multiplexed slow monopole trigger) is greater than a minimum pathlength, that counter (supercounter) is considered to be hit. We count the number of trajectories firing scintillator counters in two of the five active faces of the first supermodule. Comparing this count with total number of generated trajectories, we obtain the acceptance. The acceptance is found to have only a weak dependence on the minimum pathlength, which is chosen as 15 cm. This accepts a small number of corner-clipping trajectories, since the minimum thickness of the liquid scintillator body is 19 cm. To be realistic, we also consider the actual trigger configurations: for the slow monopole trigger, we compute the pulse width from the pathlength and the particle velocity and require it to be greater than 200 ns, the minimum pulse width to fire the slow monopole trigger (Fig. 3.16). We also put in the time of flight requirement: for each trajectory with

two face hits, we calculate the distance between the two hit positions (*length of flight*) and consequently the time of flight for a given velocity, and require it to be greater than $600 \mu\text{s}$ (page 70). For the fast monopole trigger, we require the time of flight to be in the range of $1\text{-}7 \mu\text{s}$, the FMT coincidence window (Fig. 3.10). In the fast monopole analysis in the case of time of flight longer than $5 \mu\text{s}$, we have an additional requirement that one of the pulse widths must be greater than 100 ns (page 129). The same requirement is included in the Monte Carlo. Thus, we obtain the acceptance as a function of the velocity of the penetrating particle as shown in Fig. 4.33. Shown in the low β range is the acceptance of the slow monopole trigger, which curves down at $\beta \approx 3 \times 10^{-3}$ because of the aforementioned requirement of 200 ns minimum pulse width. The geometry does not constrain the acceptance at the low β end, so it is flat; the low β extremity of the flux limit is determined by other factors (Fig. 3.18). The curve at the right side is for the fast monopole trigger, whose shape is mainly determined by the TOF requirement. If we ignore the variation in the length of flight and always use the distance between the center and bottom faces (4.5 m), the acceptance would have a rectangular shape as shown with dashes in the plot.

Next we multiply the acceptance of each trigger by the corresponding livetime and the product is shown in Fig. 4.34. The livetime for the slow monopole trigger is 541 days. This multiplied by the acceptance from Fig. 4.33 is shown in Fig 4.34. For the fast monopole trigger, the total livetime is 453 days, which, multiplied by the acceptance, is shown as the curve with the legend “FMT, ideal.” In reality a few different counters were bad for the fast monopole triggers (page 121) for different periods of time. Totally there are 27 different combinations of good and bad counters, including the configuration that all counters are good. Each combination has a different acceptance, *e.g.*, the acceptance with a bad counter 1B01 (see page 27 for the nomenclature) is different from that with 1B08 bad. For each combination the acceptance is simulated and the livetime is calculated. The sum of their products over all 27 combinations is shown in Fig. 4.34 as the curve with legend “FMT,” which is later used to obtain the flux limit.

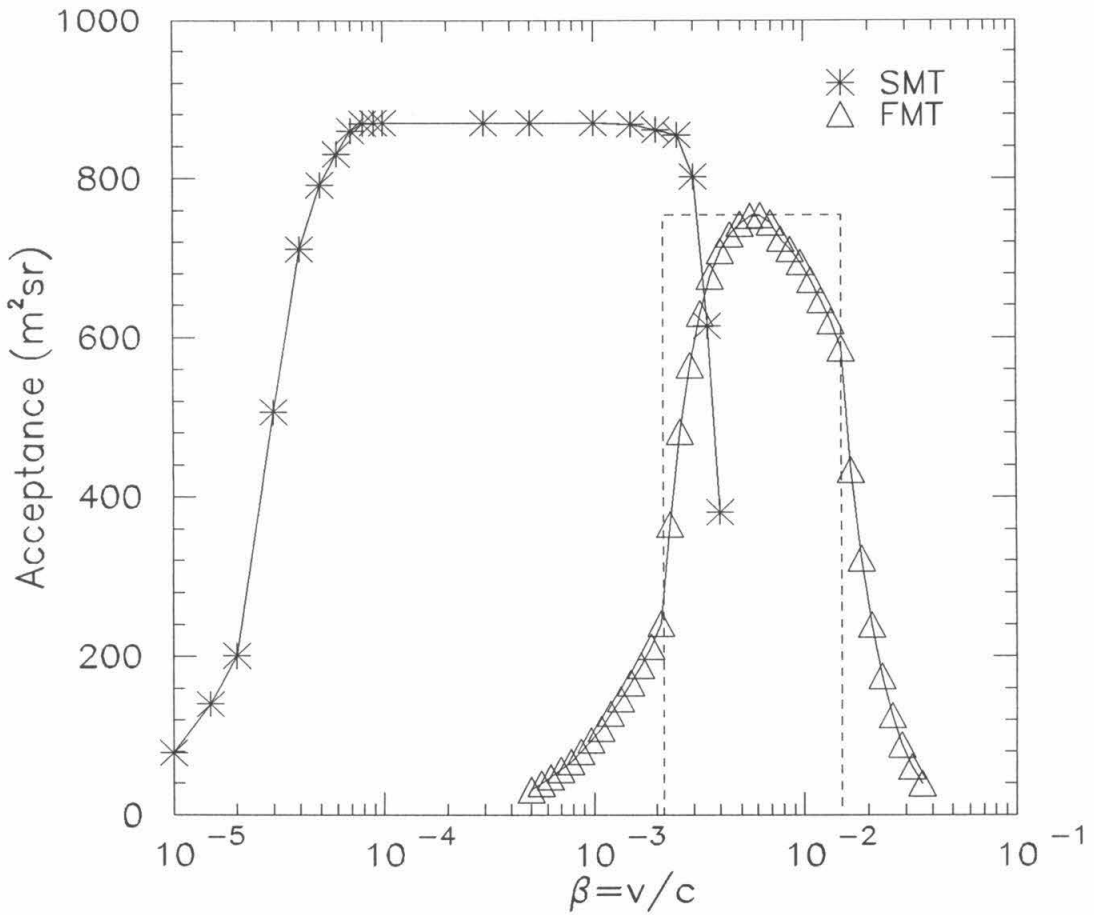


Figure 4.33: Acceptance of the first supermodule as a function of the velocity of the penetrating particle for the two monopole triggers. On the left side is the acceptance of the slow monopole trigger (SMT), while on the right side is that of the fast monopole trigger (FMT). The dashed rectangle indicates the sensitive β range constrained by the 1-7 μ s TOF requirement, assuming the length of flight to be the distance between the center and bottom faces (4.5 m).

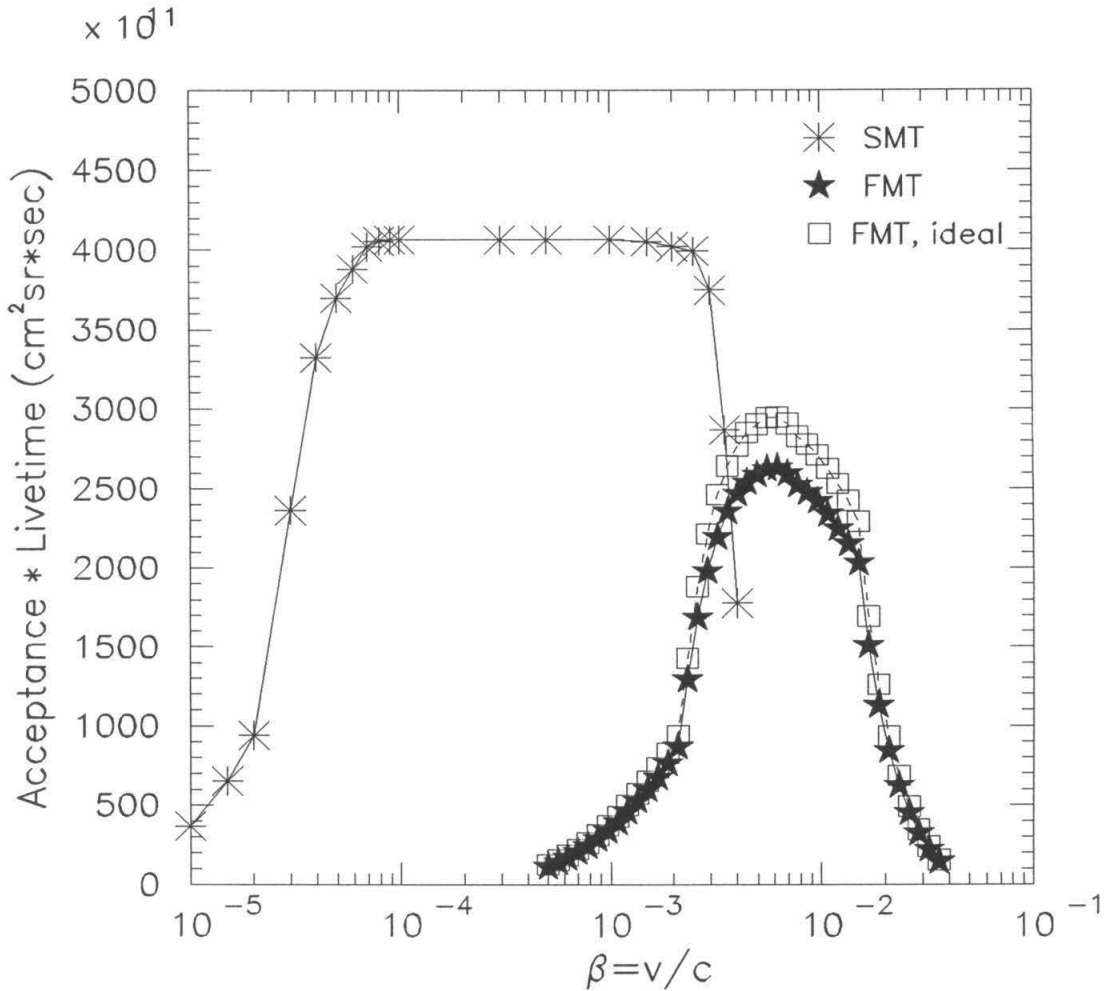


Figure 4.34: The product of the acceptance of each monopole trigger and the corresponding livetime as a function of the velocity of the penetrating particle. The curve with the legend “FMT, ideal” denotes the hypothetical configuration in which none of the scintillator counters were ever turned off. In reality a few different counters were bad for the fast monopole trigger for different periods of time and this is included in the simulation.

With no evidence of a candidate, we establish an upper flux limit for supermassive particles at 90% confidence level by dividing 2.3^4 by the inverse of the aforementioned acceptance livetime product. Shown in Fig. 4.35 is this flux limit with the sensitive β range for monopoles and dyons indicated. The velocity range at the low β end is determined by the trigger sensitivity as compared with the expected light yield, as shown in Fig. 3.18. We indicate with a bold solid line the most conservative velocity range derived from the overconservative Ahlen-Tarlé model (section 3.1.1). The plain solid line indicates the additional sensitive velocity range derived from the light yield converted from Ficeneč *et al.*'s proton scintillation measurement. The dashed line extending below $\beta = 1 \times 10^{-4}$ assumes that the monopole is a dyon with a unit electric charge. Also shown are the flux limits from previous searches and the Parker bound (page 9) as well as the anticipated limit reachable by the full MACRO detector after five years of operation. This same flux limit also applies to $\frac{1}{5}e$ superstring particles and $m > 0.1$ g nuclearites. For 10^{-10} g $< m < 0.1$ g, only downward-going nuclearites can reach the MACRO detector, and thus their flux limit is less restrictive by a factor of two as shown in Fig. 4.36.

⁴If the expected number of events is 2.3, the probability to see at least one event is 90%, according to Poisson statistics.

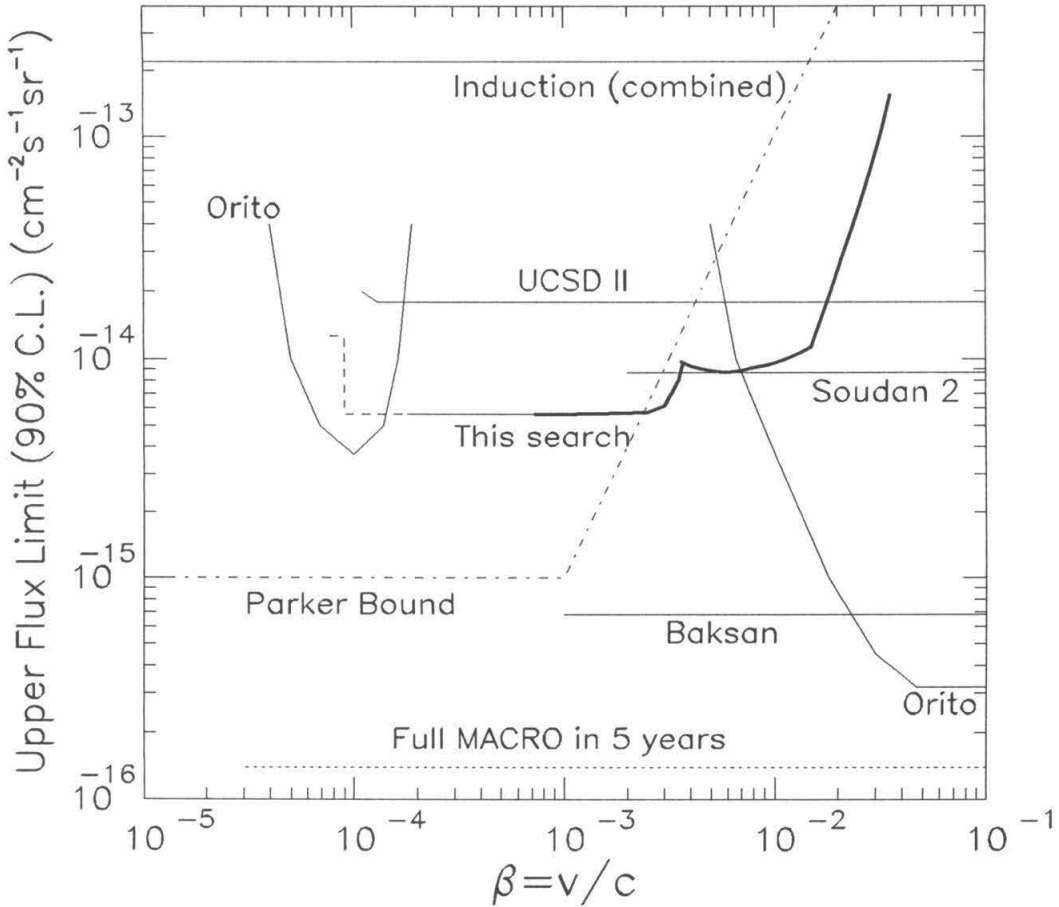


Figure 4.35: The upper limits on GUT monopole flux as a function of β . See page 141 for interpretation of this search as a function of β . The astrophysical Parker bound [24] is calculated according to Eq. 1.8 on page 9 assuming GUT monopole mass as 10^{17} GeV. The previous direct searches are reviewed in section 1.1.5 and labelled as: Induction (Combined) [30], UCSD II (He-CH₄) [46], Soudan 2 (Ar-CO₂) [47], Baksan (scintillator) [37], and Orito (CR-39) [48]. Also shown is the anticipated limit reachable by the full MACRO detector after five years of operation.

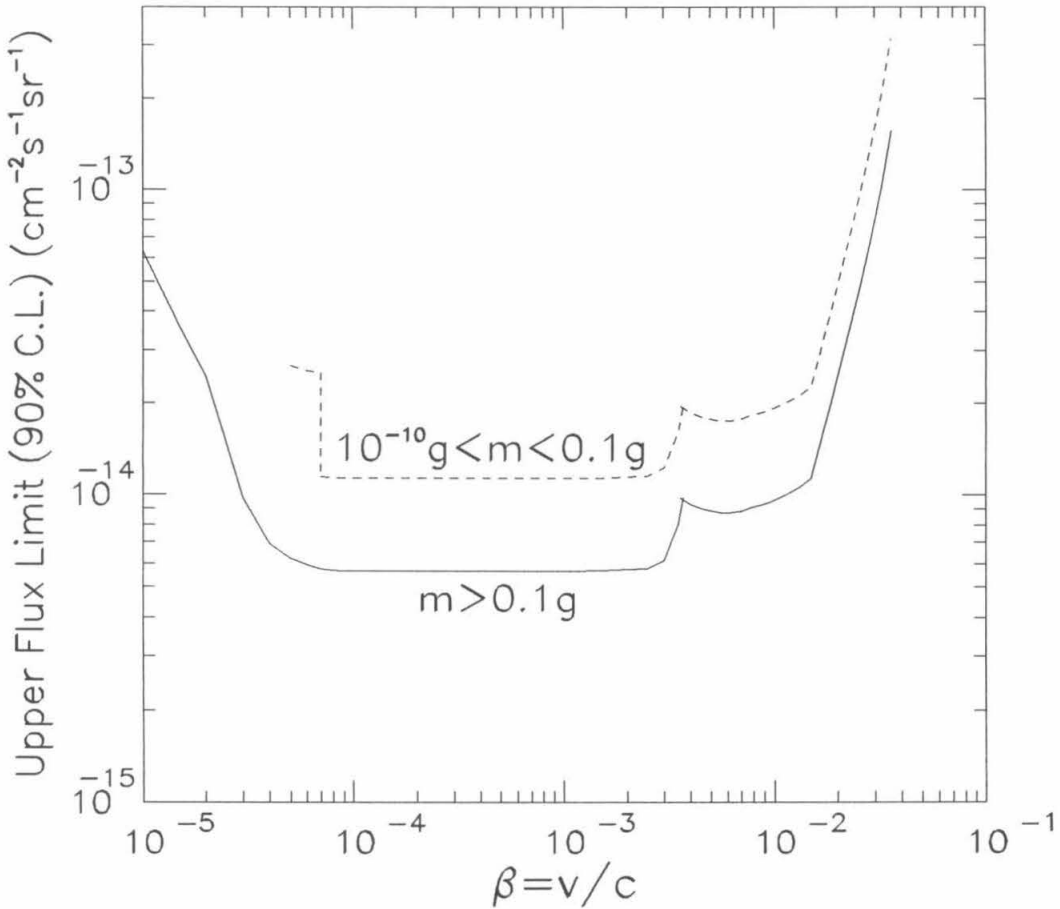


Figure 4.36: The upper limits on nuclearite flux as a function of β . The dashed lines (downward search only) is for nuclearites lighter than 0.1 g and therefore not having enough kinetic energy to come through the entire earth. The solid line (downward and upward search) is for nuclearites greater than 0.1 g and thus having enough kinetic energy to penetrate the earth.

Chapter 5

Conclusions

Magnetic monopoles necessarily exist in grand unified gauge theories. Strange quark matter may be the most stable form of matter. Discovery of either one would have profound impact on a lot of fields in modern physics. In this thesis we have presented a search for both of them and any other kind of supermassive particles that are scintillating, slow-moving and highly-penetrating.

The MACRO detector, a large underground detector, is being built, with the primary physics goal of search for GUT monopoles at a flux level beyond the Parker bound. It deploys scintillator counters, streamer tubes and track-etch detectors at a large scale. These three techniques together provide the necessary redundancy for a search for rare phenomena like GUT monopoles. When completed, MACRO will have an acceptance of $10,000 \text{ m}^2\text{sr}$. With a little over five years of operations, it will be able to search for monopoles at a flux level an order of magnitude lower than the Parker bound as indicated in Fig. 4.35.

Using the scintillator subsystem and with only the first supermodule ($\sim 1/12$ of the full detector), this thesis has searched for monopoles and other supermassive particles over a wide velocity range $10^{-4} \lesssim \beta \lesssim 10^{-2}$, in which GUT monopoles are most likely to be. The sensitivity in the low β region owes to the highly specialized slow monopole trigger system. The first supermodule has an acceptance of $870 \text{ m}^2\text{sr}$ for an isotropic flux.

In two years of operations, the absence of candidates for penetrating, slow-moving and scintillating particles implies an upper limit on the flux of various supermassive particles at $8.7 \times 10^{-15} \text{cm}^{-2} \text{sr}^{-1} \text{sec}^{-1}$ for $3 \times 10^{-3} < \beta < 2 \times 10^{-2}$, and at $5.6 \times 10^{-15} \text{cm}^{-2} \text{sr}^{-1} \text{sec}^{-1}$ for $\beta_0 < \beta < 3 \times 10^{-3}$, as shown in Figs. 4.35 and 4.36. The low velocity cutoff β_0 depends on the type of supermassive particles and can be obtained from Figs. 3.18 and 3.19. As shown in those two figures, vertical counters require more light than horizontal counters to achieve 90% slow monopole trigger efficiency. To be conservative, we used the required amount of light in vertical counters to obtain the following low end cutoff β_0 .

For bare monopoles, the optimistic cutoff is $\beta_0 = 1.8 \times 10^{-4}$, deduced from monopole light yield based on Ficenece *et al.*'s slow proton scintillation measurements, and the most conservative threshold is $\beta_0 = 7 \times 10^{-4}$, based on the overconservative Ahlen-Tarlé model. As has been argued in section 3.1.1, the optimistic one is more likely. If true, this result represents the most stringent limit on monopole flux from direct searches (excluding the indirect searches using mica) in the velocity region $10^{-4} \lesssim \beta \lesssim 10^{-3}$ and it is only a factor of six higher than the Parker bound.

For dyons, this cutoff is $\beta_0 = 9 \times 10^{-5}$. If we only consider the more sensitive horizontal counters, this cutoff is $\beta_0 = 8 \times 10^{-5}$, but the flux limit for this extended β range is $1.3 \times 10^{-14} \text{cm}^{-2} \text{sr}^{-1} \text{sec}^{-1}$ due to the reduced acceptance, as indicated by the short dashed step in Fig. 4.35. Thus, this search has covered essentially all possible velocity range. Its significance lies in that, in addition to the fact that monopoles may carry intrinsic electric charge, most likely bare monopoles have captured protons in the early universe and appear nowadays only in monopole-proton composites [54], and thus the dyon search may be a valid search for any kinds of monopoles. Both mica and the Drell mechanism are insensitive to positively charged dyons, including monopole-proton composites, adding importance to this dyon search.

For $\frac{1}{5}e$ fractionally charged superstring particles, the optimistic threshold is $\beta_0 = 3 \times 10^{-4}$ and the conservative value is $\beta_0 = 8 \times 10^{-4}$.

For nuclearites heavier than 0.1 g, the search is sensitive to any practically interesting velocities. Thus, we may quote the cutoff as the earth escape velocity $\beta_0 = 3.7 \times 10^{-5}$, though this search is sensitive to nuclearites of even lower velocities.

For nuclearites with mass $10^{-10} \text{ g} < m < 0.1 \text{ g}$, the cutoff depends on the mass and the conservative value is $\beta_0 = 7 \times 10^{-5}$ obtained using the smallest mass. For the nuclearites in this mass range, the flux limit is twice as much as that given above because only downward-going ones can reach MACRO, namely, $1.7 \times 10^{-14} \text{ cm}^{-2} \text{ sr}^{-1} \text{ sec}^{-1}$ for $3 \times 10^{-3} < \beta < 2 \times 10^{-2}$ and $1.1 \times 10^{-14} \text{ cm}^{-2} \text{ sr}^{-1} \text{ sec}^{-1}$ for $7 \times 10^{-5} < \beta < 3 \times 10^{-3}$. In the velocity range $(5-7) \times 10^{-5} c$, only horizontal counters are sensitive to the lightest nuclearites, and thus the flux limit for these velocities is $2.6 \times 10^{-14} \text{ cm}^{-2} \text{ sr}^{-1} \text{ sec}^{-1}$.

These limits can address whether supermassive particles are bound in our solar system. In particular, it has been argued [25, 26] that monopoles are very likely to be trapped in the solar system and their local flux is much enhanced as compared to the Parker bound. Freese and Turner [26] have found that if magnetic fields of strength $O(m_{17} 10^6 \text{ G})$ exist inside the sun, the local monopole flux may be enhanced by a factor of $O(5000 m_{17}^2)$ over the Parker bound (monopole mass = $m_{17} 10^{17} \text{ GeV}$). This search suggests that this scenario is unlikely, if monopoles are dyons or have bound protons in the early universe, or if the monopole light yield derived from the measured slow proton scintillation is correct.

Appendix A

Members of the MACRO Collaboration^a

S. Ahlen³, M. Ambrosio¹², R. Antolini², G. Auriemma^{14*}, R. Baker¹¹, A. Baldini¹³, G.C. Barbarino¹², B.C. Barish⁴, G. Battistoni⁶, R. Bellotti¹, C. Bemporad¹³, P. Bernardini¹⁰, H. Bilokon⁶, V. Bisi¹⁶, C. Bloise⁶, S. Bussino¹⁴, F. Cafagna¹, M. Calicchio¹, D. Campana¹², P. Campana⁶, M. Carboni⁶, S. Cecchini^{2*}, F. Cei¹³, V. Chiarella⁶, C. Chiera¹⁴, A. Cobis⁶, R. Cormack³, A. Corona¹⁴, S. Coutu⁴, G. DeCataldo¹, H. Dekhissi², C. DeMarzo¹, M. De Vincenzi¹⁴, A. Di Credico⁹, E. Diehl¹¹, O. Erriquez¹, C. Favuzzi¹, D. Ficenecc^{3o}, C. Forti⁶, L. Foti¹⁴, P. Fusco¹, G. Giacomelli², G. Giannini^{13*}, N. Giglietto¹, P. Giubellino¹⁶, M. Grassi¹³, P. Green¹⁸, A. Grillo⁶, F. Guarino¹², C. Gustavino⁷, A. Habig⁸, R. Heinz⁸, J.T. Hong⁴, E. Iarocci^{6†}, E. Katsavounidis⁴, E. Kearns³, S. Klein^{3‡}, S. Kyriazopoulou⁴, E. Lamanna¹⁴, C. Lane⁵, C. Lee¹¹, D. Levin¹¹, P. Lipari¹⁴, G. Liu⁴, R. Liu⁴, M.J. Longo¹¹, G. Ludlam³, G. Mancarella¹⁰, G. Mandrioli², A. Margiotta-Neri², A. Marin³, A. Marini⁶, D. Martello¹⁰, G. Martellotti¹⁴, A. Marzari Chiesa¹⁶, M. Masera¹⁶, P. Matteuzzi², D.G. Michael⁴, L. Miller⁸, P. Monacelli⁹, M. Monteno¹⁶, S. Mufson⁸, J. Musser⁸, S. Nutter⁸, C. Okada³, G. Osteria¹², O. Palamara¹⁰, S. Parlati⁷, V. Patera⁶, L. Patrizii², R. Pazzi¹³, C.W. Peck⁴, J. Petrakis¹⁷, S. Petrera¹⁰, N.D. Pignatano⁴, P. Pistilli¹⁰, F. Predieri², L. Ramello¹⁶, J. Reynoldson⁷, F. Ronga⁶, G. Rosa¹⁴, C. Satriano^{14*}, L. Satta^{6†}, E. Scapparone², K. Scholberg⁴, A. Sciubba^{14†}, P. Serra Lugaresi², M. Severi¹⁴, M. Sitta¹⁶, P. Spinelli¹, M. Spinetti⁶, M. Spurio², J. Steele⁴, R. Steinberg⁵, J.L. Stone³, L.R. Sulak³, A. Surdo¹⁰, G. Tarlé¹¹, V. Togo², V. Valente⁶, G.R. Verdone^{14*}, C.W. Walter⁴, R. Webb¹⁵, and W. Worstell³

^aThis list is identical to the author list of reference [63].

1. Dipartimento di Fisica dell'Università di Bari and Istituto Nazionale di Fisica Nucleare (INFN), Bari, 70126, Italy
2. Dipartimento di Fisica dell'Università di Bologna and INFN, Bologna, 40126, Italy
3. Physics Department, Boston University, Boston, Massachusetts 02215, USA
4. California Institute of Technology, Pasadena, California 91125, USA
5. Department of Physics, Drexel University, Philadelphia, Pennsylvania 19104, USA
6. Laboratori Nazionali di Frascati dell'INFN, Frascati (Roma), 00044, Italy
7. Laboratori Nazionali del Gran Sasso dell'INFN, Assergi (L'Aquila), 67010, Italy
8. Departments of Physics and of Astronomy, Indiana University, Bloomington, Indiana 47405, USA
9. Dipartimento di Fisica dell'Università dell'Aquila and INFN, L'Aquila, 67100, Italy
10. Dipartimento di Fisica dell'Università di Lecce and INFN, Lecce, 73100, Italy
11. Department of Physics, University of Michigan, Ann Arbor, Michigan 48109, USA
12. Dipartimento di Fisica dell'Università di Napoli and INFN, Napoli, 80125, Italy
13. Dipartimento di Fisica dell'Università di Pisa and INFN, Pisa, 56010, Italy
14. Dipartimento di Fisica dell'Università di Roma and INFN, Roma, 00185, Italy
15. Physics Department, Texas A&M University, College Station, Texas 77843, USA
16. Dipartimento di Fisica dell'Università di Torino and INFN, Torino, 10125, Italy
17. Bartol Research Institute, University of Delaware, Newark, Delaware 19716, USA
18. Sandia National Laboratory, Albuquerque, New Mexico 87185, USA

* Also Università della Basilicata, Potenza, 85100, Italy

● Also Istituto TESRE/CNR, Bologna, Italy

○ Now at Physics Department, Washington University, St. Louis, Missouri 63130, USA

★ Also Università di Trieste and INFN, Trieste, 34100, Italy

† Also Dipartimento di Energetica, Università di Roma, Roma, 00185, Italy

‡ Now at Department of Physics, University of California, Santa Cruz, California 95064, USA

Appendix B

Photoelectron Statistics¹

As discussed in section 2.3.3, 8'' hemispherical Hamamatsu R1408 PMTs are instrumented in the first supermodule of the MACRO detector. The single photoelectron charge spectrum of the R1408 PMT follows an exponential distribution, as shown in Fig. 2.11 on page 39. This exponential spectrum gives the dynode statistics factor of $\sqrt{2}$, as will be derived in this appendix.

This spectrum can be expressed as

$$f_1(q) = \frac{1}{g} \exp\left(-\frac{q}{g}\right), \quad (\text{B.1})$$

where g is the charge gain of the PMT, $f_1(q)$ is the probability density that the single photoelectron has charge q ($q \geq 0$). This distribution has a mean and a standard deviation given by

$$\mu_1 = \int_0^\infty q f_1(q) dq = g \quad \text{and} \quad \sigma_1 = \left[\int_0^\infty (q - \mu_1)^2 f_1(q) dq \right]^{1/2} = g. \quad (\text{B.2})$$

Suppose that $f_n(q)$ is the probability density that a pulse with exactly n ($n \geq 0$) photoelectrons has charge q . Assuming the photoelectrons are independent of each other (this assumption fails only at very high light level when the PMT is saturated), the mean and

¹This appendix essentially follows the derivations given by Peck in a MACRO internal memo [93].

standard deviation of this distribution are given by

$$\mu_n = \int_0^{\infty} q f_n(q) dq = ng \quad \text{and} \quad \sigma_n = \left[\int_0^{\infty} (q - \mu_n)^2 f_n(q) dq \right]^{1/2} = \sqrt{ng} . \quad (\text{B.3})$$

These two quantities can be obtained without knowing the explicit form of the distribution $f_n(q)$. However, it is given below for reference,

$$f_n(q) = \begin{cases} \frac{1}{g(n-1)!} \left(\frac{q}{g}\right)^{n-1} \exp\left(-\frac{q}{g}\right), & \text{if } n > 0 ; \\ \delta(q), & \text{if } n = 0 . \end{cases} \quad (\text{B.4})$$

In reality the number of photoelectrons n follows Poisson statistics $P_n^\lambda = e^{-\lambda} \lambda^n / n!$, where λ is the mean number of photoelectrons. Folding these two distributions together, we obtain the actual charge distribution for pulses having a mean number of photoelectrons of λ ,

$$S_\lambda(q) = \sum_{n=0}^{\infty} P_n^\lambda f_n(q) . \quad (\text{B.5})$$

Thus, one can calculate the mean charge and the standard deviation as

$$\mu_\lambda = \int_0^{\infty} q S_\lambda(q) dq = \lambda g \quad \text{and} \quad \sigma_\lambda = \left[\int_0^{\infty} (q - \mu)^2 S_\lambda(q) dq \right]^{1/2} = \sqrt{2\lambda} g . \quad (\text{B.6})$$

With the gain removed, the mean is equal to the mean of Poisson statistics λ as expected, but the standard deviation is inflated by a factor of $\sqrt{2}$ compared with the standard deviation of Poisson statistics $\sqrt{\lambda}$. This factor is the so-called dynode statistics, which depends on the single photoelectron charge spectrum, which in turn depends on the PMT dynode structure.

From Eq. B.6, one can easily obtain the mean number of photoelectrons in a pulse if the mean and the standard deviation of the pulse charge spectrum are given,

$$\lambda = \left(\frac{\sqrt{2}\mu_\lambda}{\sigma_\lambda} \right)^2 . \quad (\text{B.7})$$

However, in an actual measurement, the charge spectrum $S_\lambda(q)$ does not include the $n = 0$ term in Eq. B.5. Therefore, the mean and standard deviation of a measured charge spectrum

can be used to calculate the mean number of photoelectrons according to the above equation only if the $n = 0$ term is negligible. This requires that $P_0^\lambda = e^{-\lambda} \ll 1$, *i.e.*, the mean number of photoelectron $\lambda > 5$ for an 1% accuracy ($P_0^\lambda < 0.01$). Finally, the central limit theorem gives that the charge spectrum follows a Gaussian distribution for $\lambda \gg 1$.

Appendix C

Simulations of Pulse Trains

A Monte Carlo simulation has been used to study the performance of the slow monopole trigger circuits described in section 3.2. Pulse trains simulating monopole-induced signals have been generated. However, it is important to take into account that for the LED-generated pulse trains used in the sensitivity determinations described in section 3.5, the pulses have a $\sim 1 \mu s$ risetime. For that reason, both ideal square pulse train shapes of monopole-induced signals and the LED pulse train shapes having $1 \mu s$ risetime have been generated. The pulse train is therefore modelled as

$$\lambda(t) = \lambda_0 \left(1 - e^{-t/\tau}\right) , \quad (\text{C.1})$$

where $\lambda(t)$ is the density of photoelectrons, and τ is the risetime. Taking $\tau = 0$ gives a square monopole-like pulse train,

$$\lambda(t) = \lambda_0 , \quad (\text{C.2})$$

and taking $\tau = 1 \mu s$ gives the LED-like pulse train.

The time series of photoelectrons in the pulse train is generated according to the density of the photoelectrons. Supposing that a photoelectron occurs at time t_n , the time t_{n+1} of the next photoelectron is given by

$$\exp\left(-\int_{t_n}^{t_{n+1}} \lambda(t) dt\right) = R , \quad (\text{C.3})$$

where R is a random number uniformly distributed between zero and one. In the case of the monopole-like square pulse train, we have

$$t_{n+1} = t_n - \frac{1}{\lambda_0} \log(R) . \quad (\text{C.4})$$

In the case of the LED-like pulse train, we have to deal with the transcendental equation

$$(t_{n+1} - t_n) + \tau \left[\exp\left(-\frac{t_{n+1}}{\tau}\right) - \exp\left(-\frac{t_n}{\tau}\right) \right] = -\frac{1}{\lambda_0} \log(R) , \quad (\text{C.5})$$

which can be solved numerically. The shape of a single photoelectron (SPE) pulse is modelled as

$$u(t) = \frac{qe^2t}{w^2} \exp\left(-\frac{et}{w}\right) h(t) , \quad (\text{C.6})$$

where q is the integral over time of the SPE pulse shape (*i.e.*, the charge), w is the effective width of the pulse defined as the integral over the peak amplitude, $e = 2.71828 \dots$ is the familiar mathematical constant, and finally $h(t)$ is the step function,

$$h(t) = \begin{cases} 1 , & \text{if } t \geq 0 ; \\ 0 , & \text{if } t < 0 . \end{cases} \quad (\text{C.7})$$

The SPE width $w = 15 \pm 2$ ns is generated to follow a Gaussian distribution. PMT pulses are assumed to be positive-going in the simulation, while the PMTs in the MACRO detector operate with negative high voltages and give negative-going pulses. The SPE charge for Hamamatsu phototubes used in the first supermodule follows an exponential distribution as shown in Eq. B.1 on page 149 and Fig. 2.11 on page 39. Thus, this charge can be generated as

$$q = -g \log(R) , \quad (\text{C.8})$$

where $g = 50$ mV·ns is the nominal average charge (integral) of the SPE pulses into 50Ω , corresponding to a PMT gain of 6.25×10^6 (*cf.* Table 3.3). In the first supermodule, the PMT gain varies from counter to counter and the worst case gain is about half of the average (Fig. 3.17). For this reason, we have also performed simulations with $g = 25$ mV·ns,

corresponding to a PMT gain of 3.1×10^6 . Finally, the shape of the pulse train is given by the sum of all single photoelectron pulses in the train,

$$S(t) = \sum_n u(t - t_n) . \quad (\text{C.9})$$

Some examples of the generated pulse trains are shown in Fig. 3.4.

The generated pulse trains are passed to a simulated slow monopole trigger circuit consisting of a Time Over Half Maximum discriminator (TOHM) and a Leaky Integrator. The parameters are set to be the same as the actual setup in the first year of running: the TOHM threshold is 2.5 mV, the activity level is $C_{\text{act}} = 6$, the trigger level is $C_{\text{tr}} = 16$, the down counting period is $D = 1/R_d = 180$ ns, and the up counting clock is $R_u = 66$ MHz (section 3.4).

The above Monte Carlo was done for various pulse train durations spread from 250 ns to 20 μ s. For each duration, we obtain curves of the trigger efficiency as a function of the number of photoelectrons in the pulse train, an example of which is shown in Fig.C.1. From these curves, for each pulse train duration, we obtain numbers of photoelectrons at 90% trigger efficiencies, which are plotted in Fig. C.2. For comparison, the Monte Carlo results in Fig. C.2 and the empirical measured results using LEDs in Fig. 3.16 are plotted together in Fig. C.3.

As one can see from Fig. C.2 and Fig. C.1, for pulse trains of ≥ 1 μ s durations, the LED risetime only makes a tiny difference ($< 5\%$) to the efficiency. However, for the short pulse trains, an LED pulse with a risetime apparently requires $\sim 30\%$ more light to achieve 90% trigger efficiency than a monopole-like square pulse, making the sensitivity measurements using LEDs conservative.

As indicated by Fig. C.2, reducing the PMT gain by a factor of two increases the required amount of light at 90% trigger efficiency by a factor of less than two: this factor is 1.8 for pulse trains of durations ≥ 5 μ s and it is 1.4 for 1 μ s trains. As the pulse gets shorter, this factor approaches one. These behaviors are reasonable: for the long trains, the SPEs are spread out and the average pulse heights decrease as the phototube gain is

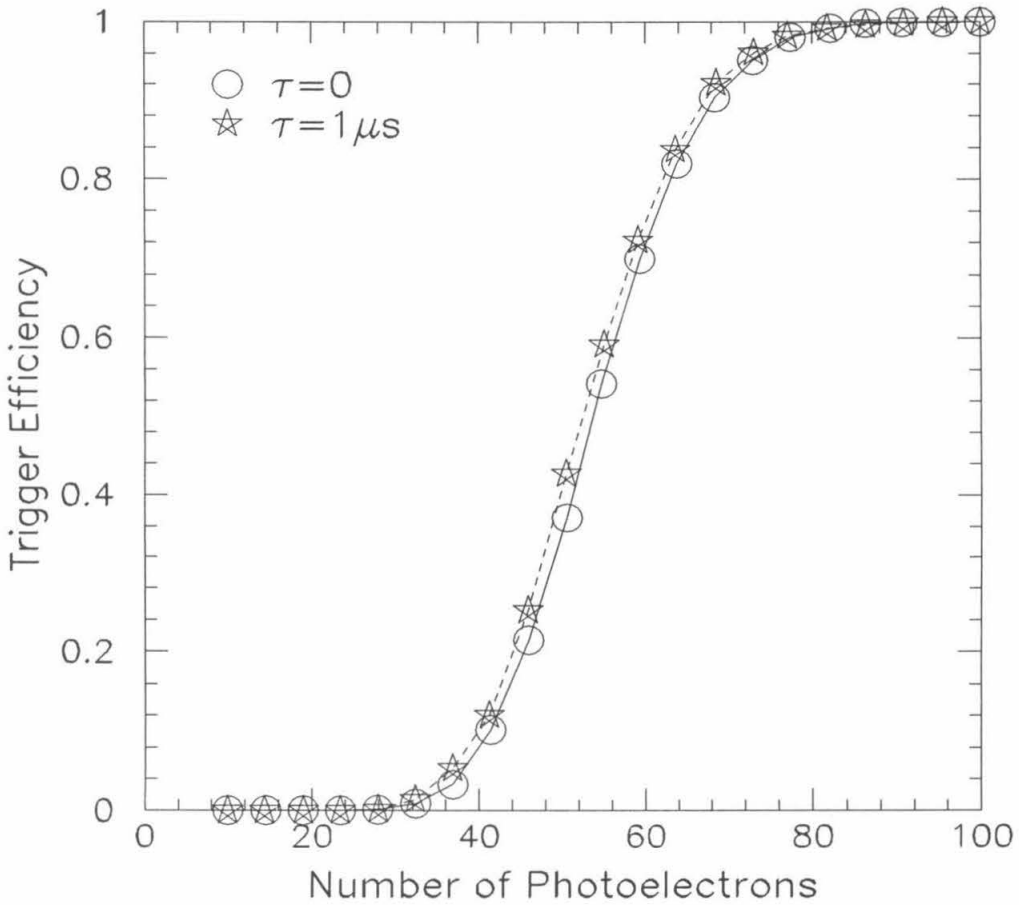


Figure C.1: Slow monopole trigger efficiency as a function of light level for $2\mu\text{s}$ pulse trains as simulated in the Monte Carlo. The PMT gain is 6.25×10^6 .

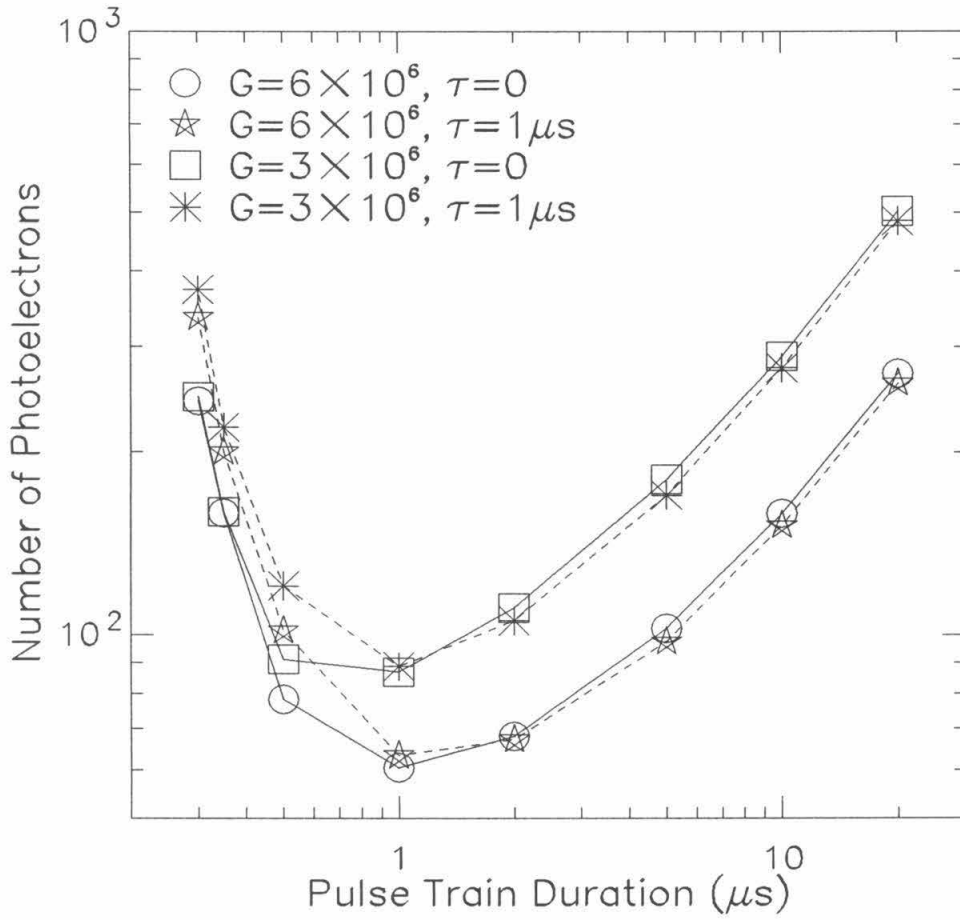


Figure C.2: Slow monopole trigger sensitivity at 90% efficiency as simulated in the Monte Carlo.

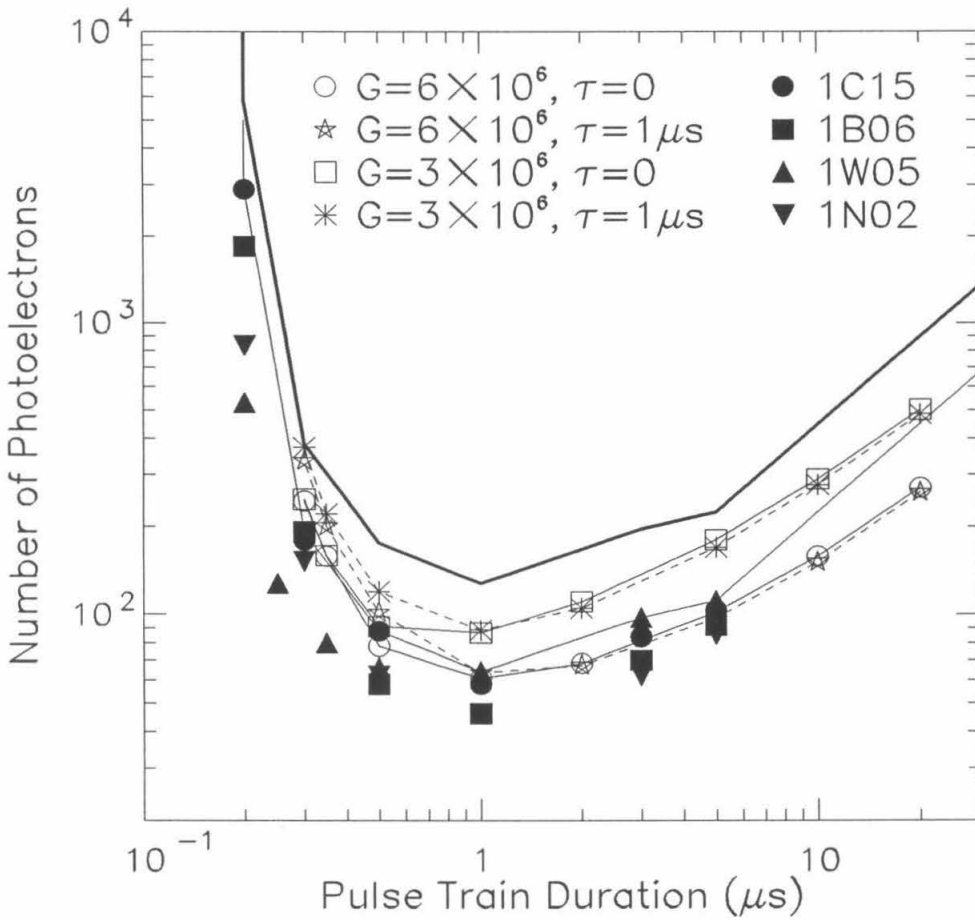


Figure C.3: Slow monopole trigger sensitivity at 90% efficiency as simulated in the Monte Carlo (the un-blacked symbols) and as empirically measured using LEDs (the blackened symbols). This plot combines Fig. 3.16 and Fig. C.2. See those two plots for explanations.

reduced; the SPEs in the high tails of the exponential pulse height spectrum can still pass the TOHM discrimination level though the fraction of these high tail SPEs decreases. For short pulses of high light level, the effect of gain variations is less evident because their pulse heights are much larger than the TOHM threshold.

Fig. C.3 shows that the Monte Carlo results using the PMT gain of 6×10^6 are in good agreement with the empirical LED measurements. The results also demonstrate that our finally quoted sensitivity as indicated by the thick curve is a very conservative one, even compared with the Monte Carlo results with half gain (3×10^6).

Appendix D

Numbers of Stopping Muons in FMT Candidates

As described on page 134 in section 4.3.2, among the eight final candidates from the fast monopole trigger (FMT) data, six or seven events are consistent with stopping muons (one event is uncertain because of lack of the streamer tube signals). In this appendix, we shall give a rough estimate of the expected number of such candidates caused by stopping muons.

In order for a stopping muon to fire the FMT, it must traverse the first layer of scintillator and stop inside the detector, and the decay electron must reach the second scintillator layer with sufficient energy. A muon stopping in the second layer of scintillator would not fire the FMT, because it would fire the SPAM fast muon trigger which would veto the FMT.

For simplicity, I shall ignore the angular dependence of the flux of muons reaching the MACRO detector and assume that the muon trajectories are vertical. The vertical flux of muons crossing the MACRO detector has been fit to the simple phenomenological exponential form

$$I_0(d) \propto \exp(-d/d_0), \quad (\text{D.1})$$

where d is the thickness of the rock overburden. The fit result is $d_0 = 7.6 \times 10^4 \text{ g cm}^{-2}$ [94].

Thus, the probability for a muon to stop in a layer of $(x, x + dx)$ is dx/d_0 , where x is the distance above the second hit scintillator plane. The electron from the muon decay has an energy spectrum given by [95] (in the natural units $\hbar = c = 1$)

$$\frac{dP}{dE} = 16E^2(3 - \frac{4E}{m})/m^3, \quad 0 \leq E \leq \frac{m}{2}, \quad (\text{D.2})$$

where dP is the probability for the electron energy to be in the interval $(E, E + dE)$, m is the muon mass, and the electron mass is ignored. This spectrum has been normalized so that

$$\int_0^{m/2} \frac{dP}{dE} dE = 1. \quad (\text{D.3})$$

If we ignore the polarizations of the cosmic ray muons, the decay electron is isotropic. Thus, the probability of the electron to reach the scintillator with remaining energy greater than Q is

$$\mathcal{P}(x) = \frac{1}{2} \int_0^{\pi/2} d\theta \sin \theta \int_0^{m/2} dE \frac{dP}{dE} h(E - \frac{x}{\cos \theta} I_0 - Q), \quad (\text{D.4})$$

where Q is the minimum required deposited energy in the FMT charge cut which has been chosen as the most probable muon energy loss (31 MeV), θ is the angle of the decay electron from the downward vertical direction, the factor of 1/2 is due to the fact that the isotropic decay electron could go upwards, $h(x)$ is the step function (Eq. C.7), and finally $I_0 = 2 \text{ MeV g}^{-1} \text{ cm}^2$ is the ionization energy loss rate (the radiation energy loss is ignored).

Hence the expected number of stopping muons in the final fast monopole candidates is

$$N = N_\mu f_{\text{TOF}} f_{\text{peak}} \int_0^\infty \mathcal{P}(x) dx/d_0. \quad (\text{D.5})$$

Here $N_\mu = 1.4 \times 10^6$ is the total number of muons observed during the FMT livetime of 453 days. The factor f_{TOF} is due to the 1-7 μs TOF window of the FMT trigger; the probability for a stopping muon to decay in this time window is

$$f_{\text{TOF}} = \frac{1}{\tau} \int_1^7 e^{-t/\tau} dt = 0.59, \quad (\text{D.6})$$

where $\tau = 2.2 \mu\text{s}$ is the muon lifetime. Finally, f_{peak} is another reduction factor due to the charge cut at the first scintillator layer which requires that the deposited energy be greater

than the peak charge, and it is

$$f_{\text{peak}} = \int_{q_0}^{\infty} f(q) dq = \int_0^{\infty} \phi(\lambda) d\lambda = 0.71, \quad (\text{D.7})$$

where q_0 is the peak charge, $f(q)$ is defined in Eq. 4.6, and $\phi(\lambda)$ is the Landau function (Eq. 4.7). In reality, because the energy loss in a single collision cannot exceed the energy of the incident muon, the upper limit in the integral in Eq. D.7 is finite, but $+\infty$ is a quite good approximation. Finally, let us compute the integral

$$X_0 = \int_0^{\infty} \mathcal{P}(x) dx = \frac{1}{2} \int_0^{\pi/2} d\theta \sin \theta \int_0^{m/2} dE \frac{dP}{dE} \int_0^{\infty} dx h\left(E - \frac{x}{\cos \theta} I_0 - Q\right). \quad (\text{D.8})$$

Let $y = x / \cos \theta$, and we have

$$\begin{aligned} X_0 &= \frac{1}{2} \int_0^{\pi/2} d\theta \sin \theta \cos \theta \int_0^{m/2} dE \frac{dP}{dE} \int_0^{\infty} dy h(E - I_0 y - Q), \\ &= \frac{1}{4} \int_Q^{m/2} dE \frac{dP}{dE} \frac{E - Q}{I_0}, \\ &= \frac{m}{80I_0} \left[7 - 20 \frac{Q}{m} + 80 \left(\frac{Q}{m} \right)^4 - 64 \left(\frac{Q}{m} \right)^5 \right]. \end{aligned} \quad (\text{D.9})$$

Inserting $Q = 31 \text{ MeV}$ and $I_0 = 2 \text{ MeV g}^{-1} \text{cm}^2$, we obtain that $X_0 = 1.1 \text{ g cm}^{-2}$.

Therefore, putting together all numbers, we obtain the expected number of stopping muons in the fast monopole candidates

$$N = N_{\mu} \frac{X_0}{d_0} f_{\text{TOF}} f_{\text{peak}} = 8.5, \quad (\text{D.10})$$

which is in agreement with the observed number of six or seven.

Bibliography

- [1] The quotation on page iii is from a poem by S.L. Glashow given in the conference summary of the Seventh Workshop on Grand Unification held in Toyama, Japan in 1986. The poem is reprinted in Martin Gardner, *The New Ambidextrous Universe*, 3rd ed. (W.H. Freeman and Company, New York, 1990), p. 347.
- [2] Petrus Peregrinus, *Epistola de magnete — Epistle of Peter Peregrinus of Maricourt to Sygerus of Foncaucourt, soldier, concerning the magnet*, written in 1269AD, translated from Latin into English by Silvanus P. Thompson (Chiswick Press, London, 1902).
- [3] J. Preskill, *Ann. Rev. Nucl. Part. Sci.*, **34**, 461 (1984).
- [4] D.E. Groom, *Phys. Reports*, **140**, 323 (1986).
- [5] *Magnetic Monopoles*, Proceedings of a NATO Advanced Study Institute on Magnetic Monopoles, held October 14-17, 1982 in Wingspread, Wisconsin, edited by R.A. Carrigan, Jr., and W.P. Trower (Plenum Press, New York, 1983).
- [6] *Monopole '83*, Proceedings of a NATO Advanced Research Workshop entitled Monopole '83, held October 6-9, 1983 in Ann Arbor, Michigan, edited by J.L. Stone (Plenum Press, New York, 1984).
- [7] P.A.M. Dirac, *Proc. Roy. Soc. London*, **A 133**, 60 (1931); *Phys. Rev.*, **74**, 817 (1948).
- [8] See, for example, R.A. Millikan, *Science*, **32**, 436 (1910).
- [9] J. Preskill, in *Magnetic Monopoles* (Ref. [5]), p. 111.
- [10] H. Georgi and S.L. Glashow, *Phys. Rev. Lett.*, **32**, 438 (1974).

- [11] H. Georgi, H.R. Quinn, and S. Weinberg, *Phys. Rev. Lett.*, **33**, 451 (1974).
- [12] G. 't Hooft, *Nucl. Phys. B*, **79**, 276 (1974).
- [13] A.M. Polykov, *JETP Lett.*, **20**, 194 (1974).
- [14] For a review on proton decay experiments, see R. Barloutaud, *Nucl. Phys. B (Proc. Suppl.)*, **28A**, 437 (1992).
- [15] U. Amaldi, W. de Boer, P.H. Frampton, H. Fürstenau, and J.T. Liu, *Phys. Lett. B*, **281**, 374 (1992).
- [16] R.N. Mohapatra, *Unification and Supersymmetry*, 2nd ed. (Springer-Verlag, New York, 1992).
- [17] X.-G. Wen and E. Witten, *Nucl. Phys. B*, **261**, 651 (1985).
- [18] G. Lazarides, C. Panagiotakopoulos, and Q. Shafi, *Phys. Rev. Lett.*, **58**, 1707 (1987).
- [19] E.W. Kolb and M.S. Turner, *The Early Universe* (Addison-Wesley, Redwood City, Calif., 1990).
- [20] T.W.B. Kibble, *J. Phys. A*, **9**, 1387 (1976).
- [21] J.P. Preskill, *Phys. Rev. Lett.*, **43**, 1365 (1979).
- [22] A.H. Guth, *Phys. Rev. D*, **23**, 347 (1981).
- [23] K.A. Olive, *Phys. Reports*, **190**, 307 (1990).
- [24] M.S. Turner, E.N. Parker, and T.J. Bogdan, *Phys. Rev. D*, **26**, 1296 (1982).
- [25] S. Dimopoulos, S.L. Glashow, E.M. Purcell, and F. Wilczek, *Nature*, **298**, 824 (1982).
- [26] K. Freese and M.S. Turner, *Phys. Lett. B*, **123**, 293 (1983).
- [27] E.N. Parker, *Astrophys. J.*, **160**, 383 (1970); **163**, 255 (1971); **166**, 295 (1971).
- [28] Y. Rephaeli and M.S. Turner, *Phys. Lett. B*, **121**, 115 (1983).
- [29] J.A. Harvey, M.A. Ruderman, and J. Shaham, *Phys. Rev. D*, **33**, 2084 (1986).

- [30] S. Berman *et al.*, *Phys. Rev. Lett.*, **64**, 839 (1990).
- [31] See, for example, K. Kinoshita, *Phys. Rev. D*, **46**, 881 (1992).
- [32] S.P. Ahlen and K. Kinoshita, *Phys. Rev. D*, **26**, 2347 (1982).
- [33] See, for example, T. Ebisu and T. Watanabe, *Phys. Rev. D*, **36**, 3359 (1987).
- [34] R.R. Ross, P.H. Eberhard, L.W. Alvarez, and R.D. Watt, *Phys. Rev. D*, **8**, 698 (1973).
- [35] B. Julia and A. Zee, *Phys. Rev. D*, **11**, 2227 (1975).
- [36] M.E. Huber, B. Cabrera, M.A. Taber, and R.D. Gardner, *Phys. Rev. Lett.*, **64**, 835 (1990); *Phys. Rev. D*, **44**, 636 (1991).
- [37] E.N. Alexeyev, M.M. Boliev, A.E. Chudakov, and S.P. Mikheyev, *Proc. 21st Intern. Cosmic Ray Conf.* (Adelaide, 1990), edited by R.J. Protheroe, **v. 10**, p. 83 (abstract only); E.N. Alexeyev *et al.*, *Lett. Nuovo Cimento*, **35**, 413 (1982).
- [38] B. Barish, G. Liu, and C. Lane, *Phys. Rev. D*, **36**, 2641 (1987).
- [39] M.J. Shepko *et al.*, *Phys. Rev. D*, **35**, 2917 (1987).
- [40] D.J. Ficenec, *Ph.D. Thesis*, Boston University, 1990.
- [41] R. Bellotti *et al.* (MACRO Collaboration), *Proc. 21st Intern. Cosmic Ray Conf.* (Adelaide, 1990), edited by R.J. Protheroe, **vol. 10**, p. 75.
- [42] S.D. Drell, N.M. Kroll, M.T. Mueller, S. Parke, and M.H. Ruderman, *Phys. Rev. Lett.*, **50**, 644 (1983).
- [43] N.M. Kroll, V. Ganapathi, S.J. Parke, and S.D. Drell, in *Monopole '83* (Ref. [6]), p. 295.
- [44] See, for example, F. Kajino, S. Matsuno, Y.K. Yuan, and T. Kitamura, *Phys. Rev. Lett.*, **52**, 1373 (1984); T.E. Bortner and G.S. Hurst, *Phys. Rev.*, **93**, 1236 (1954); W.P. Jesse, *J. Chem. Phys.*, **41**, 2060 (1964).
- [45] V. Patera, *Phys. Lett. A*, **137**, 259 (1989).

- [46] K.N. Buckland, G.E. Masek, W. Vernon, L.M. Knapp, and J.P. Stronski, *Phys. Rev. D*, **41**, 2726 (1990).
- [47] J.L. Thron *et al.* (Soudan 2 Collaboration), *Phys. Rev. D*, **46**, 4846 (1992).
- [48] S. Orito *et al.*, *Phys. Rev. Lett.*, **66**, 1951 (1991).
- [49] D.P. Snowden-Ifft and P.B. Price, *Phys. Lett. B*, **288**, 250 (1992).
- [50] P.B. Price, *Phys. Lett. B*, **140**, 112 (1984).
- [51] D. Ghosh and S. Chatterjea, *Europhys. Lett.*, **12**, 25 (1990).
- [52] P.B. Price and M.H. Salamon, *Phys. Rev. Lett.*, **56**, 1226 (1986).
- [53] P.B. Price, S. Guo, S.P. Ahlen, and R.L. Fleischer, *Phys. Rev. Lett.*, **52**, 1265 (1984).
- [54] L. Bracci, G. Fiorentini, G. Mezzorani, and P. Quarati, *Phys. Lett. B*, **143**, 357 (1984); **155**, 468 (erratum) (1985).
- [55] V.A. Rubakov, *JETP Lett.*, **33**, 644 (1981); *Nucl. Phys. B*, **203**, 311 (1982).
- [56] C.G. Callan, Jr., *Phys. Rev. D*, **25**, 2141 (1982); **26**, 2058 (1982).
- [57] E. Witten, *Phys. Rev. D*, **30**, 272 (1984).
- [58] E. Farhi and R.L. Jaffe, *Phys. Rev. D*, **30**, 2379 (1984).
- [59] A. De Rújula and S.L. Glashow, *Nature*, **312**, 734 (1984).
- [60] C. Alcock and A. Olinto, *Ann. Rev. Nucl. Part. Sci.*, **38**, 161 (1988).
- [61] *Strange Quark Matter in Physics and Astrophysics*, Proceedings of the International Workshop on Strange Quark Matter in Physics and Astrophysics, University of Aarhus, Denmark, 20-24 May 1991, edited by J. Madsen and P. Haensel (Elsevier, Amsterdam, 1991), *Nucl. Phys. B (Proc. Suppl.)*, **24B** (1991).
- [62] J. Barrette *et al.*, *Phys. Lett. B*, **252**, 550 (1990).
- [63] S. Ahlen *et al.* (MACRO Collaboration), *Phys. Rev. Lett.*, **69**, 1860 (1992).

- [64] K. Nakamura, H. Horie, T. Takahashi, and T. Tanimori, *Phys. Lett. B*, **161**, 417 (1985).
- [65] P.B. Price, *Phys. Rev. D*, **38**, 3813 (1988).
- [66] S. Nakamura *et al.*, *Phys. Lett. B*, **263**, 529 (1991).
- [67] T. Saito, H. Hatano, Y. Fukada, and H. Oda, *Phys. Rev. Lett.*, **65**, 2094 (1990).
- [68] G. Liu and B. Barish, *Phys. Rev. Lett.*, **61**, 271 (1988).
- [69] S. Ahlen *et al.* (MACRO Collaboration), *Nucl. Instrum. & Methods*, **A324**, 337 (1993).
- [70] S. Ahlen *et al.* (MACRO Collaboration), *Phys. Rev. D*, **46**, 895 (1992).
- [71] S. Ahlen *et al.* (MACRO Collaboration), *Astroparticle Physics*, **1**, 11 (1992).
- [72] S. Ahlen *et al.* (MACRO Collaboration), accepted by *Astrophys. J.* (to appear in the July 20, 1993 issue).
- [73] E. Iarocci, *Nucl. Instrum. & Methods*, **217**, 30 (1983).
- [74] G. Battistoni *et al.*, *Nucl. Instrum. & Methods*, **176**, 297 (1980).
- [75] G. Auriemma *et al.*, *Nucl. Instrum. & Methods*, **A263**, 249 (1988).
- [76] I.B. Berlman, *Handbook of Fluorescence Spectra of Aromatic Molecules*, 2nd. ed. (Academic Press, New York, 1971).
- [77] Hamamatsu Corp., Technical Data Sheet for R1408 Photomultiplier Tube (undated).
- [78] S.P. Ahlen, *Phys. Rev. D*, **17**, 229 (1978).
- [79] J.A. Harvey and N.W. Hill, *Nucl. Instrum. & Methods*, **162**, 507 (1979).
- [80] J. Lindhard, *Dan. Mat. Fys. Medd.* **28**, no. 8 (1954).
- [81] J. Lindhard and M. Scharff, *Phys. Rev.*, **124**, 128 (1961).
- [82] E. Fermi and E. Teller, *Phys. Rev.*, **72**, 399 (1947).
- [83] S.P. Ahlen and G. Tarlé, *Phys. Rev. D*, **27**, 688 (1983).

- [84] W. Brandt and J. Reinheimer, *Canadian J. Phys.*, **46**, 607 (1968).
- [85] D.J. Ficenec, S.P. Ahlen, A.A. Marin, J.A. Musser, and G. Tarlé, *Phys. Rev. D*, **36**, 311 (1987).
- [86] D.E. Groom, E.C. Loh, H.R. Nelson, and D.M. Ritson, *Phys. Rev. Lett.*, **51**, 941 (1983).
- [87] S.P. Ahlen, T.M. Liss, C. Lane, and G. Liu, *Phys. Rev. Lett.*, **55**, 181 (1985).
- [88] G. Liu, *Ph.D. Thesis*, California Institute of Technology, 1987.
- [89] D.E. Knuth, *The Art of Computer Programming*, vol. 1, 2nd. ed. (Addison-Wesley, Reading, Mass., 1973).
- [90] A.M. Tenenbaum, Y. Langsam, and M.J. Augenstein, *Data Structure Using C*, (Prentice Hall, Englewood Cliffs, N.J., 1990).
- [91] LeCroy Corp., *Research Instrumentation Catalog* (1992).
- [92] W.H. Press, B.P. Flannery, S.A. Teukolsky and W.T. Vetterling, *Numerical Recipes, The Art of Scientific Computing*, (Cambridge University Press, New York, 1989).
- [93] C. Peck, *MACRO Internal Memo*, 1008/87 (1987).
- [94] S.P. Ahlen *et al.* (MACRO Collaboration), *Phys. Lett. B*, **249**, 149 (1990).
- [95] F. Halzen and A.D. Martin, *Quarks and Leptons* (John Wiley & Sons, New York, 1984).